

**Technical Design Report**  
 for the  
**Paul Scherrer Institute Experiment R-12-01.1:**  
**Studying the Proton “Radius” Puzzle with  $\mu p$  Elastic**  
**Scattering**  
 June 1, 2017

**The MUon Scattering Experiment collaboration (MUSE):**

R. Gilman (Contact person),<sup>1</sup> E.J. Downie (Spokesperson),<sup>2</sup> G. Ron (Spokesperson),<sup>3</sup>  
 S. Strauch (Spokesperson),<sup>4</sup> A. Afanasev,<sup>2</sup> A. Akmal,<sup>5</sup> J. Arrington,<sup>6</sup> H. Atac,<sup>7</sup>  
 C. Ayerbe-Gayoso,<sup>8</sup> F. Benmokhtar,<sup>9</sup> N. Benmouna,<sup>5</sup> J. Bernauer,<sup>10</sup> A. Blomberg,<sup>7</sup>  
 W. J. Briscoe,<sup>2</sup> D. Cioffi,<sup>2</sup> E. Cline,<sup>1</sup> D. Cohen,<sup>3</sup> E. O. Cohen,<sup>11</sup> C. Collicott,<sup>12</sup>  
 K. Deiters,<sup>13</sup> J. Diefenbach,<sup>12</sup> B. Dongwi,<sup>14</sup> D. Ghosal,<sup>15</sup> A. Golossanov,<sup>2</sup> R. Gothe,<sup>4</sup>  
 D. Higinbotham,<sup>16</sup> D. Hornidge,<sup>17</sup> Y. Ilieva,<sup>4</sup> N. Kalantarians,<sup>14</sup> M. Kohl,<sup>14</sup> B. Krusche,<sup>15</sup>  
 G. Kumbartzki,<sup>1</sup> I. Lavruchin,<sup>2</sup> L. Li,<sup>4</sup> J. Lichtenstadt,<sup>11</sup> W. Lin,<sup>1</sup> A. Liyanage,<sup>14</sup>  
 W. Lorenzon,<sup>18</sup> K. E. Mesick,<sup>19</sup> Z.-E. Meziani,<sup>7</sup> P. Mohanmurthy,<sup>10</sup> P. Moran,<sup>7</sup>  
 J. Nazeer,<sup>14</sup> E. Piassetzky,<sup>11</sup> R. Ransome,<sup>1</sup> R. Raymond,<sup>18</sup> D. Reggiani,<sup>13</sup> P.E. Reimer,<sup>6</sup>  
 A. Richter,<sup>20</sup> T. Rostomyan,<sup>1</sup> P. Roy,<sup>18</sup> A. Sarty,<sup>21</sup> Y. Shamai,<sup>22</sup> N. Sparveris,<sup>7</sup>  
 N. Steinberg,<sup>18</sup> I. Strakovsky,<sup>2</sup> V. Sulkosky,<sup>23</sup> A.S. Tadepalli,<sup>1</sup> and M. Taragin<sup>24</sup>

<sup>1</sup>*Rutgers University, New Brunswick, New Jersey, USA*

<sup>2</sup>*George Washington University, Washington, DC, USA*

<sup>3</sup>*Hebrew University of Jerusalem, Jerusalem, Israel*

<sup>4</sup>*University of South Carolina, Columbia, South Carolina, USA*

<sup>5</sup>*Montgomery College, Rockville, MD, USA*

<sup>6</sup>*Argonne National Lab, Argonne, IL, USA*

<sup>7</sup>*Temple University, Philadelphia, Pennsylvania, USA*

<sup>8</sup>*College of William & Mary, Williamsburg, Virginia, USA*

<sup>9</sup>*Duquesne University, Pittsburgh, PA, USA*

<sup>10</sup>*Massachusetts Institute of Technology, Cambridge, Massachusetts, USA*

<sup>11</sup>*Tel Aviv University, Tel Aviv, Israel*

<sup>12</sup>*Johannes Gutenberg-Universität, Mainz, Germany*

<sup>13</sup>*Paul Scherrer Institut, CH-5232 Villigen, Switzerland*

<sup>14</sup>*Hampton University, Hampton, Virginia, USA*

<sup>15</sup>*University of Basel, Switzerland*

<sup>16</sup>*Jefferson Lab, Newport News, Virginia, USA*

<sup>17</sup>*Mount Alison University, New Brunswick, Canada*

<sup>18</sup>*University of Michigan, Ann Arbor, Michigan, USA*

<sup>19</sup>*Los Alamos National Laboratory, Los Alamos, NM, USA*

<sup>20</sup>*Technical University of Darmstadt, Darmstadt, Germany*

<sup>21</sup>*St. Mary's University, Halifax, Nova Scotia, Canada*

<sup>22</sup>*Soreq Nuclear Research Center, Israel*

<sup>23</sup>*University of Virginia, Charlottesville, Virginia, USA*

<sup>24</sup>*Weizmann Institute, Rehovot, Israel*

The difference in proton radii measured with  $\mu p$  atoms and with  $ep$  atoms and scattering remains an unexplained puzzle. The PSI MUSE proposal is to measure  $\mu p$  and  $ep$  scattering in the same experiment at the same time. The experiment will determine cross sections, two-photon effects, form factors, and radii independently for the two reactions, and will allow  $\mu p$  and  $ep$  results to be compared with reduced systematic uncertainties. These data should provide the best test of lepton universality in a scattering experiment to date, about an order of magnitude improvement over previous tests. Measuring scattering with both particle polarities will allow a test of two-photon exchange at the sub-percent level, about a factor of four improvement on uncertainties and over an order of magnitude more data points than previous low momentum transfer determinations, and similar to the current generation of higher momentum transfer electron experiments. The experiment has the potential to demonstrate whether the  $\mu p$  and  $ep$  interactions are consistent or different, and whether any difference results from novel physics or two-photon exchange. The uncertainties are such that if the discrepancy is real it should be confirmed with  $\approx 5\sigma$  significance, similar to that already established between the regular and muonic hydrogen Lamb shift.

## CONTENTS

I. Motivation	5
II. Experiment Overview	7
A. Beam Properties	8
B. Experimental Equipment	9
C. Rates, Accidentals, Statistics	11
D. Systematics	13
III. The $\pi$ M1 Beam Line and Detectors	14
A. Beam Properties	14
1. Measured Beam Properties	14
2. Beam Simulations	16
B. Beam Line Detectors	17
1. Beam Cerenkov	17
2. Beam Hodoscope	20
3. GEM Chambers	24
4. Beam Veto	30
5. Beam Monitor	32
C. Target	33
1. Purpose	33
2. Requirements	33
3. Target Design: Major Sub-Systems	34
4. Target Design: Engineering Design by Create	37
5. Target Design: Target Cell Design and Fabrication	41
6. Target Design: Safety Measures and Tests	42
7. Current status and path to completion	44
8. Operation and Maintenance of the Target	44
IV. Scattered Particle Spectrometer	44
A. Straw Chambers	44

B. Scattered-Particle Scintillators	49
V. DAQ	54
A. Electronics and Readout	54
B. Trigger	58
C. Software Systems	62
VI. Tests, Commissioning, Calibrations, Runs	63
A. Installation and Commissioning	63
B. Calibrations	64
C. Dress Rehearsal Run Plan	65
D. Run Plan	66
E. Personnel for Production Runs	68
VII. Analysis, Corrections, Systematics, Results	69
A. Data Analysis	69
1. Determination of Yields	69
2. Backgrounds	71
3. Solid Angle	75
4. Projected Data with Statistical Uncertainties	76
5. Derived Data with Statistical Uncertainties	77
B. Corrections	79
1. Magnetic and $Q^2$ Correction	80
2. Radiative Corrections	80
3. Radiative Corrections and Beam Momentum	81
4. Two-photon exchange	82
C. Systematics	83
1. Beam Detector Related Systematics	84
2. Beam Momentum Determination Systematics	84
3. Target Systematics	85
4. Scattered Particle Detector Systematics	85
5. Solid Angle	85

6. Electronics, Trigger, and Computer Live Time Uncertainties	86
7. Uncertainties in Theoretical Corrections	86
8. Analysis and Instability Uncertainties	87
9. Systematic Uncertainties for Ratios	87
D. Radius Extraction	87
VIII. Project Management	89
A. Collaboration	91
A. Backgrounds	92
B. Systematic Uncertainties	95
C. Electronics Layout	102
References	104

## I. MOTIVATION

In 2010, a Paul Scherrer Institute (PSI) experiment [1] reported that the proton radius determined from muonic hydrogen level transitions is  $0.84184 \pm 0.00067$  fm, about  $5\sigma$  off from the nearly order-of-magnitude less precise, non-muonic measurements. This “proton radius puzzle” was confirmed in 2013 by a second measurement of muonic hydrogen [2] that determined the radius to be  $0.84087 \pm 0.00039$  fm.

New electronic results of  $0.879 \pm 0.008$  fm [3] and  $0.875 \pm 0.010$  fm [4], all from scattering measurements, confirmed the puzzle, and a new CODATA analysis [5] increased the significance of the discrepancy between electronic and muonic measurements to  $>7\sigma$ . The situation has been discussed extensively in a number of papers - here we point out a review paper in Annual Review of Nuclear and Particle Science [6] - and in many talks and two dedicated workshops [7, 8]. It is generally agreed that new data are needed to resolve the puzzle, and the MUon Scattering Experiment (MUSE) discussed here uniquely attempts to resolve the puzzle. Our intent is

- to directly compare  $ep$  to  $\mu p$  elastic scattering at the sub-percent level, in simultaneous measurements, more precisely than done before, and at much lower  $Q^2$ ,
- to compare cross sections of positive vs. negative charged particles to test two-photon exchange effects in both  $ep$  to  $\mu p$  elastic scattering at the sub-percent level, more precisely than done before,
- and to extract the proton radius from the slope of the elastic electric form factor at  $Q^2 = 0$ , the first significant  $\mu p$  scattering radius determination, at roughly the same level as done in previous electron scattering experiments.

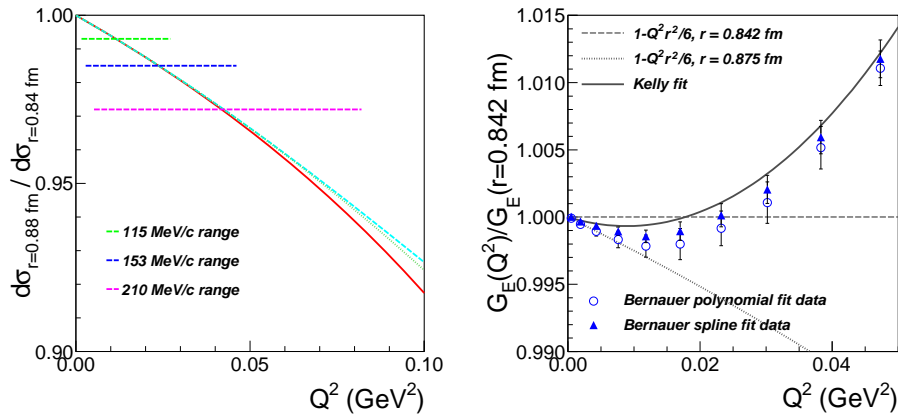


FIG. 1. Left: Effect on the cross section from the proton radius being 0.88 fm vs. 0.84 fm. The solid red line uses a linear approximation,  $G_E = 1 - Q^2 r^2 / 6$ . The cyan dashed and green dotted curves include  $Q^4$  and  $Q^6$  terms taken from the Kelly parameterization, respectively. The horizontal green, blue, and magenta dashed lines indicate the kinematic range of the proposed MUSE data. Right: Mainz results for the proton electric form factor determined by spline and polynomial fit analyses of the cross sections, over a low  $Q^2$  range to show how terms beyond the linear term quickly become important. Also shown are the Kelly parameterization and a linear fit assuming the radius determined by  $ep$  measurements, all relative to expectations from a linear fit using the radius determined from  $\mu p$  atoms. Note the greatly expanded vertical scale compared to the left panel.

Figure 1 gives a quick indication of the minimum requirements for the experiment. The left panel shows that a radius of 0.88 fm vs. 0.84 fm results in a cross section that falls

off about 6% faster over the range of the MUSE kinematics. Thus a determination of the radius at a  $5\sigma$ ,  $< 0.01$  fm, level requires cross sections at at least the percent level. The right panel shows on an expanded  $Q^2$  scale some parameterizations compared to the Mainz data for  $G_E^p(Q^2)$ , extracted from the cross sections using spline and polynomial fit functions to the data, all relative to the expected behavior if the form factor is linear with a radius of 0.842 fm. In  $ep$  scattering, the charge radius is determined from the slope of the form factor  $G_E$  at  $Q^2 = 0$ . The lowest  $Q^2$  Mainz data points are more consistent with the larger radius found in  $ep$  experiments, but even before  $Q^2 = 0.02$  GeV<sup>2</sup> the form factor is starting to show nonlinearities. The curvature at low  $Q^2$  indicates the importance of measuring at low  $Q^2$  to be sensitive to the radius, and over a range of  $Q^2$  to have sensitivity to higher-order terms. In this report, we discuss many aspects of the MUSE experiment, including the backgrounds and systematic effects that drive the key performance specifications for the equipment, factors that lead to the experimental statistics, and the data taking and analysis, leading to the extraction of the proton radius at a level of  $< 0.01$  fm, in Section VII D. The Kelly parameterization [9] shown generally predicts the trends of the data – as do several other standard data parameterizations – and will be used for estimating rates and systematics.

## II. EXPERIMENT OVERVIEW

TABLE I. MUSE kinematic coverage.

Quantity	Coverage
Beam momenta	115, 153, 210 MeV/ $c$
Scattering angle range	20° - 100°
Azimuthal coverage	30% of $2\pi$ typical
$Q^2$ range for electrons	0.0016 GeV <sup>2</sup> - 0.0820 GeV <sup>2</sup>
$Q^2$ range for muons	0.0016 GeV <sup>2</sup> - 0.0799 GeV <sup>2</sup>

MUSE will measure cross sections for elastic  $\mu^\pm p$  and  $e^\pm p$  scattering in the PSI  $\pi M1$  beam line. Table I summarizes the kinematics.

## A. Beam Properties

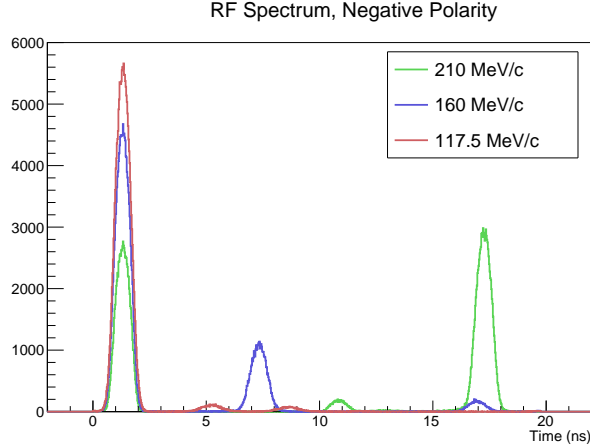


FIG. 2. Measured RF time spectrum for negative charge beams at 117.5 MeV/ $c$ , 160 MeV/ $c$ , and 210 MeV/ $c$ , at a distance of  $\approx 23.5$  m from the production target. The peaks from left to right are  $e$ ,  $\pi$ ,  $\mu$  for 117.5 MeV/ $c$  and 160 MeV/ $c$ , and  $e$ ,  $\mu$ ,  $\pi$  for 210 MeV/ $c$ . The absolute scale is arbitrary. The 3 – 6 ns separation is large compared to the intrinsic width in time of the particle peaks of  $\approx 300$  ps. The spectrum wraps around every  $\approx 20$  ns.

The  $\pi$ M1 channel transports mixed secondary beams of  $e$ 's,  $\mu$ 's,  $\pi$ 's and protons (for high momenta) generated by interactions of the primary proton beam at the M1 production target. The accelerator time structure of  $\approx 50$  MHz leads to  $\approx 300$  ps ( $\sigma$ ) wide pulses of each particle type every  $\approx 20$  ns. MUSE uses beam momenta of 115, 153, and 210 MeV/ $c$  to provide good  $e$  and  $\mu$  fluxes at momenta where the particles arrive separated in time at the MUSE scattering target - see Fig. 2. The beam spot size is  $\approx 1$  cm ( $\sigma$ ) at the scattering target, with angular divergences  $\approx 1^\circ - 3^\circ$ . More details regarding the properties of the beam are given in Section III A.

The  $\pi$ M1 beam properties coupled with the need to measure precise cross sections make it necessary to measure incoming beam particles to identify each particle type and determine its trajectory. To accomplish this, we limit the beam flux to  $\approx 3.3$  MHz with a collimator at the intermediate focal point of the beam line. At this point the beam is  $\approx 5$  cm high and momentum dispersed to a width of  $\approx 21$  cm, for the 3% channel momentum acceptance. We reduce the momentum acceptance.



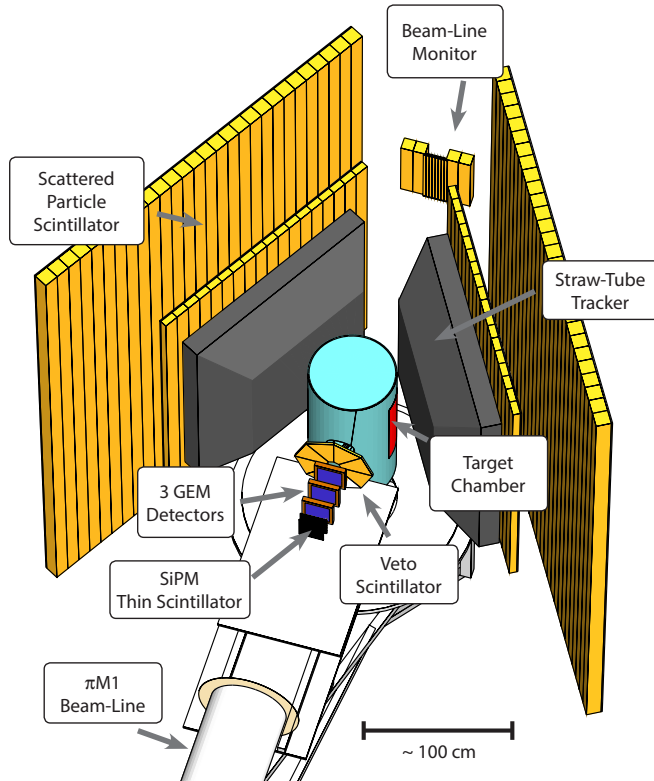


FIG. 3. Implementation of detectors in the  $\pi$ M1 area in a Geant4 [10] simulation. The beam strikes the thin scintillator beam hodoscope and three GEM chambers, passes through a hole in the annular veto scintillator, enters the cryotarget vacuum chamber and strikes one of the targets, then exits the vacuum chamber and goes through the beam monitor. Scattered particles are detected by two symmetric spectrometers, each with two straw chambers wrapped in RF shielding and two planes of scintillator paddles.

## B. Experimental Equipment

Figures 3 and 4 shows the MUSE experimental equipment in the target region. After exiting the channel, the beam passes through the beam hodoscope, a fast scintillator array that determines particle type through time measurements, relative to the accelerator RF. The beam next passes through GEM chambers to measure the trajectories going into the target. An annular veto detector surrounds the beam as it enters the vacuum chamber thin entrance window. Particles going through the veto detector are mainly muons from pion

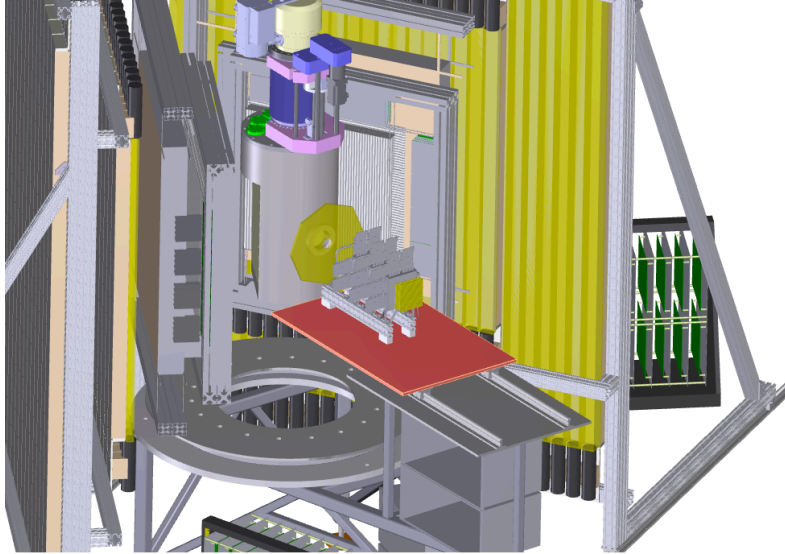


FIG. 4. CAD drawing of the experiment, showing some of the detectors, support structures, and electronics, and the cryotarget vacuum chamber.

decay,<sup>1</sup> which would hit the thick vacuum chamber wall, and might otherwise trigger the system. A target ladder inside the vacuum chamber holds the liquid hydrogen cryotarget, an empty cell for background measurements, and a solid alignment target. The ladder can be moved so that no target is in the beam. Downstream of the target is a beam monitor that monitors beam particles that do not scatter in the cryotarget. The beam monitor is also used in conjunction with the beam hodoscope to determine the  $\mu$  and  $\pi$  beam momenta through time of flight techniques.

Symmetric left and right spectrometers detect particles that scatter in the cryotarget at angles of  $20^\circ$  -  $100^\circ$ . The spectrometers consist of straw chambers for tracking and scintillator walls for precision timing measurements. The two symmetric spectrometers are intended both to double the experimental statistics, and give simultaneous but independent cross section measurements that provide an overlap and check of some of the experiment systematics.

The pion scattering rate from the strong interaction is much greater than the rates of interest, the electron and muon scattering rates from the electromagnetic interaction.

---

<sup>1</sup> At MUSE beam momenta,  $\pi$ 's decay at a rate of  $\approx 10\%/m$ , while  $\mu$ 's decay at a rate of  $\approx 0.1\%/m$ .

Thus the experiment uses a trigger that includes beam particle identification, scattered particle detection, and no veto signal.

Detector performance requirements arise from several different considerations. Detector time resolutions need to be at the  $\approx 100$  ps / plane level, so that time of flight between detectors can be measured to  $\leq 100$  ps. This is needed for beam momentum measurements and for identifying reaction types. Trigger detector efficiencies need to be at the  $\approx 99\%$  level, to not lose statistics, to reject pion induced backgrounds, and to control any angle-dependent inefficiencies that might change the angular distribution shape, and the extracted proton radius. Chamber position resolutions need to be at the 100 - 150  $\mu\text{m}$  level, with relative orientations at the sub-mm level, so that calibrations can precisely determine the chamber coordinates. This is because the measured cross sections are sensitive to systematic offsets in the scattering angle, particularly at forward angles where the electromagnetic cross section varies rapidly with angle. More details on the requirements are given in the detector sections.

### C. Rates, Accidentals, Statistics

Singles and trigger rates are presented in Table II for all kinematic settings. Elastic scattering is calculated from measured form factors, and singles and trigger rates from all processes are estimated with Geant4 simulations. We also consider backgrounds, discussed in Section A. The estimates use beam fluxes given in Table III in Section III A, the detector configuration shown in Fig. 3, and a 6 cm thick LH<sub>2</sub> target, with 0.125 mm thick kapton entrance and exit windows. The trigger rates are based on sufficient energy being deposited in two planes of scintillator paddles, no hit detected in the veto scintillator, and the efficiency of the beam PID system at rejecting  $\pi$  events at the trigger level – see Section V B. The singles rate is the integrated rate for all scintillator paddles in one wall, which is dominated by forward-angle particles, with the most forward scintillator paddle having up to about one-third of the total rate quoted. Background rates that were cross-checked with standalone estimates include  $\pi^\pm p$  scattering, evaluated using the SAID partial wave analysis, available online at <http://gwdac.phys.gwu.edu/>, and particle decays in flight.

TABLE II. Rates for both detector arms combined for various processes in Hz with the estimated beam fluxes totaling 3.3 MHz for all particle types. The “+(-)” momenta indicate positive (negative) polarity particles. For elastic processes from the target the singles and trigger rates are basically equal, but for particles from decays in flight or low-energy particles knocked out of the target this is not the case. The rates are for both detector arms combined.

Momentum (MeV/c)	+115	+153	+210	-115	-153	-210
$\mu + p$ <b>elastic scattering</b>	<b>0.6</b>	<b>2.6</b>	<b>1.0</b>	<b>0.3</b>	<b>0.7</b>	<b>0.5</b>
$\mu$ +kapton elastic scattering	0.8	2.0	0.4	0.4	0.5	0.2
Geant4: $\mu$ singles	590	1452	680	278	387	352
Geant4: $\mu$ triggers	96	384	136	55	96	76
$e + p$ <b>elastic scattering</b>	<b>54</b>	<b>20</b>	<b>1.9</b>	<b>55</b>	<b>28</b>	<b>7.5</b>
$e$ +kapton elastic scattering	21	6.6	0.5	22	9.5	2.0
Geant4: $e$ singles	77309	47691	8820	89036	73080	36942
Geant4: $e$ triggers	2619	1386	288	2465	2070	1128
Geant4: $\pi$ singles	8442	126750	274960	5176	34660	152341
Geant4: $\pi$ triggers	2340	43725	85360	1393	11948	42630
Geant4: $\pi$ triggers + beam PID	0	0	0	0	0	0
Total singles rate	86341	175893	284460	94489	108126	189635
Total Geant4 triggers + beam PID	2715	1774	433	2520	2167	1208

The Geant4 triggers in Table II exceed the elastic triggers, mainly from interactions with the upstream beam line detectors scattering particles straight into the scintillators to generate a trigger. These events are removed at the analysis stage through the reconstructed target vertex, which is far from the actual target. The highest DAQ rates of nearly 4 kHz come from electrons at negative polarity. Our goal is for the DAQ system to be able to read out an event in 0.1 ms, which would lead to a 20% dead time at 2 kHz trigger rate. Given the ratio of electron scattering to muon scattering events, the DAQ rate can easily be reduced to a more manageable level by prescaling the electron triggers. There are additional triggers described in Section VB that are not in Table II but which will be read out by the DAQ.

The highest total background singles rate of about 280 kHz contaminates  $\approx 3\%$  of the event data, assuming a 100 ns time window, the scale of the straw chamber drift times. A more significant random background is the  $\approx 6.5\%$  probability of a second beam particle

in the same RF bucket as the triggering beam particle. The potential statistical precision gained from including these events is outweighed by the potential that their inclusion changes the shape of the angular distribution, and the extracted radius.

The number of counts measured is related to the cross section by

$$N_{counts} = N_{beam} \times (x\rho)_{target} \times \frac{d\sigma}{d\Omega} \times \Delta\Omega \times \epsilon , \quad (1)$$

where  $N_{counts}$  is the number of elastic events counted,  $N_{beam}$  is the number of beam particles,  $(x\rho)_{target}$  is the target areal density,  $\frac{d\sigma}{d\Omega}$  is the elastic differential cross section,  $\Delta\Omega$  is the detector solid angle, and  $\epsilon$  accounts for all efficiency factors (detection, electronic, data acquisition, and analysis efficiencies) and radiative corrections. We estimate that we typically lose about 30% of potential events due to a combination of detector inefficiencies (hardware and reconstruction), accidental secondary beam particles, target fiducial cuts, and DAQ live time.

With the planned MUSE system and a two-calendar-year production run, the planned statistical precision of MUSE is  $\approx 1\%$  for muons in our lowest precision bins, well below 1% in most of our kinematic range, and typically several times better for electrons. The statistical uncertainty has a small increase from subtraction of the target wall background. For muons, there is an additional small increase in the uncertainties from the subtraction of the muon decay background. These and other factors are considered in leading to the projected data shown in Section VII A 4.

#### D. Systematics

To obtain precise cross sections and a precise proton radius, systematic precision is required as well as statistical precision. The main systematic issue in electromagnetic scattering is that the cross sections changes rapidly with angle for low  $Q^2$ , forward-angle data, and with energy, due to the kinematic factors in the cross section. These issues are analyzed in Appendix B. The main result of these studies is that we can control changing the shape of the angular distributions significantly by determining detector orientations at the sub-mr level, by determining beam momentum at the  $\approx 0.3\%$  level, and by correcting for the effects of multiple scattering through Monte Carlo. The necessary calibration procedures are discussed elsewhere in this report.

### III. THE $\pi$ M1 BEAM LINE AND DETECTORS

#### A. Beam Properties

##### 1. Measured Beam Properties

The  $\pi$ M1 beam line views the proton beam spot on the M1 target at an angle of  $22.5^\circ$  relative to the proton beam. The pion production region viewed by  $\pi$ M1 has a size about 2 mm horizontal (full width) by 2.9 mm vertical ( $2\sigma$ ) by 13 mm along the  $\pi$ M1  $z$  axis ( $6\sigma$ ). The  $\pi$ M1 channel nominal acceptance is about 6 msR solid angle and with a 3% momentum bite. The channel includes focusing quads, two dipoles which each bend the beam  $75^\circ$  in the horizontal direction, and two sets of jaws. The default tune is point-to-point, producing an image of the production target at a path length distance of about 23.5 m. Detailed properties of the channel magnets (field maps) do not exist, and it is understood that the fields of the upstream quads are distorted by the steel enclosures.

Except for a Hall probe is mounted in the downstream dipole, channel magnet stability is only monitored through the power supply currents. The dipole field appears to generally have been stable to better than  $10^{-4}$  during our test runs.

The  $\pi$ M1 channel has previously mainly been used and studied for  $\pi$  beam properties, we have now studied the  $\mu$  and  $e$  beam properties as well. Here we present several examples.

Figure 5 shows the beam distribution measured with a GEM telescope (see Sec. III B 3), projected to the target position. The beam width obtained varies with momentum but is independent of particle type. At the central momentum setting, the nominal beam spot ( $\sigma$ ) is  $\approx 0.8 \times 0.9$  cm<sup>2</sup>. The angular divergence of the beam was found to be at worst (lowest momentum)  $\sim 24$  mr ( $\sigma$ ) in the horizontal direction and  $\sim 15$  mr ( $\sigma$ ) in the vertical direction. These results are similar to the nominal  $\pi$ M1 characteristics at [http://aea.web.psi.ch/beam2lines/beam\\_pim1.html](http://aea.web.psi.ch/beam2lines/beam_pim1.html). In the MUSE experiment, the detectors in the beam cause multiple scattering, which makes the beam spots on target slightly different for different particle types.

The  $\pi$ M1  $\pi$  and  $e$ , but not  $\mu$ , fluxes were measured by Schumacher and Sennhauser in 1987 [11]. The RF time spectrum – see Fig. 2 – was measured at several beam momenta to determine particle fractions for each polarity, shown in Fig. 6. (We have not had

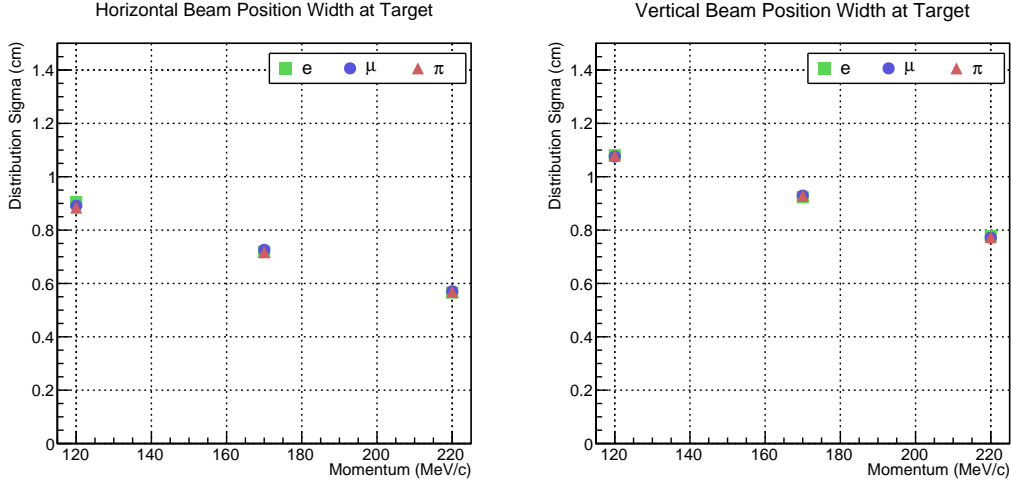


FIG. 5. Width ( $\sigma$ ) of the beam as measured in the June 2014 test setup with GEM chambers as a function of momentum and particle type.

the appropriate equipment and readout to measure the absolute beam flux.) Combining the absolute measurements of [11] scaled to a 2.2 mA primary proton current with our fractional measurements results in the fluxes given in Table III. No protons were observed in the channel in our momentum range.

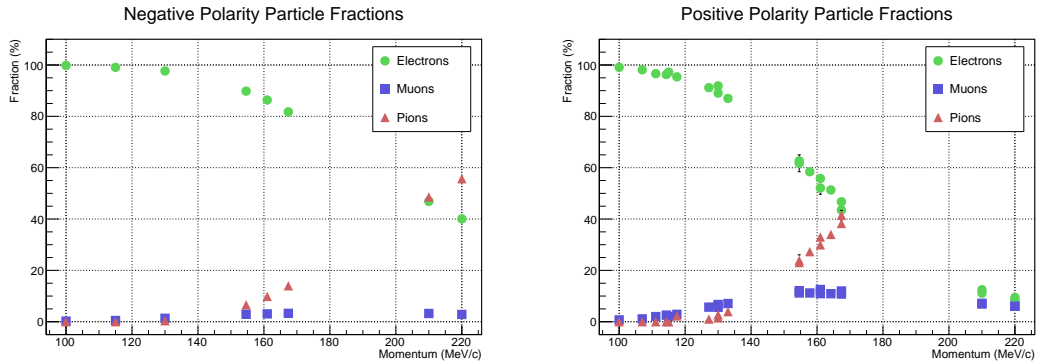


FIG. 6. Measured particle fractions versus beam momentum as measured in June 2013.

We studied beam properties at the IFP, using a SciFi detector, and compared the results to TURTLE simulations. The simulated  $\pi$  beam envelope at the IFP is 22.5 cm wide (full width at 10% maximum), with sharp edges and a momentum dispersion of 7 cm/%, and roughly Gaussian in the vertical direction with width  $\sigma = 0.60$  cm, and no visible tails

TABLE III. Beam flux at the target for full  $\pi$ M1 channel acceptance with 2.2 mA primary proton current. The total flux is based on previous measurements, while the relative fluxes of each particle types are based on MUSE measurements. Also shown in parentheses is the flux of each particle type when the combined flux is limited to the MUSE planned total flux of 3.3 MHz.

Momentum (MeV/c)	Polarity	Total Flux (MHz)	$e$ Flux (MHz)	$\mu$ Flux (MHz)	$\pi$ Flux (MHz)
115	+	8.3	8.05 (3.20)	0.17 (0.07)	0.08 (0.02)
153	+	16.9	10.65 (2.08)	2.03 (0.40)	4.23 (0.83)
210	+	79.2	9.50 (0.40)	6.34 (0.26)	63.36 (2.64)
115	-	7.4	7.29 (3.25)	0.07 (0.03)	0.04 (0.02)
153	-	11.9	10.71 (2.97)	0.38 (0.11)	0.81 (0.22)
210	-	24.0	11.28 (1.55)	0.96 (0.13)	11.76 (1.62)

outside  $\pm 2.25$  cm. The measured beam that reached the scattering target came through the IFP in a region about 20 cm wide by 5 cm high, with significant uncertainty in the horizontal direction.

We checked the momentum dispersion of  $\pi$ 's and  $\mu$ 's in the channel by using a collimator slot at the IFP and measuring both the shift in the RF time at the target and time of flight between two scintillators. All data to date are consistent within uncertainties with the expected 0.14%/cm.

## 2. Beam Simulations

We have implemented in our Geant4 [10] simulation a realistic beam parameterization based on our measured beam properties. The beam properties are similar to TURTLE predictions of the parent particle distributions.

Figure 7 shows the horizontal beam width for the measured data (triangles) and for the simulated beam distribution (circles) for electrons at 115 MeV/c and 210 MeV/c, respectively. Similar results are obtained for the vertical beam width and for other beam momenta and polarities. The simulation adequately reproduces the measured beam properties.

The realistic beam parameterization allows the prediction of beam properties in the



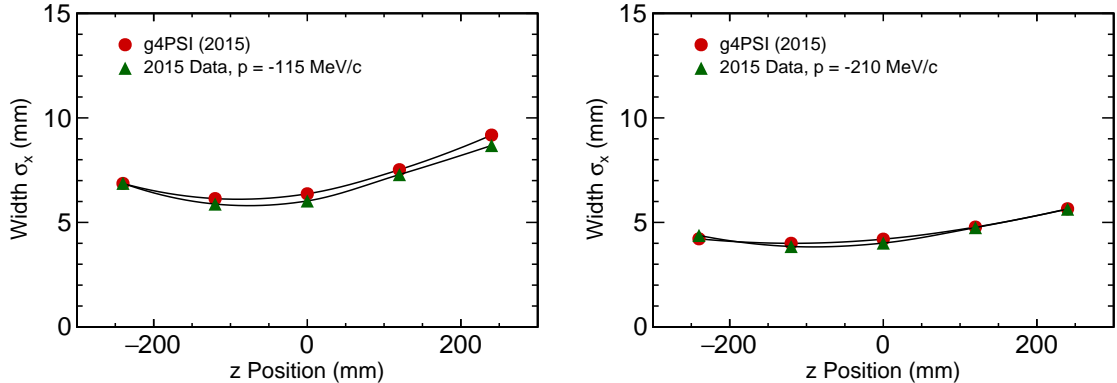


FIG. 7. Comparison of measured (triangles) beam widths  $\sigma_x$  at various positions with simulated beam distributions (circles). The simulation is based on beam parameters which were tuned to fit the experiment. The examples are for electrons at beam momenta of 115 MeV/c and 210 MeV/c, respectively.

presence of the MUSE beam line detectors. Figure 8 shows the minimum radial distance from the beam axis that encloses a certain fraction of primary beam particles. The panels are for different beam particles: *geantinos* (green), which do not interact in the simulation, electrons, muons, and pions in red. The effect of multiple scattering in air and, especially, in detector components starting at about  $z = -40$  cm, is evident. The distributions in Fig. 8 are for a beam momentum of 115 MeV/c, where the effect of multiple scattering is largest. The target radius of 3 cm is indicated as horizontal dotted line. The electron and muon beams almost fully pass through the target at about  $z = 0$  cm. A more quantitative measure of useful beam particles is the fraction of primary particles which enter the target volume within  $r < 2.5$  cm and  $5^\circ$  in the forward direction. An overview of these fractions is given in Table IV for two setup options: one with two and one with four beam hodoscope detectors just upstream of the three GEM detectors.

## B. Beam Line Detectors

### 1. Beam Cerenkov

*a. Purpose:* The beam Cerenkov provides a high-resolution timing measurement at the IFP for RF time and time-of-flight (TOF) determinations. In order to minimize

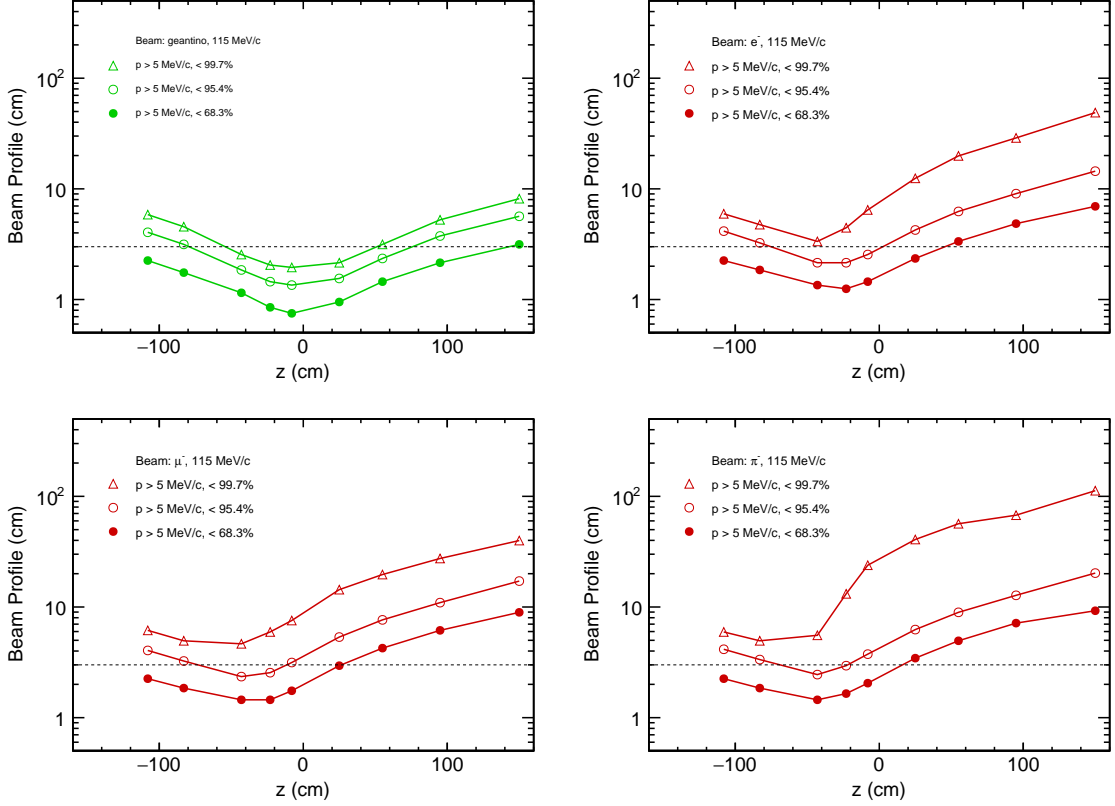


FIG. 8. Evolution of the beam profile along the beam line from simulation for various particle types at 115 MeV/c incident particle momentum. The curves show distances from the beam axis which enclose the given fractions of beam particles with at least 5 MeV/c momentum. The effect of multiple scattering in the MUSE setup is included for  $e^-$ ,  $\mu^-$ , and  $\pi^-$  (red); the *geantino* particles (green) do not interact and reflect the original beam distribution. The dashed line marks the size of the target with  $r = 3$  cm.

material in the beam line for regular experimental running, the beam Cerenkov detector will only be used for calibration and background measurements, not for regular data taking.

*b. Requirements:* The requirements for the Cerenkov detector are laid out in table V.

*c. Detector design:* The design is based on the work of Albrow *et al.* [12], who obtained timing resolution better than 10 ps ( $\sigma$ ) with a beam Cerenkov, using thick quartz bars read out through a Photech PMT240 multichannel plate (MCP) with an Ortec

TABLE IV. Fraction of selected beam particles entering the target volume for the MUSE setup including 2 or 4 SiPM detectors and 3 GEM planes.

Particle	two SiPM			four SiPM		
	115 MeV/c	153 MeV/c	210 MeV/c	115 MeV/c	153 MeV/c	210 MeV/c
$e^+$	0.943	0.976	0.989	0.922	0.968	0.986
$\mu^+$	0.881	0.969	0.989	0.832	0.955	0.989
$e^-$	0.950	0.977	0.989	0.929	0.972	0.987
$\mu^-$	0.887	0.969	0.991	0.843	0.959	0.990

TABLE V. Cerenkov detector requirements

Parameter	Performance Requirement	Achieved
Time Resolution	<80 ps	✓ <60 ps
Efficiency	99% for e, $\mu$	99% $\pm$ 2%
Positioning	$\approx$ 1 mm, $\approx$ 20 mr	not attempted, easy
Rate Capability	2.5 MHz	✓ 3 MHz

9327 preamp/CFD. The time resolution extrapolates to  $\approx$ 50 ps in MUSE experimental conditions, as we use thinner radiators to minimize effects on our lower energy beam. We use the same MCP and preamp/CFD as Albrow *et al.* We tilt the Cerenkov plate at close to the muon Cerenkov angle, to provide good efficiency for all particle types.

*d. Current status:* We have achieved better than 90 ps time of flight resolution between our prototype beam Cerenkov – see Fig. 9 – and a fast scintillator in tests in  $\pi$ M1, corresponding to a Cerenkov resolution of 50 - 60 ps. Examples of the test data taken are shown in Fig. 10. Rate dependence tests of the beam Cerenkov response up to 3 MHz of incident particles show no effects on the analog output pulse shape.

*e. Path to completion:* We descope further beam Cerenkov development and construction after adopting the beam hodoscope technology. The existing detector remains in PiM1, ready for installation and use in MUSE as needed. We will retest the detector before the experiment to ensure it is ready if needed.

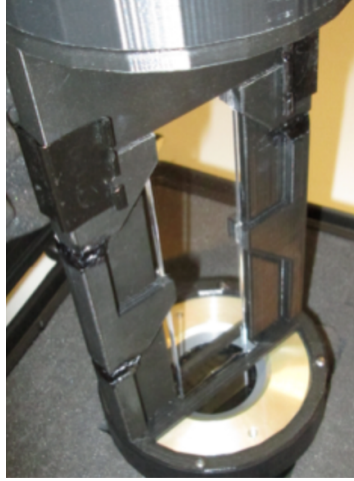


FIG. 9. Quartz plate mounted on a PMT240 with a 3d printed mounting fixture, during the June 2015 test run. The assembly is wrapped in tedlar for light tightness.

## 2. Beam Hodoscope

*a. Purpose:* The beam hodoscope provides precise timing information for beam particles, along with position information. The beam hodoscope timing information will be used in conjunction with the RF signal to provide beam particle identification at low precision for the trigger and at high precision for the event analysis. Time of flight from the beam hodoscope to the scattered particle scintillators, determines the reaction type, in particular separating muon decay from muon scattering. Time of flight from the beam hodoscope to the beam monitor allows an RF time vs. time of flight comparison that confirms particle identification, helps to identify backgrounds, and determines the muon and pion beam momenta. The beam hodoscope also counts the total incident beam flux, and through sampling randomly coincident beam particles determines the flux of each particle type.

*b. Requirements:* The requirements for the beam hodoscope detector are laid out in Table VI. The time resolution requirement allows the needed time of flight resolution from the combination of multiple planes of beam hodoscope to the scintillator walls. The

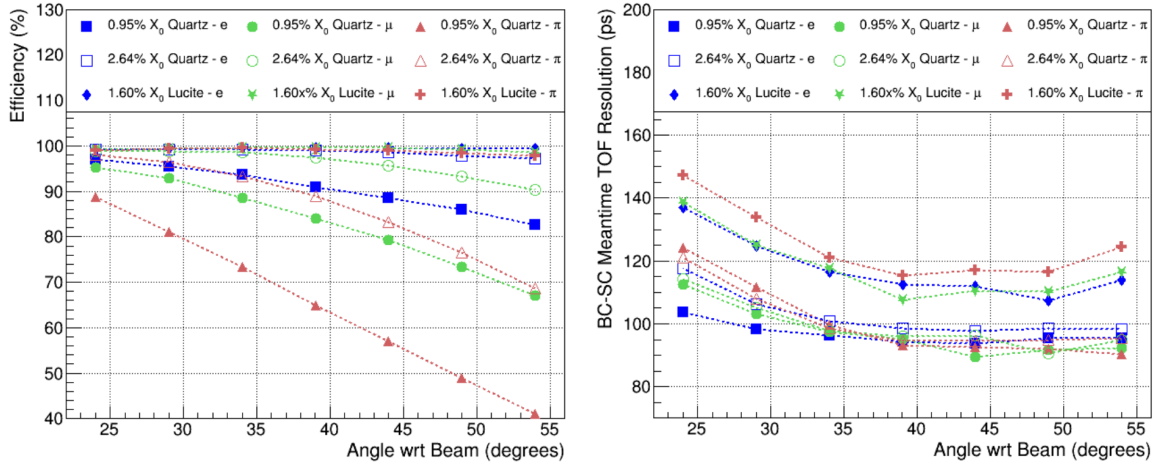


FIG. 10. Left: efficiency data for the beam Cerenkov prototype for 3 radiators. Systematic uncertainties on the efficiencies are a few percent. Right: time of flight resolution between the beam Cerenkov and a fast scintillator.

TABLE VI. Beam hodoscope detector requirements

Parameter	Performance Requirement	Achieved
Time Resolution	<100 ps / plane	✓ 80 ps
Efficiency	99%	✓ 99.8%
Positioning	≈1 mm, ≈1 mr	not attempted; easy – calibrated by data
Rate Capability	3.3 MHz / plane	✓ >10 MHz / plane

efficiency allows efficient collection of statistics and rejection of pion induced events. The positioning requirement is to align the beam hodoscope to the GEM chambers, allowing efficient analysis when there are randomly coincident additional beam particles within the detector time windows. The rate capability allows the full planned beam flux of  $\approx 3.3$  MHz to be observed at high efficiency.

*c. Detector design:* A beam hodoscope plane under construction is shown in Fig. 11. We use BC-404 scintillator, with 6 central paddles of size 10 cm long  $\times$  4 mm wide  $\times$  2 mm thick, flanked by 5 outer paddles on each side of size 10 cm long  $\times$  8 mm wide  $\times$  2 mm thick. This gives 16 paddles, and 32 readout channels per plane. The paddles are glued to SiPMs which are mounted on custom printed circuit boards (PCBs). A foil is used during assembly to position the paddles 6  $\mu$ m apart, to provide an air gap and total

internal reflection to capture much of the light within the paddles, to be directed to the SiPMs at each end. The active area is  $\approx 10 \text{ cm} \times 10.4 \text{ cm}$ .

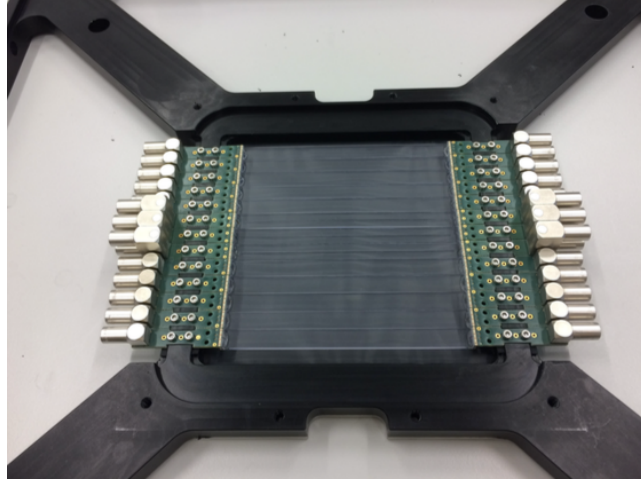


FIG. 11. A beam hodoscope plane of thin scintillators with SiPM readout under construction.

The Hamamatsu S13360-3075PE SiPMs have an active area of  $3 \text{ mm} \times 3 \text{ mm}$  in a housing about  $4 \text{ mm} \times 4 \text{ mm}$ , a peak quantum efficiency near 50% at  $\approx 450 \text{ nm}$ , and a gain of about  $4 \times 10^6$  at operating voltage. For the central 6 paddles we use PCBs that house 2 SiPMs operating independently to read out 2 4-mm paddles - the PCBs with double LEMO connectors in Fig. 11. For the outer 10 flanking paddles we use PCBs that house 2 SiPMs connected in series and reading out the same paddle - the PCBs with single LEMO connectors in Fig. 11. We operate the single SiPMs at  $\approx 55 \text{ V}$ , and the two SiPMs in series at  $\approx 110 \text{ V}$ .

The beam hodoscope analog signal is amplified to produce a fast signal with a 1.2 ns rise time, a 3.0 ns fall time, and typically a few hundred mV peak. See Fig. 12. For read out, the amplified analog signal is sent to a Mesytec CFD, which, in turn, sends an analog copy of the signal to the Mesytec QDC input, and the discriminated signal to the TRB3 TDC, to the trigger, and (an OR of 16 such signals) to the Mesytec QDC gate.

We will build 4 planes of the beam hodoscope detector. All 4 planes will be used at the planned highest beam momentum of  $210 \text{ MeV}/c$ . Due to the effects of the beam hodoscope on the beam, and the less precise timing requirements at lower beam momentum, the number of planes installed will be reduced to 3 at  $153 \text{ MeV}/c$ , and 2 at  $115 \text{ MeV}/c$ .

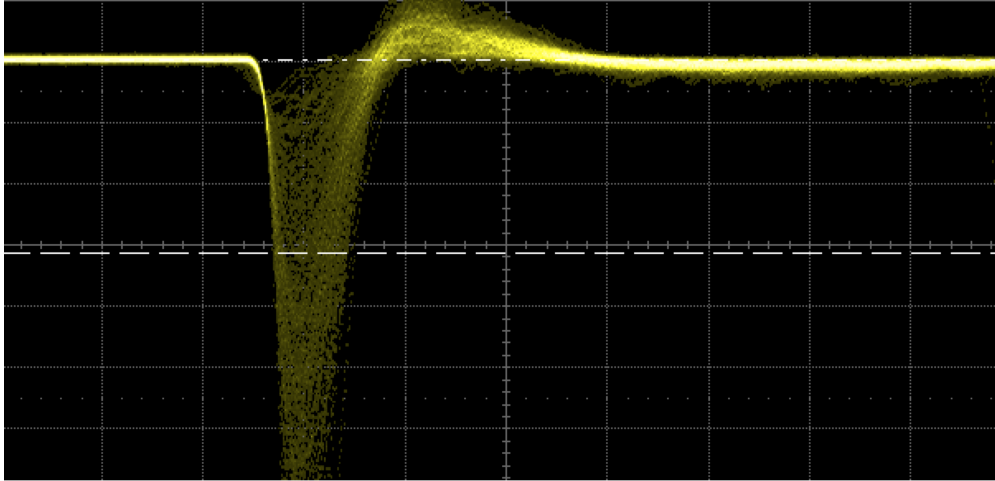


FIG. 12. A scope trace of amplified beam hodoscope prototype paddle signals. The horizontal scale is 5 ns / division. The vertical scale is 100 mV / division.

*d. Current status:* The beam hodoscope design results from extensive prototyping of scintillator materials (BC-404, BC-418, BC-420, BC-422), SiPMs (various Hamamatsu and AdvanSiD models), geometries (lengths of 10 and 16 cm, widths of 4 mm, 5 mm, 8 mm, and 12 mm). Both individual paddles and few-element hodoscopes were tested, to also study cross talk. Radiation damage of the SiPMs and recovery was also studied, to ensure adequate lifetime of the detector. SiPM performance was measured with them in the beam, for a total particle flux exceeding Monte Carlo estimates of annual dosage.

The first beam hodoscope plane has now been constructed, but not yet tested. An initial set of amplifier PCBs have been built and are undergoing testing, to verify performance before the full set of PCBs are constructed.

Two sample results from prototype tests follow. Figure 13 shows efficiency measurements and a timing spectrum from one of the SiPM detectors. Both 5- and 12-mm wide paddles had  $99.9\% \pm 0.1\%$  efficiencies with properly-set thresholds at the recommended operating voltages. The 12-mm Advansid paddle had 3 APDs connected in series, so it required  $3\times$  the operating voltage and threshold of the single APD 5-mm paddle. Resolutions for bars, averaging both ends, were less than 100 ps for most configurations.

*e. Path to completion:* All components necessary to construct the beam hodoscope detector have been purchased and are on hand, with the exception of four detector frames,

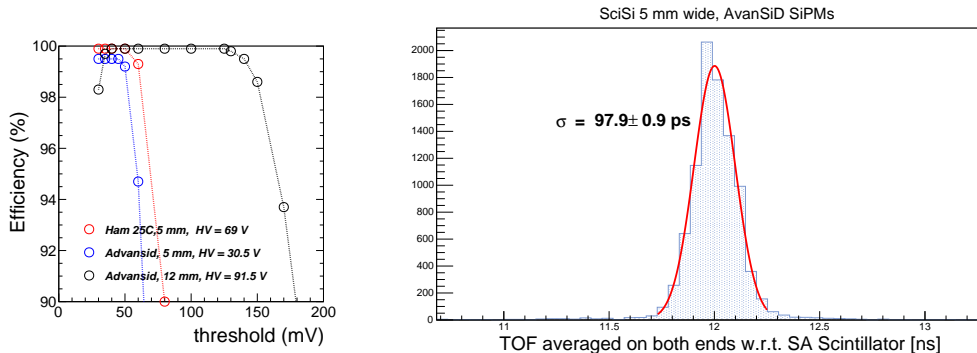


FIG. 13. Left: Efficiency for several paddles as a function of threshold. Right: Time resolution of a SiPM paddle, using the average of both ends, for events with muon RF time in fast scintillator.

which are now being machined. The additional planes will be assembled in 2017 and early 2018. The amplifier PCBs will be assembled after the performance of the initial set of PCBs is verified.

### 3. GEM Chambers

*a. Purpose:* Measuring high-precision cross sections requires knowledge of the scattering angle on an event-by-event basis at the level of several mr, but the divergence of the beam is  $\approx 15 - 25$  mr ( $\sigma$ ). Thus high-resolution tracking detectors are needed to measure trajectories into the target to reconstruct the scattering kinematics.

The most effective solution for tracking a several MHz beam with  $< 100$   $\mu\text{m}$  resolution is the use of GEM (Gas Electron Multiplier) detectors. GEMs have been demonstrated to withstand harsh radiation environments while maintaining high resolution and efficiency for single events and show little to no aging effects. GEMs have been successfully operated at intense high-energy muon beams at the COMPASS experiment at CERN, which has served as a role model for the development of GEMs in many other experiments and applications. They are low-mass detectors of order 0.5% of a radiation length, thus keeping multiple scattering at a minimum. Resolutions of  $50 - 100$   $\mu\text{m}$  are typically achieved with a two-dimensional strip readout at some  $400$   $\mu\text{m}$  pitch. This way the amplified charge is distributed over several readout strips as a few-mm wide cluster, which allows for an improved resolution smaller than the pitch by using a centroid weighting technique. The



TABLE VII. GEM detector requirements

Parameter	Performance Requirement	Achieved
Resolution	100 $\mu\text{m}$ / element	✓ 70 $\mu\text{m}$
Efficiency	98%	✓ 98%
Positioning	$\approx 0.1$ mm, $\approx 0.2$ mr	not attempted; easy
Rate Capability	3.3 MHz / plane	✓ 5 MHz
Readout Speed	2 kHz / 20% deadtime	1 kHz / 100% deadtime

two-dimensional hit information from several GEM detectors is combined to determine the beam trajectory. The reduced number of electronics channels and a rather simple construction scheme makes GEM detectors very cost-effective.

*b. Requirements:* The GEMs for beam particle tracking are required to provide 100  $\mu\text{m}$  resolution and  $>98\%$  efficiency per element at operation of 3.3 MHz beam flux. The requirements are presented in Table VII.

*c. Detector design:* The Hampton group developed, built, and successfully operated a set of  $10 \times 10$  cm<sup>2</sup> GEM detectors at the OLYMPUS experiment at DESY [13, 14]. At OLYMPUS, these GEM detectors were used for monitoring of the luminosity by determining the forward-angle elastic  $ep$  scattering rate on an event-by-event basis. These GEM detectors became available for the proposed MUSE experiment at PSI in the course of 2013, after OLYMPUS data taking was completed. The GEM elements were identified as US (upstream), MI (middle), and DS (downstream), left and right sector in OLYMPUS and this nomenclature will also be used for MUSE.

The  $10 \times 10$  cm<sup>2</sup> OLYMPUS GEMs are operated with a 70% Ar / 30% CO<sub>2</sub> gas mixture and are read out with strips in two dimensions with a pitch of 400  $\mu\text{m}$ . The design of the GEM stack parameters such as the drift gap and gaps between the three GEM layers and the readout plane follow that of the COMPASS design, which has been demonstrated to provide reliable detection of hit locations at routine rate densities of 2.5 MHz/cm<sup>2</sup> and of up to 25–100 MHz/cm<sup>2</sup> in dedicated tests. The expected rate density for the nominal  $\pi\text{M1}$  tune at the final GEM just upstream of the target is about  $3.3 \text{ MHz} / 5 \text{ cm}^2 = 0.66 \text{ MHz/cm}^2$ , with a single-track probability of over 90%. Because the beam is coming to a focus, the upstream GEMs will have a smaller rate density. The OLYMPUS GEMs are

therefore very well suited to provide event-by-event beam particle tracking under these conditions.

The GEMs are read out using FPGA-controlled frontend electronics based on the APV-25 chip developed for CMS and digitized with the Multi-Purpose Digitizer (MPD). The readout hardware was developed by INFN Rome and Genova for the Hall A SBS spectrometer in the framework of the 12 GeV upgrade of Jefferson Lab, and was used for the first time in a realistic setting at OLYMPUS. It consists of a frontend card hosting the APV-25 chip, which is directly attached to the GEM detector, and a VME based controller board (MPD) hosting an FPGA located several meters away. Each APV processes 128 readout channels and pipelines both analog and digital information of 128 channels on a single cable. Raw signals on all strips are sampled with either 20 or 40 MHz frequency. After adjusting the latency, “snapshots” of the analog signal are taken and sent as frames to the VME based controller.

The MPD controller provides clock, trigger and configuration via I2C to the APV, and receives and digitizes the raw data into on-board ADCs. The DAQ frontend software was realized for OLYMPUS by the Hampton group and has been running on a VME based single-board computer that controls the VME bus to read out and write the data to disk or to send it to the event builder. As each APV chip reads out 128 channels, a  $10 \times 10 \text{ cm}^2$  chamber corresponds to  $2 \times 250$  channels, which are read out with four frontend chips. One MPD can operate up to 16 APVs, *i.e.* one such controller can operate up to four GEMs, hence one telescope of three GEMS can be read out with a single MPD. The strip numbers and digitized pulse heights of the hit clusters in  $x$  and  $y$  give the spatial information for the track. Figure 14 shows the digitized pulse height after pedestal subtraction of a single event versus the strip number, of the US, MI, and DS GEM in both  $x$  and  $y$  direction (250 channels each). The red triangles indicate the candidate cluster locations returned by the cluster finding algorithm.

The GEM telescopes at OLYMPUS worked very well. Operation was very stable, noise levels were very low. At OLYMPUS, intrinsic resolutions were found to be around  $80 \mu\text{m}$ , and efficiencies around 93-95%, as shown in Figs. 15 and 16.

*d. Current status:* The GEM readout was successfully added into the MUSE MIDAS DAQ and used in beam tests starting in December 2013.

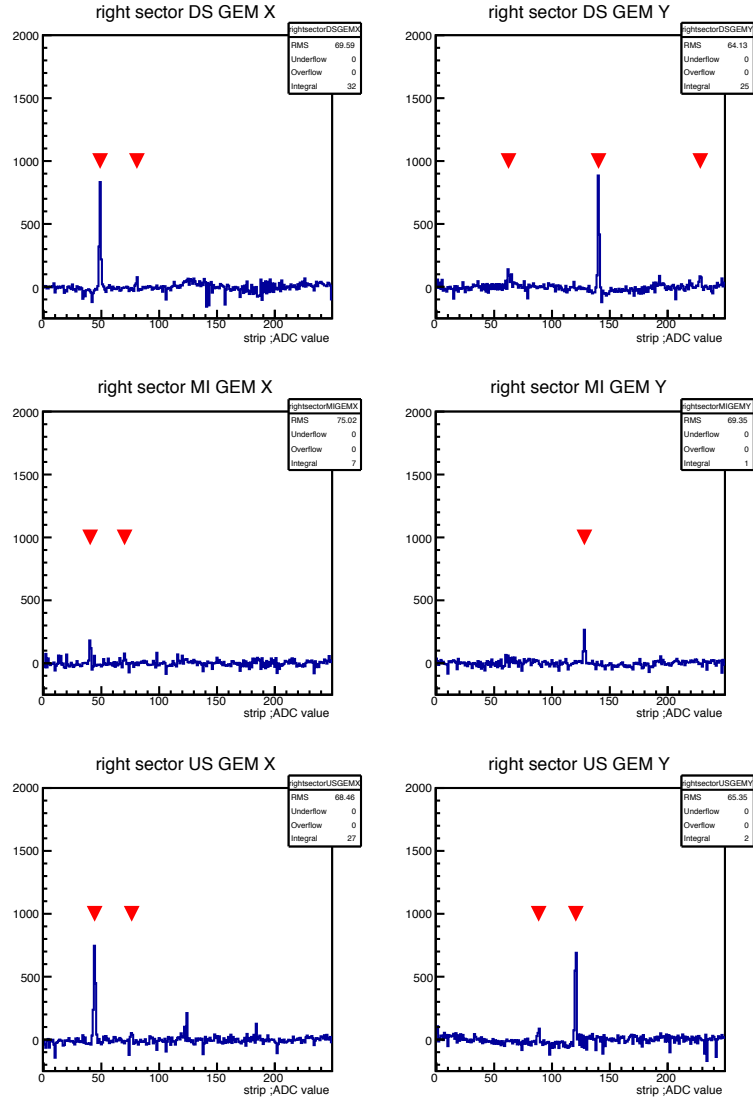


FIG. 14. ADC channel versus strip number in  $x$  and  $y$  direction for the US, MI, and DS GEM elements. The red triangles mark the location where the cluster finding algorithm yields a candidate cluster location.

An improved cluster finding algorithm to account for common-mode noise and channel-by-channel pedestal subtraction has been implemented, and the effect on chamber efficiencies has been studied in test beamtimes in December 2014 and summer 2015. The structures in the efficiency maps as seen e.g. in Fig. 16 have largely disappeared with the improved analysis scheme. As depicted in Fig. 17, efficiencies for each element are now above 98% with inefficiency patterns greatly reduced.

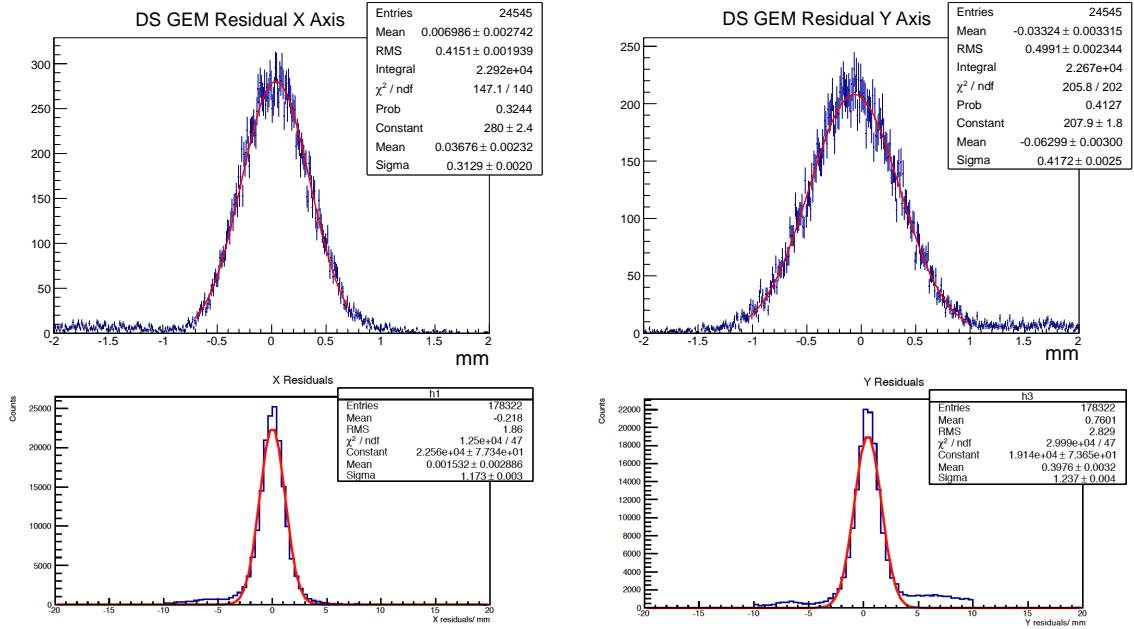


FIG. 15. Top: Track residuals from OLYMPUS fitted with 3 MWPC + 2 GEM elements. The residual width is composed of the intrinsic resolution and the track uncertainty. Intrinsic resolutions of around  $80 \mu\text{m}$  have been achieved for each GEM element. Bottom: Track residuals from the December 2013 test beam for MUSE beam trajectories in the GEM telescope fitted with 2 of 3 GEM elements. Residuals are bigger due to the less constrained tracks.

In summer 2015 the GEM telescope modification for the final configuration began with reduced gaps between GEM elements, which should be about 8 cm to optimize the balance between spatial resolution requirements and minimizing the effects of multiple scattering. In order to reduce the distance between two elements to less than 12 cm, it was required to re-arrange the APV cards such that they would be oriented within the plane of each GEM. At the same time, cabling was modified to accommodate the new geometry, and the length of the cables was reduced to less than 10 m from previously 25 m. Studies are ongoing to assess and optimize the noise situation.

Alongside modification of the digital and analog cables, we decided to upgrade the previous MPD v3 to v4. The v4 has standard HDMI-A front panel connectors for the analog cables instead of the previous, very uncommon, HDMI-B connectors. The migration to the new hardware has been challenging, as the operation of the new MPD version and firmware with the existing DAQ frontend software was unsatisfactory. In particular, the I2C ad-

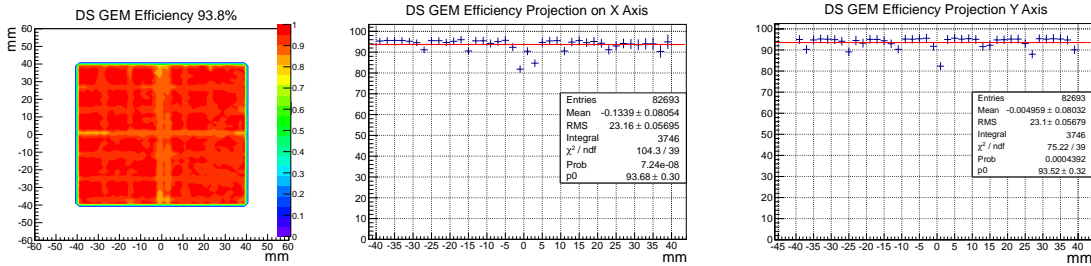


FIG. 16. Efficiency of the DS GEM element as a function of  $x$  and  $y$  at OLYMPUS. Tracks were identified and fitted with 3 MWPC + 2 GEM elements, in order to verify if the respective third GEM element shows a hit at the expected location. Some localized structures are visible related to weaker strips, which is under study. Efficiencies are generally around 93-95%.

dressings of the APVs was problematic, which delayed the successful re-commissioning of the telescope in the 2016 beamtimes. In spring 2017 we decided to retire the previous DAQ software and to migrate to the meanwhile mature INFN/JLab version of the code, which ran successfully at JLab in fall 2016. At the June 2017 PSI test beamtime, work is now in progress to meet the milestone of low-noise operation and reproduction of high efficiency. The new frontend software offers improved control features for the MPD and APV operation.

*e. Path to completion:* In the OLYMPUS experiment, the readout rate of the telescopes was  $\approx 100$  Hz. During the test beamtimes in 2014 and 2015 with one telescope, GEM readout required  $\approx 0.8$  ms, which would limit the DAQ rate to  $\approx 1$  kHz. In order to achieve a readout rate of order 2 kHz at less than 20% deadtime, an order of magnitude increase in readout speed is required.

With the hardware and software upgrades we also switched to a faster VME controller (XVB-601 replacing the V7768 model) and are going to establish in steps 32-bit and 64-bit block transfer, which together is expected to decrease the readout time by at least a factor 10, sufficient for MUSE operation. With the new controller, the VXS extensions of VME systems are also supported by all hardware elements, potentially allowing a significant further speed increase. The new DAQ software allows multi-frame readout of the APV cards, to be tested in the June 2017 beamtime. With multiple samples the event timing can be extracted. This can be used to suppress accidental hits occurring predominantly at high rates. For operation at the highest rates, we plan to migrate to MPD firmware

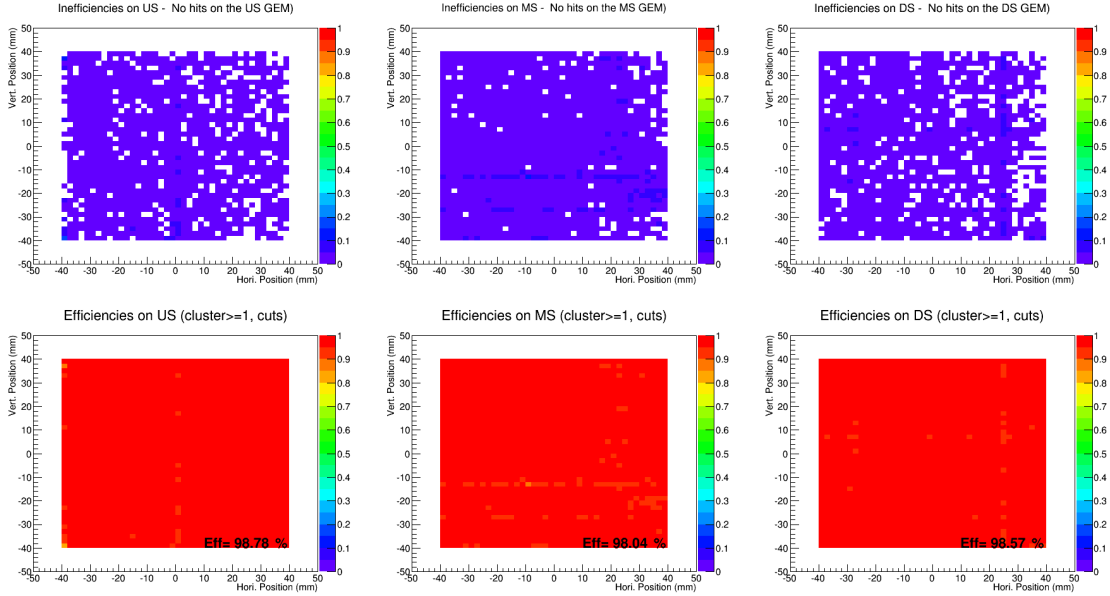


FIG. 17. Inefficiency maps (top row) and efficiency maps (bottom row) of the US, MI, and DS GEM element as a function of  $x$  and  $y$ , obtained in test beamtimes at PSI in summer 2015. Tracks were determined with 2 GEM elements, in order to verify if the respective third GEM element shows a hit at the expected location within 10 mm radius. Some localized structures are still visible related to weaker strips, but have been greatly reduced. Efficiencies are generally above 98%.

version 4 Extraction of the data from the MPD via optical link would then be possible. Following the scheme presently being implemented for the SBS setup at JLab, a Sub-System Processor (SSP) with a large FPGA collects the data from the MPD via optical link and performs real-time data reduction by applying common-mode correction and pedestal subtraction, zero suppression, and timing analysis in multi-sample readout mode to suppress accidental hits.

The system will be optimized in 2017 for its final configuration and operation.

#### 4. Beam Veto

*a. Purpose:* The beam veto detector is used to reduce trigger rate, by vetoing scattering or beam particle decay events upstream of the scattering chamber.

TABLE VIII. Beam veto detector requirements

Parameter	Performance Requirement	Achieved
Time Resolution	1 ns / plane	not attempted; easy
Efficiency	99%	not attempted; easy
Positioning	$\approx 1$ mm, $\approx 1$ mr	not attempted; easy
Rate Capability	1 MHz / plane	not attempted; easy

*b. Requirements:* The beam veto detector uses the same technology as the scattered particle scintillators of Section IV B, but with a modified geometry and only single-ended readout. The requirements are presented in Table VIII.

*c. Detector design:* The veto detector design is shown in Fig. 18. The veto detector is an approximately annular detector that surrounds the beam. It consists of 8 trapezoidal scintillators read out with Hamamatsu R13435 PMTs. The 3-cm inner radius matches the target vacuum chamber thin entrance window. Simulations were used to determine the veto detector coverage, leading to an outer radius of about 16 cm.

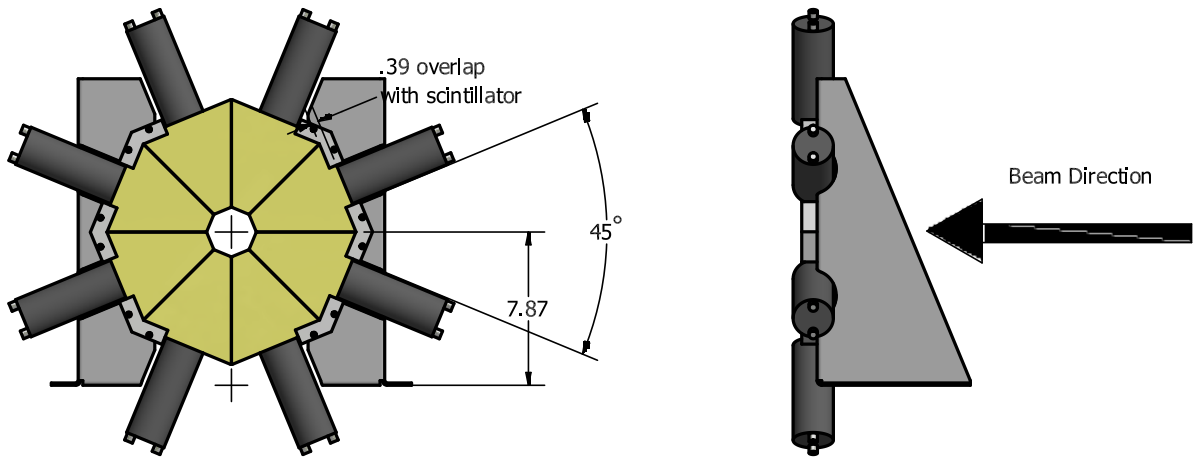


FIG. 18. Design of the beam veto detector and its frame. Dimensions are in inches.

*d. Current status:* The veto detector has been designed using the same technology as the scattered particle scintillators, but has more modest performance requirements. It has not been prototyped or tested in the planned veto geometry.

*e. Path to completion:* We plan to build the veto detector in late summer / early fall 2017, so that it is available for the dress rehearsal run.

## 5. Beam Monitor

*a. Purpose:* The beam monitor provides a high-precision particle time measurement and a flux determination of beam particles downstream of the target. For scattered particle events, it provides a determination of the time and particle type of randomly coincident unscattered particles, to monitor beam stability. The time of flight from the beam monitor determines particle type independently from the RF time, and also determines muon and pion momenta. For Moller / Bhabha scattering events that generate triggers, the beam monitor detects the forward-going, high-momentum electron / positron.

*b. Requirements:* The beam monitor comprises a central hodoscope similar to the beam hodoscope of Section III B 2 and an outer hodoscope similar to the scattered particle scintillators of Section IV B. In both cases the underlying technology and the requirements are the same; the detector geometry is different.

*c. Detector design:* The central hodoscope of the beam monitor comprises two offset planes of 16-paddles, each similar to the beam hodoscope shown in Fig. 11. We use BC-404 scintillator paddles with dimensions 30 cm long  $\times$  12 mm wide  $\times$  3 mm thick. The long length is intended to limit radiation damage to the SiPMs. We use three Hamamatsu S13360-3075PE SiPMs in series to read out each end of each paddle. The same readout electronics is used as for the beam hodoscope.

The outer hodoscope consists of 4 paddles identical in technology to the scattered particle scintillator paddles, but of dimensions 30 cm long  $\times$  6 cm wide  $\times$  6 cm thick. For these paddles we use constant-fraction discriminators to maintain good timing for randomly coincident beam particles, for which we will not have pulse size information and thus cannot do walk corrections.

*d. Current status:* Full-size prototype paddles for the central hodoscope have been constructed and will be tested in June 2017, to verify performance. We have successfully tested 12-mm wide prototypes previously, but only up to 16-cm long. All components needed to construct the detector itself are on hand, except for the detector frames. Prototype scintillator paddles similar to the outer hodoscope paddles, but 50 cm long, have excellent performance characteristics in extensive testing in PiM1. The shorter outer hodoscope paddles should have superior resolution and efficiency.



*e. Path to completion:* The first beam monitor central hodoscope plane will be completed in summer 2017 for use in the fall 2017 dress rehearsal run. The second central hodoscope plane and the outer hodoscope paddles will be completed in fall 2017.

## C. Target

### 1. Purpose

The MUSE experiment requires a liquid hydrogen target of very stable density, and sufficient cooling power to minimize uncertainty in target length. The target will also be used for tracking tests and background subtraction measurements, which require multiple targets in addition to the full liquid hydrogen cell.

### 2. Requirements

Although liquid hydrogen (LH<sub>2</sub>) targets have been fabricated and widely used at various laboratories, special precautions have to be taken for each individual target to ensure safe handling of hydrogen which is a flammable gas. The MUSE LH<sub>2</sub> cryotarget system is further complicated by the physics need for a target ladder that will allow the beam to strike either a LH<sub>2</sub> target, a dummy target for background study, a carbon target for detector alignment, or no target at all – an empty target position – and by the experimental requirement for large vacuum windows. The latter requirement arises from the very large solid angle subtended by the detectors. Thus, the MUSE cryotarget system requires appropriate engineering and safety considerations. An external company, Creare Inc.<sup>2</sup>, has been selected to design and potentially fabricate the system. Part of the design effort was to build and test prototypes of the most critical components, such as the target cells and the entrance and exit windows. We discuss here the major sub-systems of the cryotarget system, the engineering design, and safety measures and tests for safe operation of the target at PSI. An outline of the main physics requirements for the target can be found in table IX.

---

<sup>2</sup> Creare website: [www.creare.com](http://www.creare.com)

TABLE IX. Target system requirements.

Parameter	Performance Requirement	Achieved?
Liquid hydrogen	maintain liquid hydrogen-filled cell at $T \approx 19$ k and $P \geq 1$ atm	not attempted; moderate
Cool down time	$< 3$ days	not attempted; moderate
Beam entrance window	$> 6$ cm	not attempted; easy
Exit window(s) (One continuous or two symmetric on beam left and beam right)	$20^\circ < \theta < 100^\circ$ ; $\phi = 0^\circ \pm 45^\circ$ at $\theta = 60^\circ$ beam up-down and beam left-right symmetry	prototyping underway; challenging

### 3. Target Design: Major Sub-Systems

The MUSE target system consists of many sub-systems. One of them is the target ladder. It consists of two approximately 300 ml cylindrical cells (6 cm inner diameter (I.D.), 14 cm height including the end caps) mounted coaxially, one above the other, and a carbon target ( $6 \times 6$  cm<sup>2</sup> area). Each cell consists of a Kapton cylinder with a wall thickness of about 0.12 mm and two copper end caps. The pipes of the ladder are made of copper. The upper cell is filled with LH<sub>2</sub> and serves as the cryogenic target. It is operated at a temperature of 20 K and a pressure of 1 bar. The lower cell is empty and serves as the dummy target to measure the background. The carbon target is used for detector alignment.

A cryocooler is utilized to cool a copper condenser and the copper structure of the target ladder. The cryocooler is bolted to the condenser to ensure good thermal contact. The CH110LT single-stage cryocooler from Sumitomo Industries has been selected, partially because similar cryocoolers have been used at PSI and because they have a service center in Darmstadt, Germany. The total power load on the LH<sub>2</sub> target at 20 K is only a few  $\mu$ W from the beam and a few 100 mW (taking into consideration a few layers of aluminized Mylar superinsulation wrapped around the target) due to radiation. Thus, the CH110LT cryocooler, which has 25 W cooling power at 20 K and 50 Hz, has sufficient power to

liquefy hydrogen and maintain it at 20 K.

The target is controlled and monitored via a FPGA based PLC target control system. The target system has an external pressure sensor and heaters on the condenser to regulate the hydrogen pressure and thus the temperature of the LH<sub>2</sub> cell. Close to 20 K, a change of 0.1 K in LH<sub>2</sub> temperature results in a change of 24 Torr in pressure <sup>3</sup>. Hence, a more precise temperature regulation is achieved by having a feedback loop on hydrogen pressure instead of temperature. Additionally, temperature sensors are installed on the copper condenser to support a backup temperature regulation system. Each target cell has one temperature sensor, one level sensor, and two heaters, which are all monitored by the slow control system.

The target ladder and the condenser are housed inside a vacuum chamber to provide good thermal insulation. The outer diameter (O.D.) cannot exceed 49 cm so that it does not interfere with the rest of the experimental set up. The design is discussed in details in Section III C 4. The chamber has a bellows which allows the cryocooler, the condenser and the targets to move vertically together. The chamber requires two windows: a beam entrance window made of Kapton with approximately 7 cm I.D. and thickness less than 0.2 mm, and an exit window(s) for the beam and scattered particles, covering a  $\theta$  range of  $[20, 100]^\circ$  on each side of the beamline, and  $\phi$  range of  $[-45, 45]^\circ$  from the target center at  $\theta = 60^\circ$ . It is highly preferable to have a continuous window with a thickness of up to 285 g/m<sup>2</sup> covering  $\theta$  region of  $[0, 110]^\circ$  on both sides of the beamline, if possible. The window must be capable of withstanding the pressure difference between atmospheric pressure and vacuum. Each window assembly consists of a frame on which the window sheet is glued. The sheet seals onto the vacuum chamber with an O-ring.

Another important sub-system is the vacuum system. It is provided by PSI. It consists of mechanical and turbo pumps, valves and a PSI-built control system. The layout of the pumps and valves is shown in Figure 19. The fore-vacuum side of the turbo pump is connected to a scroll pump through a buffer to increase the lifetime of the scroll pump. The same mechanical pump is also used to pump out the supply line, the target cell and the cold trap for purging. The exhaust of the mechanical pump goes into a dedicated hydrogen exhaust pipe in the PiM1 area.

<sup>3</sup> See NIST website: [webbook.nist.gov/cgi/fluid.cgi?ID=C1333740&Action=Page](http://webbook.nist.gov/cgi/fluid.cgi?ID=C1333740&Action=Page)

A gas system is used to control hydrogen flow. Figure 19 shows the schematic layout of the gas system that is fabricated by PSI. Hydrogen gas for the target is supplied from a compressed hydrogen gas tank. The tank is placed outside the PiM1 experimental area (in an explosion-proof cabinet). Approximately 0.3 m<sup>3</sup> of H<sub>2</sub> gas is needed. Safe disposal of hydrogen gas leaving the target cell is achieved by the direct release of the hydrogen gas into a dedicated hydrogen exhaust pipe in the PiM1 area. The pneumatic and mechanical overpressure relief valves are configured such that the pressure in the LH<sub>2</sub> target, the hydrogen input and exhaust lines always remains below 2 bar.

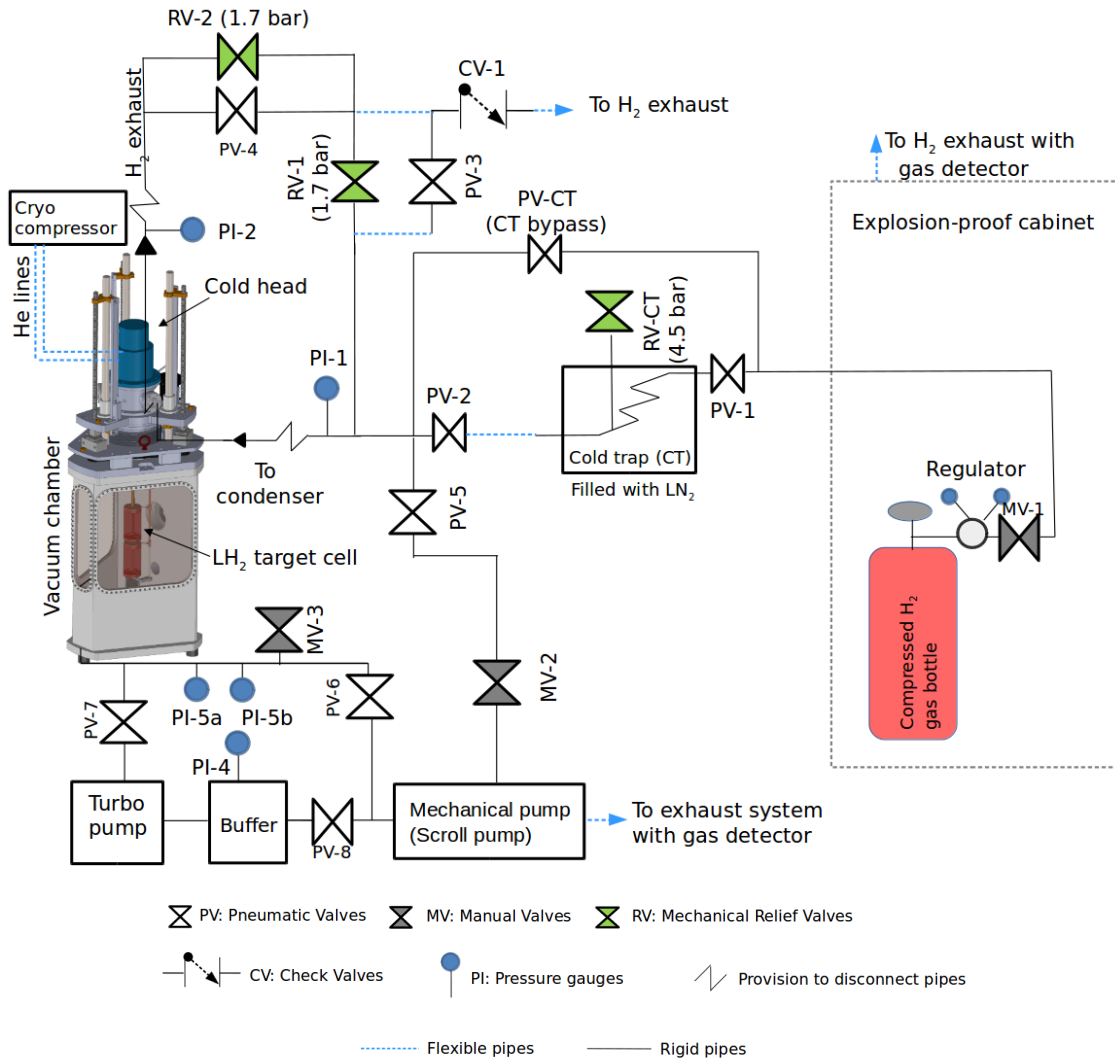


FIG. 19. The schematic layout of the gas system. Note that flexible pipes are required to allow vertical movement of the target ladder and the condenser.

#### 4. Target Design: Engineering Design by Creare

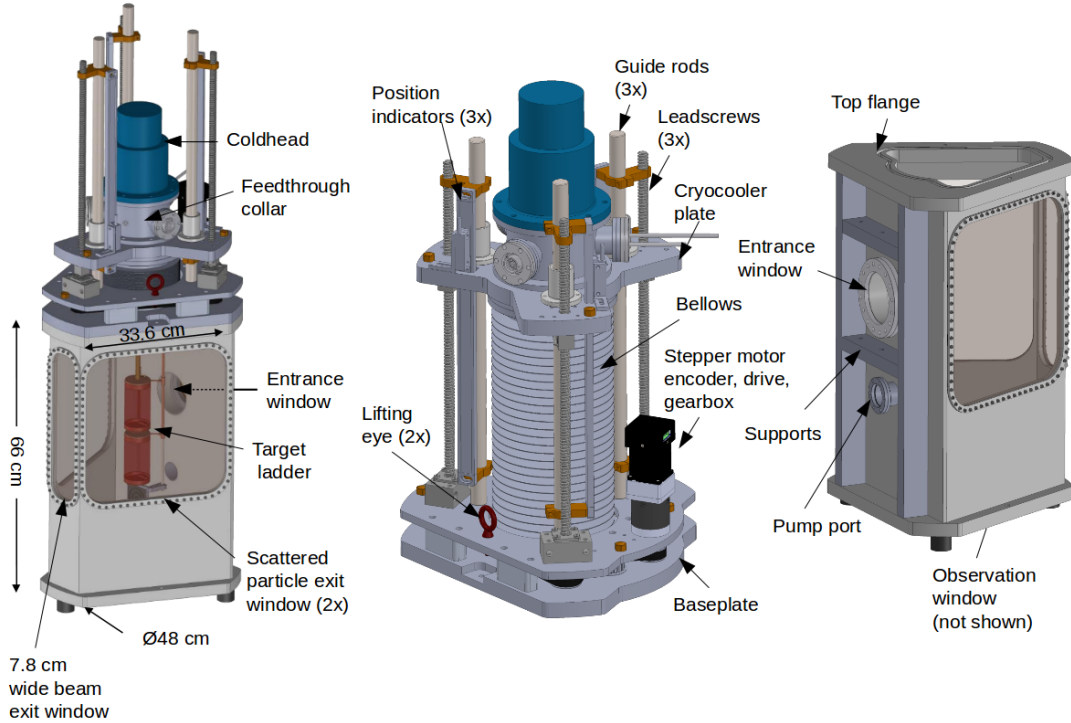


FIG. 20. The vacuum chamber design by Creare. (Left) A full view of the chamber with the lift system. (Center) The details of the lift system implemented on the top of the chamber. (Right) A back view of the chamber showing the chamber supports, entrance window and pump port.

A CAD rendering of the vacuum chamber with entrance and exit windows, bellows, cryocooler and target ladder is shown in Fig. 20. The chamber material is chosen to be stainless steel. The vacuum chamber has an O.D. that fits within 49 cm, and it has a height of 66 cm. This does not include the lift system. The chamber wall thickness was determined to be 9.5 mm, based on chamber stress analysis. This thickness provides a safety factor of at least a factor of two from the yield point.

A large edge-welded bellows allows the vertical movement of the cryocooler, the condenser and the target ladder. The bellows has an I.D. of 15.2 cm and is capable of providing the required vertical movement of 34 cm to attain all four target positions. Such bellows are commercially available. The vertical movement of the cryocooler plate (shown in Figure 20 (center)) and the target ladder is achieved by using three leadscrews which are

driven by a cogged timing belt and motor system. Three guide rods keep the cryocooler plate centered and prevent movement in the horizontal plane. As a precautionary measure, a magnetic position scale is attached to each guide rod to provide the true position of the cryocooler plate at three equally spaced radial positions.

Figure 20 also shows a feedthrough collar with three conflat flanges connected to the chamber top. Two of them serve as electrical and fluid feedthroughs while the third is a spare. The condenser has two copies of a heater circuit ( $25\ \Omega$ , 200 W each) and a Lakeshore Cernox temperature sensor, one for regular operation and the other as a backup. The target cell and the empty cell each have a  $50\ \Omega$ , 50 W heater for regular operation and a second as a backup, one Lakeshore Cernox temperature sensor and one Allen Bradley level sensor attached inside the top end cap. The electrical feedthrough has sufficient pins to accommodate all electrical connections and also provide spare pins.

The vacuum port is placed below the entrance window such that it lies above the detector support table. The bottom of the chamber has a view port where a camera can be attached to survey the X and Z coordinates of the target. The design has provisions for bolting the chamber to a stand which, in turn, can be bolted to the raised platform of the experimental hall, thus providing a very stable configuration. The stand has translation mechanisms to adjust the chamber position in all three directions. The height of the stand is chosen such that the adjustment screws lie above the detector support table.

The beam entrance window has a 7.5 cm O.D. clear aperture in accordance with the specified experimental requirements. Creare has successfully vacuum tested a  $50\ \mu\text{m}$  thick Kapton sheet for the entrance window using a test assembly fabricated from a 6 inch diameter conflat nipple. Pressure tests using the same configuration confirmed that the sheet can withstand a pressure difference of 4 bar, thus providing a safety factor of four with respect to operating conditions.

It is preferred that the exit window for the beam and the scattered particles is a single, continuous window covering the  $\theta$  region of  $[0, 110]^\circ$  on both sides of the beamline and the  $\phi$  region of  $[-45, 45]^\circ$  at  $\theta = 60^\circ$ . This requires a  $64.1 \times 33.7\ \text{cm}^2$  clear aperture. There are several other constraints imposed by the experimental requirements on the design. It should be homogeneous and there should be a minimum distance of 10 cm between the center of the target and the window along the beam direction to allow the

study of background and vertex reconstructions. It should be able to not only routinely operate under atmospheric pressure, but also have a pressure safety margin of 3 times the operating pressure. Furthermore, the window material should be chosen such that the angular resolution in the scattering angle,  $\Delta\theta$ , is 19 mrad or better for a precise determination of the proton's electric radius.

Building an exit window which satisfies all these constraints has proved to be very challenging. Several types of materials have been tested for the exit window. Among those were a 125  $\mu\text{m}$  thick Kapton (the thickest Kapton that is commercially available) and various sailcloth fabrics<sup>4</sup> which are Mylar laminated on Kevlar-like fabric. Due to the cylindrical shape and large size, all these windows deflect inside to varying degrees and form pleats when vacuum is established inside the chamber. Unfortunately, these pleats lead to inhomogeneities which are difficult to simulate and they lead to large multiple scattering for particles traversing through them.

We have settled on a trapezoidal design for the chamber which would use three separate, flat windows made of a 120  $\mu\text{m}$  thick Kapton and a sailcloth for the beam exit window and the two scattered particle windows, respectively. The use of three small-sized flat windows instead of one large-sized cylindrical window has eliminated the problem of pleats without violating the hard requirement of covering a  $\theta$  range of  $[20, 100]^\circ$  from the target center on both sides of the beamline. The analysis will be more complicated due to background events generated in the two support strips for the window frames at the very forward angles, which can generate additional event triggers. We are studying with Geant4 simulations the backgrounds, background rejection in the analysis, and the use of small veto scintillators just outside the two support strips to tag particles which scatter from these strips into the acceptance. Preliminary results are very positive.

Figure 21 shows a schematic view of the target ladder along with the dimensions of each cell. In this configuration, a single copper tube with 1 cm O.D. connects the inside of the condenser to the top end cap of the  $\text{LH}_2$  cell. It serves as the  $\text{LH}_2$  inlet tube as well as  $\text{H}_2$  exhaust outlet tube for the target cell. The bottom end cap of the target cell is connected only to the Kapton cylindrical wall of the cell. Laboratory tests performed

---

<sup>4</sup> These sailcloth fabrics were manufactured by Dimension-Polyant. Website: <http://www.dimension-polyant.com/>

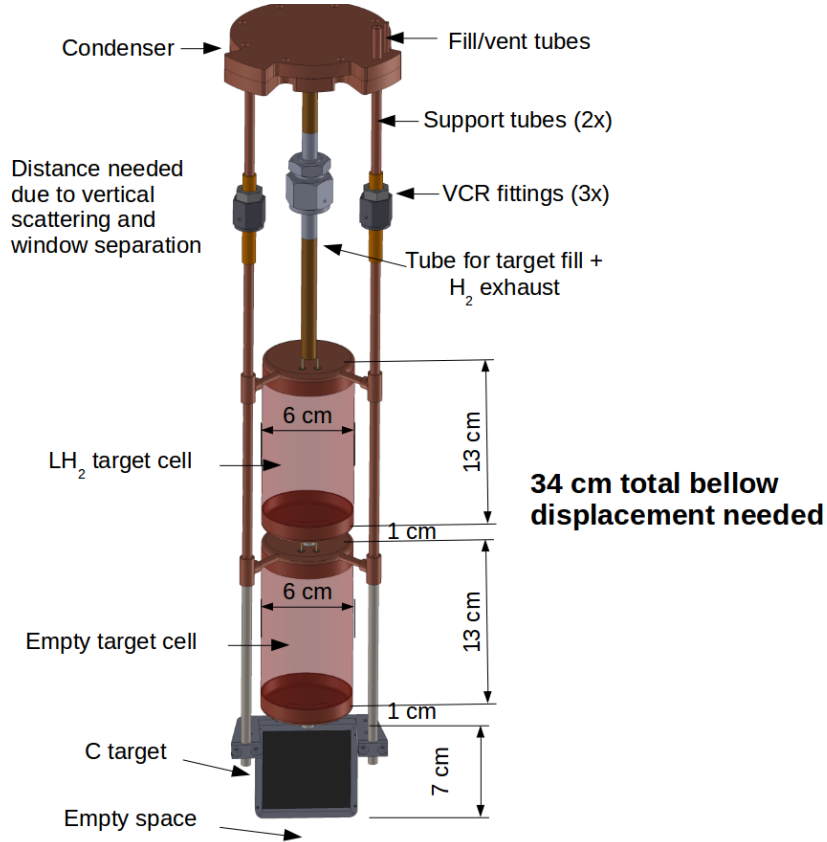


FIG. 21. A schematic view of the target ladder.

on target ladder prototypes at the University of Michigan (U-M) have shown that this configuration gives a higher safety factor for the LH<sub>2</sub> target cell than the configuration in which a LH<sub>2</sub> inlet tube is connected to the bottom end cap and a separate tube is connected to the top end cap to remove the hydrogen exhaust from the target cell. This may be because the latter configuration over-constrains the target's Kapton wall.

Two support tubes (0.63 cm O.D.) shown in Figure 21 connect the condenser to the three targets via radial stubs (0.32 cm O.D.). These support structures provide additional mechanical stability to the ladder. The condenser and the entire pipe structure, starting from the bottom of the condenser up to the top end cap of the empty target cell, are made of copper to establish thermal equilibrium between these components. The support tubes are placed to the sides and rear (upstream side) of the target ladder, away from the interaction area and in the shadow of the supporting chamber walls, avoiding additional



sources of background.

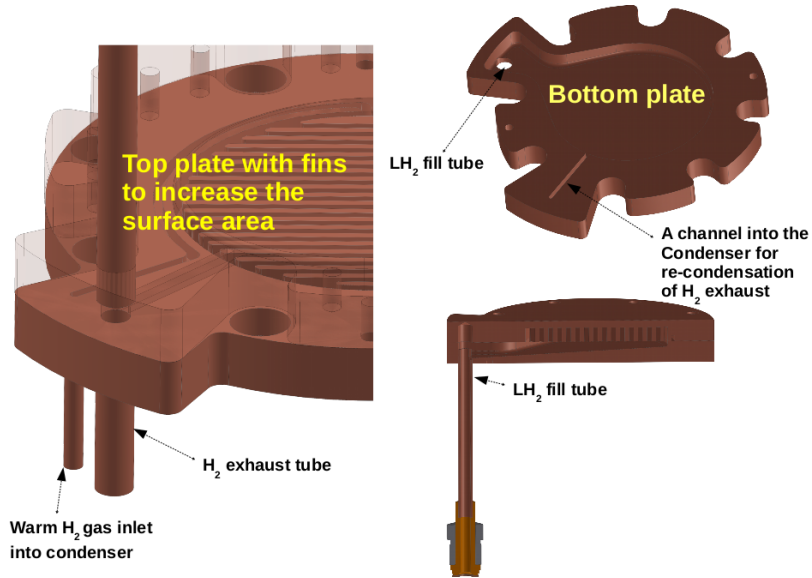


FIG. 22. SolidWorks drawings of the condenser.

Figure 22 shows SolidWorks drawings of the condenser. The top plate consists of a cavity which contains a series of fins to provide enough surface area for condensing hydrogen. The internal floor of the bottom plate is tilted towards the liquid hydrogen fill pipe that is connected to the target. A channel milled into the bottom plate allows the hydrogen exhaust from the target to re-enter the condenser and get liquefied. The condenser weighs 1.27 kg and has an internal condensing surface area of 350 cm<sup>2</sup>.

### 5. Target Design: Target Cell Design and Fabrication

Various target cells have been fabricated and tested at U-M to fine-tune the fabrication technique. These cells have cylindrical shapes with walls that are made with three wraps of a 25  $\mu\text{m}$  thick Kapton sheet (see Figure 23). The three wraps are glued together using Stycast 1266. The thickness of the glue is controlled to achieve a total thickness of about 0.12 mm for the cell wall. This method leads to a strong and robust wall. The height of the cell is consistent with the experimental requirement (11 cm without including the end caps). The Kapton cylinder has an extra 1 cm length at both ends to glue the end caps to

the cylinder. Cell tests were performed at a differential pressure of 2 bar at liquid nitrogen temperature over several temperature cycles. Destruction tests have consistently shown that the cells survive a differential pressures of 3.8 bar at about 300 K, thus providing a higher safety factor than the factor of three recommended by PSI.

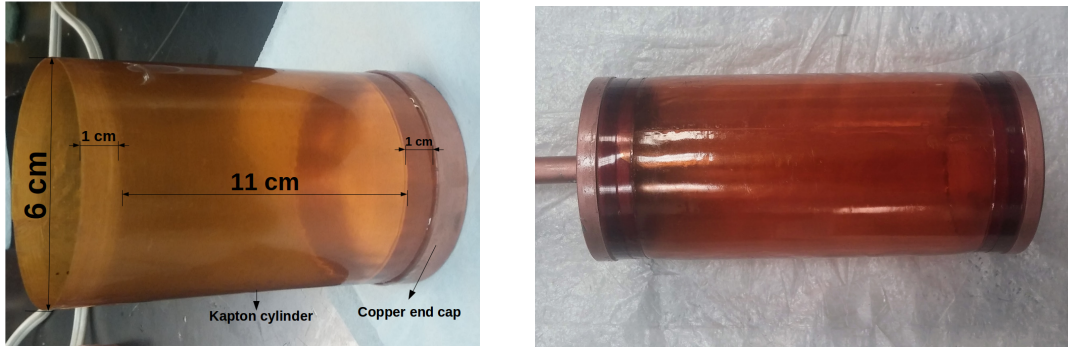


FIG. 23. Photographs of a target cell prototype built at U-M. (Left) The Kapton cylinder is made from three wraps of a  $25 \mu\text{m}$  thick Kapton sheet glued together using Stycast 1266. (Right) Two copper end caps are glued to the Kapton cylinder using Stycast 1266. The glue joints between the cylinder and the end caps are further reinforced by gluing few layers of Kapton strips.

#### 6. Target Design: Safety Measures and Tests

Full details for the safe operation of the cryotarget are provided in the MUSE Hydrogen Target Safety and Operating Procedures Report, which has to be approved by PSI before MUSE can operate the target in the PiM1 area. The main points are discussed here.

The pneumatic valves in the gas system controlled by the slow control system protect the target cell from high pressure. For additional safety, these valves are normally open-type valves. As backups, the mechanical over-pressure relief valves, operating independently of the slow control system, guarantee protection of the target from high pressure (i.e. above 1.7 bar). Furthermore, gas detectors and safety alarms are placed at various places to detect hydrogen leaks and issue warnings.

If there is a loss of power, valves to the vacuum pumps will close and thus maintain reasonable vacuum inside the chamber. Pneumatic valves in the inlet and exhaust lines will open.  $\text{LH}_2$  will slowly warm up and the evaporated  $\text{H}_2$  gas will be directed to a

dedicated H<sub>2</sub> exhaust pipe in the PiM1 area.

In case there is a slow loss of vacuum due to a leak, the valves to the pumps will close. The evaporation process will be slow and the evaporated H<sub>2</sub> will be directed to the dedicated H<sub>2</sub> exhaust pipe in the PiM1 area.

If there is a rapid loss of vacuum, such as from a window rupture, the shock wave may rupture the target cell. In that situation, hydrogen will mix with air and possibly lead to an explosion (if the mixture of H<sub>2</sub>:O<sub>2</sub> reaches a ratio of 10:1). Note that the target cell will evaporate only about 0.25 m<sup>3</sup> of H<sub>2</sub> into the area, which has the significantly greater volume of about 200 m<sup>3</sup>. Furthermore, the target will be wrapped in multilayer insulation, so the shock wave should be significantly mitigated. To protect the vacuum chamber windows, protective plastic shields are used to cover the windows whenever there is access to the area.

Lastly, one should consider the possibility of a target rupture. The released liquid will evaporate and expand quickly in the chamber. The outcome will depend on the extent of failure. If the target cell develops a slow leak, the windows will most likely remain intact and the evaporated hydrogen will be pumped out by the vacuum system into the H<sub>2</sub> exhaust system. On the other hand, if the target cell breaks releasing a large amount of LH<sub>2</sub> in a short period of time into the chamber, this may break the chamber window(s) and lead to an explosion as discussed above.

The cryotarget system will undergo multiple stages of safety tests before the production run begins in the summer of 2018. The overall procedure is as follows. The pipe work of the gas system will be thoroughly inspected for leaks. It will also be checked whether the pipes can successfully hold pressure up to the relief pressure of 1.7 bar. Prototypes of windows will be vacuum tested and pressure tested at 3 bar. Testing the target will involve multiple steps. First, it will be pressurized to 2 bar differential pressure using helium gas. At this pressure, the target will undergo several temperature cycles using liquid nitrogen and will be thoroughly checked for leaks after each cycle. Next, a cooldown test with neon, which has a similar boiling point to hydrogen but is not explosive, will be performed using the final cryotarget system in a staging area. The target will be pressure tested up to the set pressure of the mechanical relief valves. If successful, a cooldown test with a few milliliters of LH<sub>2</sub> will be performed in the staging area. Finally, a complete integration

test at the PiM1 beam line will be performed to fully test all components, including the slow control system and safety procedures before the production run begins.

#### *7. Current status and path to completion*

The target design process started in mid-December of 2016, and was essentially completed in June 2017, with: a successful completion of engineering design review of the chamber and target ladder by PSI; constructed cell prototypes meeting design requirements; a fully designed gas system; safety documentation under review; and tests of safety factors of the large exit windows well underway. We and Creare have both estimated that, given the current status and rate of progress, the complete target system can be ready for beam in summer 2018.

#### *8. Operation and Maintenance of the Target*

Once commissioning is completed and operations begin, target experts along with shift workers will be responsible for normal monitoring and operation of the target. The local PSI target group will assist as needed, such as for maintenance and/or repair work. To that effect, European standards are used to construct the system; all designs, off the shelf and manufactured components are metric as requested by the local group.

## **IV. SCATTERED PARTICLE SPECTROMETER**

### **A. Straw Chambers**

*a. Purpose:* The Straw Tube Tracker provides high resolution and high efficiency tracking of the scattered particles from the target.

*b. Requirements:* The design requirements are given in Table X. The MUSE straw tube tracker is based on recent developments in straw chamber design [15] being implemented for the PANDA experiment [16]; this design meets our requirements, but for a different geometry chamber in a different accelerator environment.

TABLE X. Straw Tube Tracker requirements

Parameter	Performance Requirement	Achieved
Position Resolution	150 $\mu\text{m}$	$\checkmark$ <120 $\mu\text{m}$
Efficiency	99.8% tracking	$\approx$ 99% in prototype; moderate
Positioning	$\approx$ 0.1 mm, 0.2 mr in $\theta$	not attempted; moderate
Positioning	$\approx$ 0.5 mr pitch, yaw, roll	not attempted; moderate
Positioning	50 $\mu\text{m}$ wire spacing	not attempted; moderate
Rate Capability	0.5 MHz	not attempted; easy

*c. Detector design:* The detector design is a combination of individual straw design, which is based on the PANDA straw chamber [15], with a geometry appropriate for the MUSE experiment.

The PANDA design uses thin-walled, over-pressured straws, allowing for significantly less straw material while providing mechanical stability. We adopt the same straws, wires, end pieces, and feed throughs from this design. The PANDA chambers have operated successfully at rates exceeding 8 kHz/cm, significantly higher than the MUSE rates. The PANDA chambers have also achieved a position resolution of  $\approx$ 150  $\mu\text{m}$ .

MUSE requires symmetric scattered particle detector systems to beam left and right. We use 2 chambers on each side of the beam, each chamber with 5 vertical planes and 5 horizontal planes, to achieve high tracking efficiency. In order to provide better resolution on the scattering angle, the vertical straw planes will be placed closer to the target. In order to break symmetries that make certain trajectories hard to track, the straws in the front and rear planes will be offset by  $\approx$ 2 mm from each other. Straw spacing is 1.01 cm, and adjacent offset straw planes are centered 0.87 cm apart.

Table XI summarizes chamber geometry and the number of straws per chamber. The spacing between the chambers will be about 6 cm from the back of one chamber to the front of the next chamber. The front chambers each have 275 60-cm long vertical straws and 300 55-cm long horizontal straws. The rear chambers each have 400 90-cm long vertical straws and 450 80-cm long horizontal straws. The total number of straws in the system is 2850. No stereo planes are needed because the low beam flux reduces the likelihood of multiple particle tracks on the same side of the beam, and the scattered particle scintillators provide

a precise time and approximate position for any second tracks.

TABLE XI. Straw chamber parameters including the distance from the pivot, chamber active area, and the number of straws.

Chamber	Distance (cm)	Active Area (cm <sup>2</sup> )	Number of Straws per Chamber
Front	30	60 × 55	575
Back	45	90 × 80	850

The chambers will be operated using a mixture of 90% Ar + 10% CO<sub>2</sub> at a pressure of 2 bar, using pressure-control transducers and mass flow controllers (Bronkhorst Ltd.). Each of the 4 chambers will be provided with an independent gas supply system. The gas mixture will run in continuous-flow mode, completely replacing the full gas load in the chambers every 12 hours, which will allow us to run without bubblers.

The straws operate at 1700V. Voltage is applied and readout connected using dedicated HV / readout cards, into which the PADIWA frontend cards plug directly (see Section VB). The PADIWAs are in turn read out by TRB3 TDCs.

The full design for the chamber frames, including the straws, gas lines, and readout electronics, has been realized in CAD format, to ensure compatibility with other MUSE systems at the design level. Figure 24 shows the CAD drawing.

*d. Current status:* Figure 25 shows a prototype half-chamber, constructed at Hebrew University, and partially operated at PSI in in December 2016. In these test beam conditions the straws were shown to operate reliably with approximately 90% efficiency, which yields 99% tracking efficiency for 5 planes. Fig. 26 shows a typical 'shark fin' diagram of the straw time distribution, above a flat, random noise background.

Importantly, during the same beam test, tracking information was obtained from a half chamber (vertical straws only) and a tracking algorithm was implemented. Figure 27 shows a track obtained from the tracking code. A preliminary analysis of the chamber resolution using a small calibration dataset shows a resolution of approximately 115 μm; Fig. 28 shows the residuals of the track distances. It is clear that the design resolution can be achieved.

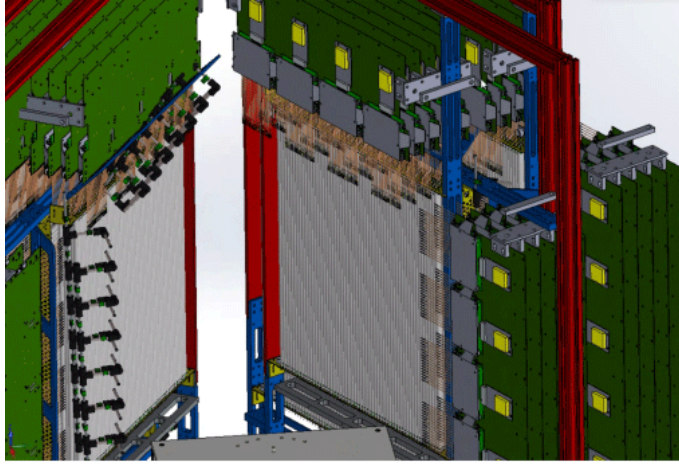


FIG. 24. Snapshot of CAD drawing of the four STT chambers mounted on the table. Straws (light gray), HV/readout cards (dark gray) with PADIWAs (yellow on gray), frames (blue and red), and parts of the gas system plumbing (black) and other components can be seen.

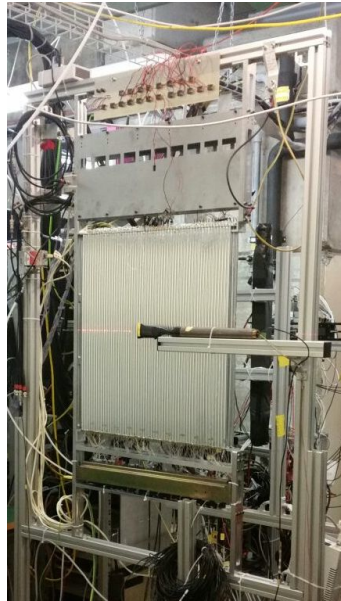


FIG. 25. A prototype half-chamber mounted at PSI.

*e. Path to completion:* In order to avoid straw damage during transport to PSI, the construction plan has individual straws being built at Hebrew University and shipped to PSI, where the chambers will be assembled and tested. The first chamber straws are at PSI, being assembled into a chamber. The chambers are assembled by gluing the individual straws together using a precision machined jig. The straw packages are mounted between

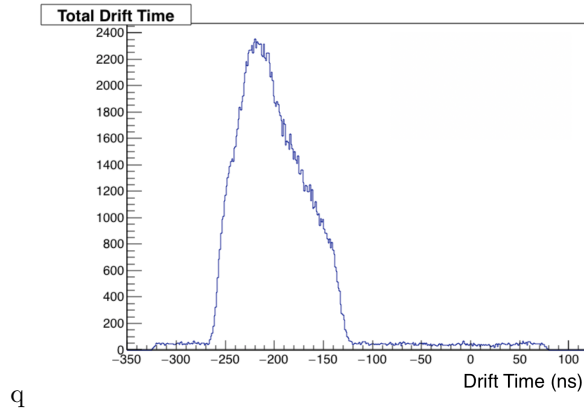


FIG. 26. A typical drift time histogram from the chamber tested during the Dec 2016 test period, showing the expected 'shark fin' shape.

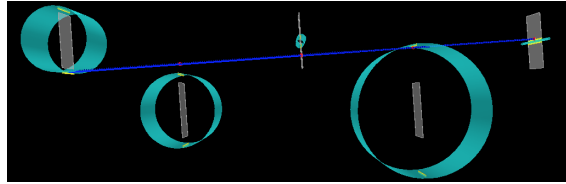


FIG. 27. A track generated by the track fitting code used for the straw tube tracker.

printed circuit board end plates, which are mounted into the detector frames. Gas, HV, and readout are then added.

Straw construction will continue at the Hebrew University with the second chamber straws shipped to PSI for the December 2017 beam time, and the straws for the final chambers being shipped in early 2018.

New HV / readout cards are being built, incorporating a gain modification to improve the signal to noise ratio. This will be tested during the June 2017 beam time.

The assembled chambers are flushed, and the wire positions determined using a well-collimated radioactive source and trigger scintillator, moved by a precision stepper motor across the chamber. The drift time measurements allow the wire to be located. This technique has previously been used with precision  $\approx 50 \mu\text{m}$ . The first chamber will be scanned with this technique in August 2017.



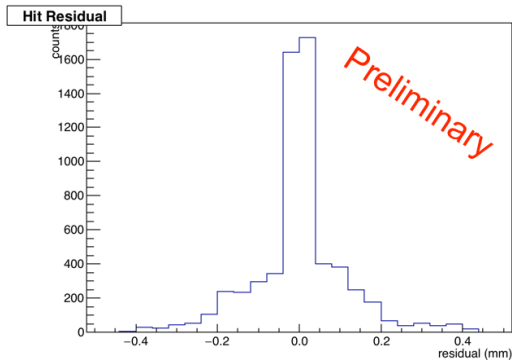


FIG. 28. A plot of the track residuals from a genfit analysis of beam test data.

TABLE XII. Scattered-particle scintillation-detector requirements

Parameter	Performance Requirement	Achieved
Time Resolution	$\approx 60$ ps / plane	✓ 55 ps
Efficiency	99%, $\ll$ 1% paddle to paddle uncertainty	✓ 99%, paddle to paddle not attempted, moderate
Positioning	$\approx 1$ mm, $\approx 1$ mr	not attempted; easy
Rate Capability	0.5 MHz / paddle	✓ 1 MHz

## B. Scattered-Particle Scintillators

*a. Purpose:* The scattered-particle scintillators are part of the event trigger and help with the particle separation via time-of-flight (TOF) measurements.

*b. Requirements:* This purpose requires high detection efficiency for the particles of interest and excellent timing resolution. The requirements for the scattered-particle scintillators are laid out in Table XII.

*c. Detector design:* The Experimental Nuclear Physics Group at USC is building the scattered-particle scintillators for the MUSE experiment.

The group previously designed, prototyped, and built the new FToF12 detector for the upgraded CLAS12 at Jefferson Lab. The design and construction procedures of the MUSE detectors follow that of the FToF12 detector. The detector will be made of Eljen Technology EJ-204 plastic scintillators, which have a high light output and fast rise time. Each end of the long scintillator bars is fitted with black tape, which masks the corners

while leaving a circular window that extends one millimeter into the area that will be covered by the photocathode. The corner blocking reduces the amount of reflected light contributing to the leading edge of the PMT signal. Hamamatsu R13435 PMTs are then glued to each end of the scintillator. The bare counter is wrapped with precision-cut aluminized mylar and DuPont<sup>TM</sup> Tedlar. The Tedlar film extends beyond each PMT onto the anode, dynode, and high-voltage cables, providing a single light-tight casing for the entire counter. Pairs of scintillator bars are mounted on aluminum sheets that serve as backing structure. These units will be mounted in a frame. Details about the construction process and system tests for quality assurance can be found in Ref. [17].

Table XIII lists the design parameters for the scintillator walls. The front wall is approximately square and covers at least a horizontal angular range from 20° to 100° from all points within the target. The back wall has an increased angular acceptance to account for particles which scatter in the front wall material.

TABLE XIII. Design parameters for the scintillator walls.

	Front wall	Back wall
Number of scintillator bars	18	28
Scintillator cross section	6 cm × 3 cm	6 cm × 6 cm
Scintillator length	120 cm	220 cm
Target to front-face distance	52 cm	74 cm
Gap between scintillator bars	0.3 mm	0.3 mm
Scintillation material	EJ-204	EJ-204
Photomultiplier	Hamamatsu R13435	Hamamatsu R13435

*d. Current status:* We are presently building the 18 short and 28 long detectors for the left TOF wall. All photomultiplier tubes have been tested and characterized; almost all photomultiplier tubes have been glued to the scintillation bars; most detectors are built. We continue to measure position-dependent time resolutions in cosmic-ray tests before we mount pairs of detectors on their backing structure. Average time resolutions of  $\sigma_{avg} = 55$  ps for the 220-cm long bars and below 50 ps for the 110-cm long bars were obtained; see Fig. 29.

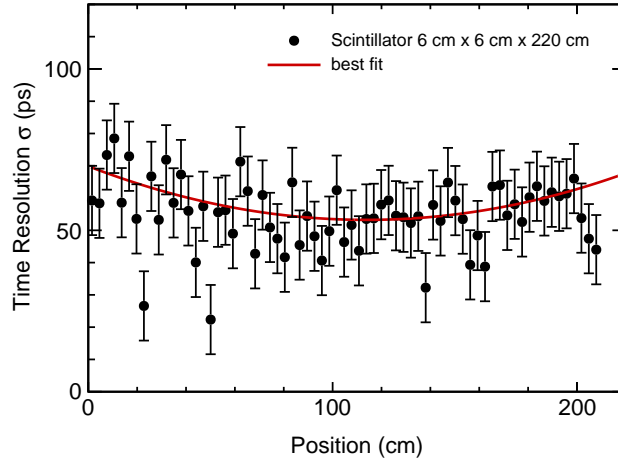


FIG. 29. Position-dependent time resolution for a prototype MUSE 220-cm long scintillation bar after calibration, event selection, and time-walk correction. The average time resolution is  $\sigma_{avg} = 55$  ps.

We have studied the performance of the proposed scattered-particle scintillators with Geant4 simulations of the planned setup. The particle interactions and their energy deposition within the scintillators have been calculated. Figure 30 shows the distribution of deposited energy in a  $5 \text{ cm} \times 5 \text{ cm}$  scintillator which was used in the summer 2013 test measurement at  $\pi\text{M1}$ . The incident particles were  $153 \text{ MeV}/c$  muons. The simulated energy distribution agrees nicely with the measured data. The energy deposited by particles whose paths do not traverse at least the full thickness of the scintillator is lower than the energy of the lower edge of the Landau-like portion of the energy distribution.

Simulated energy distributions for the  $6 \text{ cm} \times 3 \text{ cm}$  and  $6 \text{ cm} \times 6 \text{ cm}$  scintillator bars are shown in Fig. 31 for scattered electrons (left panel) and muons (right panel) at various beam momenta. The set of curves with low energy deposition (red) is for the front wall; the set of curves with high energy deposition (blue) is for the thicker back wall. In the studied range, the energy depositions for  $e^\pm$  are independent of the beam momentum. The simulation shows for each event the maximum energy deposition in any front- or back-wall bar. Very nearly all events have energy depositions above threshold,  $E_{th} = 2 \text{ MeV}$ , in (at least) one bar. The detection efficiency is indeed very high.

A detailed view of the particle detection efficiencies for the scattered-particle scintillator

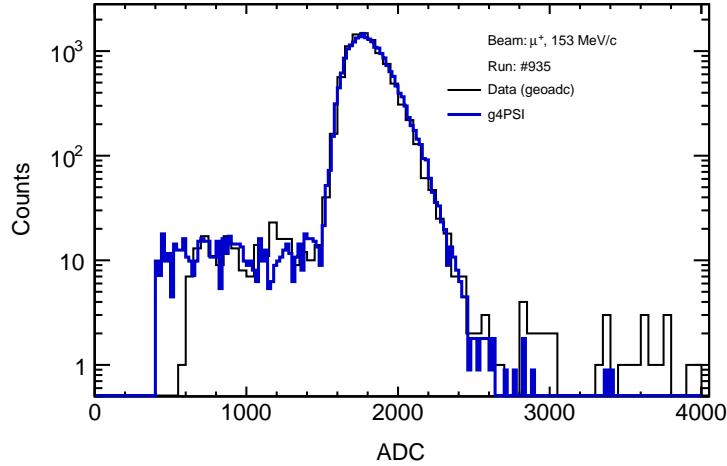


FIG. 30. Deposited energy of muons passing through a  $5 \text{ cm} \times 5 \text{ cm}$  scintillator bar. The data are from the summer 2013 test measurement at  $\pi M1$ . The blue histogram shows the result of the Geant4 simulation.

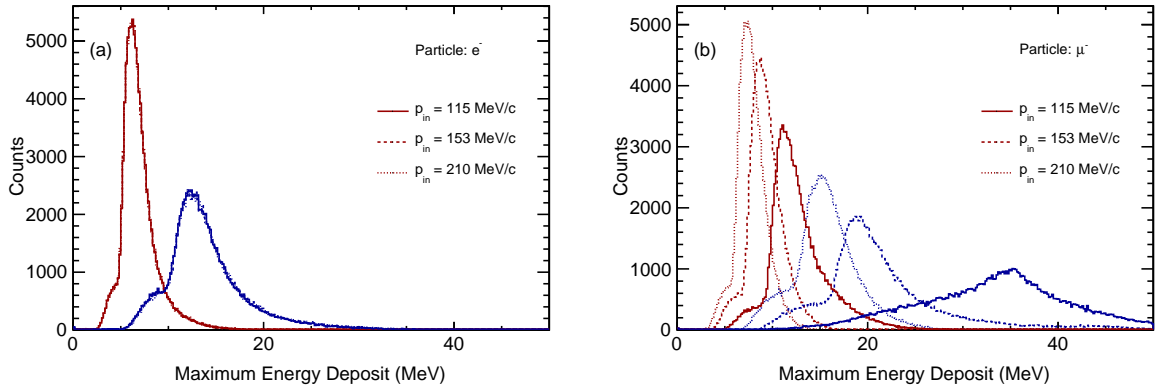


FIG. 31. Simulated energy deposition for scattered electrons (left) and muons (right), traversing the  $6 \text{ cm} \times 3 \text{ cm}$  bars of the front and  $6 \text{ cm} \times 6 \text{ cm}$  bars of the back scattered-particle scintillator wall. The simulation recorded for each event the maximum energy deposition in a scintillator of a given plane.

walls at  $115 \text{ MeV}/c$  is shown in Fig. 32 for electrons and positrons as a function of the particle scattering angle. All panels are for the same detection threshold of  $E_{th} = 2 \text{ MeV}$ . The solid dots give the ratio of events with an above-threshold hit in the front plane per incident particle. Particles were incident on the “active” area of the scintillator plane; the physical size of the plane is slightly larger. The average acceptance is higher for higher

momenta and it is higher for  $\mu^\pm$  than for  $e^-$ . The one-plane efficiency is practically

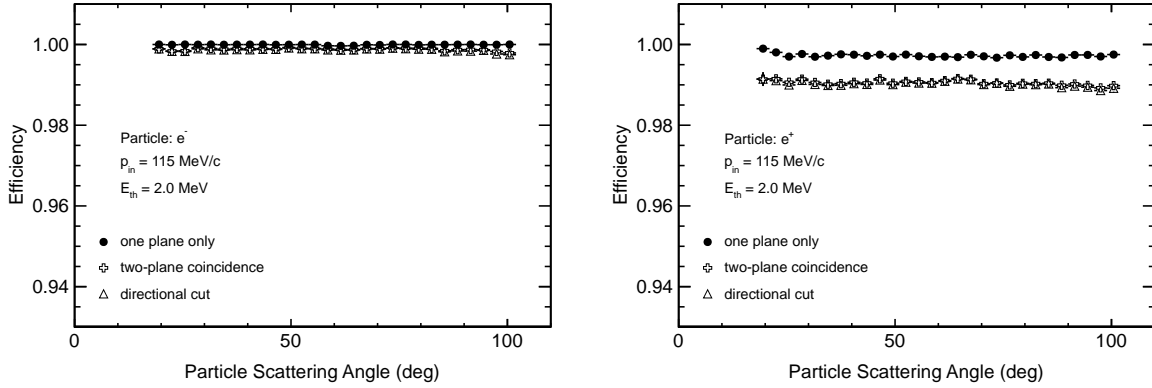


FIG. 32. Estimated detection efficiency as a function of particle scattering angle for  $e^+$  and  $e^-$  at beam momenta of 115 MeV/c. The change of momentum of the scattered particle with scattering angle is taken into account.

100%. The two-plane coincidence (plus symbol in Fig. 32) requires above-threshold hits in both the front and back planes. It is in all cases well above 99.5%, except for  $e^+$ . The “directional cut” (triangle points in Fig. 32) utilizes the fact that scattered particles, which originate in the target, deposit energy mostly in certain combinations of front- and back-wall scintillators. For an event to pass this cut, each hit in a scintillator bar of the back wall must coincide with hits in up to three corresponding neighboring scintillators in the front wall. This directional cut does not affect the efficiency much but helps to suppress triggers from background events which do not originate within the target. Figure 33 illustrates this correlation of scintillator-bar numbers for muons with different momenta originating in the target volume.

If uncorrected, detection inefficiencies in the scattered-particle detector will lead to errors in the measured cross sections. The average corrections for detector inefficiencies are of the order of 0.1% for  $\mu^\pm$  and  $e^-$ ; and 0.4% to 0.9% for  $e^+$ . These values require a threshold of  $E_{th} = 2$  MeV. The positron efficiency is reduced due to possible annihilation processes. The detector inefficiencies show some angular dependence at low scattered particle momentum (backward angles at 115 MeV/c beam momentum); see Fig. 32. After correction for these effects, we expect the contribution from the scattered-particle detector to the systematic uncertainties of the absolute cross section to be less than 0.1%. The

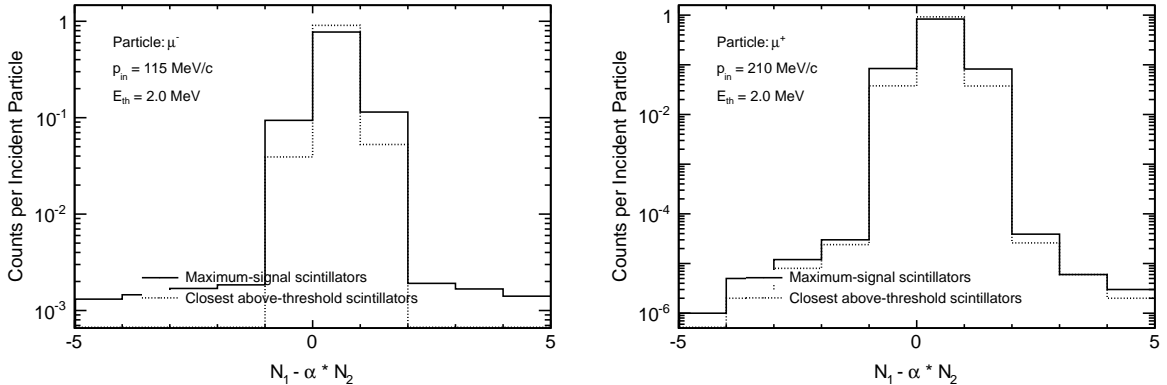


FIG. 33. Typical paddle-number correlations between paddle numbers  $N_1$  and  $N_2$  from the front- and back-wall scintillators, respectively. The factor  $\alpha$  is the ratio of the distances from the target to the front and back scintillator-wall mid-planes, respectively.

uncertainty is larger for  $e^\pm$  cross sections if the threshold can not be kept stable. Because of their very similar detector response, we expect the contributions to the systematic uncertainties of relative cross sections for  $\mu^+$  and  $\mu^-$  to be negligible. Also, the  $\mu^\pm$  and  $e^-$  relative cross section uncertainties should be much smaller than 0.1%.

*e. Path to completion:* The larger part of the detectors for the left wall have been built and we expect to complete its construction on schedule by the end of summer 2017. Thereafter, as soon as the remaining construction funding becomes available, we will continue building detectors for the right wall.

## V. DAQ

### A. Electronics and Readout

*a. Purpose:* The Data Acquisition System (DAQ) reads out the fast event data from the detectors, times and pulse sizes, for event analysis and detector calibration. This sub-system also reads out slow controls, and includes the event trigger.

*b. Requirements:* The requirements for the DAQ hardware are listed in table XIV. The readout channels necessary for the experiment are listed in table XV, except that we treat the GEM DAQ as part of the GEM system, discussed in Section III B 3.

TABLE XIV. Data acquisition system hardware requirements.

Parameter	Performance Requirement	Achieved?
TDC Resolution	$\leq 40$ ps	$\checkmark < 30$ ps
QDC Resolution	$> 10$ bit	$\checkmark 12$ bit
Readout Rate	100 $\mu$ s per event	400 $\mu$ s per event to date, moderate

TABLE XV. Summary of detector needs. The Gate Source is either “Exp’t” for the full experiment trigger, which requires delaying signals, or “Fast” for an earlier Level 1 trigger.

Detector	No. Chan’s	TDC	Disc.	QDC	Gate Source	Trigger Input
Upstream Beam Line Detectors:						
SiPM Hodo.	64-128	$\checkmark$	MCFD	$\checkmark$	Fast	$\checkmark$
Veto	8	$\checkmark$	PADIWA	$\checkmark$	Exp’t	$\checkmark$
Beam Monitor:						
SiPM	64	$\checkmark$	MCFD	$\checkmark$	Fast	$\checkmark$
Paddles	8	$\checkmark$	MCFD	$\checkmark$	Fast	$\checkmark$
Scattered Particle Detectors:						
STT	2850	$\checkmark$	PADIWA	$\times$	N/A	$\times$
SPS	184	$\checkmark$	PADIWA	$\checkmark$	Exp’t	$\checkmark$

*c. Data acquisition system design* The basic components of the MUSE DAQ are outlined in the following paragraphs.

The analog detector signals are digitized by discriminators of two kinds: PADIWA level discriminators, or Mesytec MCFDs.

**PADIWAs** were custom-designed at GSI to provide a fast, compact and cost-effective readout for FAIR experiments. They are 16-channel level discriminators. The customized MUSE PADIWA design removes the standard  $\times 10$  input amplification. PADIWAs have an independent threshold for each channel, set via TRB3 board control lines, using either a script or the TRB3 web interface. The PADIWAs send LVDS signals to the TRB3 TDC. Tests have shown that for fast scintillators, level discriminators used in combination with QDC-signals for time-walk corrections provide better time resolution than constant fraction discriminators.

**Mesytec MCFDs** provide constant fraction discrimination for all detectors read out by SiPMs, and for the beam monitor paddles where we will want to precisely time random coincidence signals with no corresponding pulse size measurement. The MUSE MCFDs have been customized with LVDS outputs for direct input to the TRB3 system, instead of externally converting the standard ECL output. Each board discriminates 16 channels, and provides two outputs per channel: a copy of the analog signal for input to the QDC, and the discriminated logic pulse. The MCFD board also provides a single 16OR LEMO output, which can be used as a fast gate of the MQDC-32. MCFDs are controlled via usb interface.

**TRB3** boards were designed by GSI as a customizable, programable, scalable, versatile building block for modern data acquisition systems. Each TRB3 has a central FPGA for control, communication, and triggering, plus four peripheral FPGAs programmed as high-resolution – 11 ps – TDCs plus scalers. Each peripheral FPGA controls and reads out three PADIWAs or 48 channels. Thus, one TRB3 can control and read out a maximum of 12 PADIWAs or 192 channels. The TRB3s are powered by a 48 V supply, and are independently controlled and read out over gigabit ethernet. They require no VME crate. The TRB3s will be distributed throughout the experimental equipment, leading to shorter cabling and better timing.

**Mesytec-MQDC-32s** provide signal size information, for pulse-height corrections to improve timing, and for monitoring detector response, to check for gain shifts. The MQDC-32 accepts both positive and negative inputs in the same hardware module, through the use of jumpers, and reads out all channels in 250 ns. The MQDC-32s can be gated with a fast trigger or with the experimental trigger. For the fast trigger, a final read-out trigger or fast clear needs to then be provided by the experiment trigger. This eliminates the need for long delay cables. The MQDC-32 modules are housed in VME crates.

VME infrastructure is provided via standard VME crates, read out via a **CAEN v2718 VME-PCI bridge** in each crate over a **CAEN A3818C - PCIe 4-link optical bridge**. In order to synchronize the data provided by each of the crates and that provided by each TRB3, an event number, generated in the TRB3 triggering system, is fed into the VME systems using a **VULOM 4b** board, designed and produced by GSI. This VME board has an FPGA, and a series of inputs and outputs which will received the trigger



number, and other trigger header information. This information will be copied into the VME buffer and sent with the data to ensure synchronization between systems.

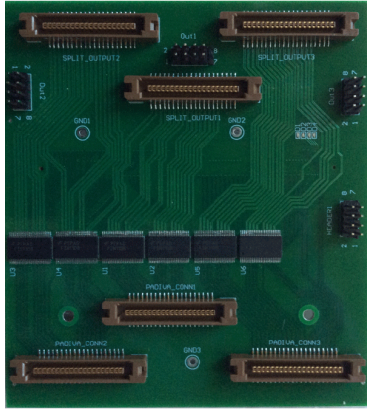


FIG. 34. A prototype splitter board. The board mounts directly onto the TRB3 peripheral FPGA, in place of the usual board used to couple in TDC input signals.

**A custom splitter** copies logic signals going to the TRB3 TDCs for use in trigger logic and QDC gating. The prototype splitter board shown in Fig. 34 was built by Marcin Kajetanowicz, who works with the group of Piotr Salabura of Jagiellonian University of Krakow, Poland. It directly couples the logic signals from trigger detectors into the high precision TDC FPGAs, and copies the signal to a second trigger FPGA. Test data show that timing resolution of the directly coupled signal is basically unaffected, while the copied signal timing has a total jitter increased by  $\approx 10$  ps – see Fig. 35 – which is negligible at the trigger level.

For diagrams of the systems planned for each detector read out, see Appendix C.

*d. Current status:* All major DAQ components have been designed, prototyped and investigated during beam tests, all components function as required. The modified PADIWA design to date has only been tested by modifying standard PADIWAs, as we await delivery of the modified design. Also, two simple circuit boards to adjust cable form factors are being designed and built by Basel. One plugs into the Mesytec 34-pin output and converts to a TRB3 cable form factor for TRB3 input. The second takes scintillator signal coax cable inputs to a pin connector on which a PADIWA mounts.

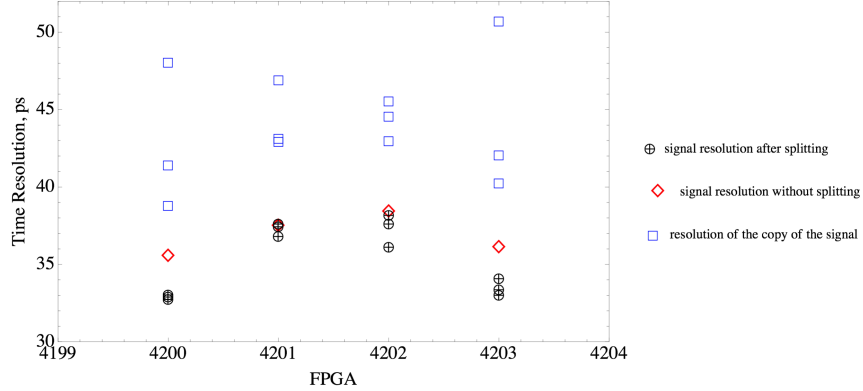


FIG. 35. Measured TRB3 timing resolution for signals in  $\pi$ M1 without and with the prototype splitter board.

One specification still to be met is the readout time, which is currently limited by the GEM readout, discussed elsewhere.

POs have been issued for nearly all procurement of DAQ components needed in 2017. Many cable components have been ordered, but final cable procurement and construction awaits final cryotarget design, review, and acceptance, to ensure procurement of the appropriate cable lengths.

*e. Path to completion:* The remaining electronics will be purchased as soon as the second year of MUSE funding is approved. All electronics systems will then be assembled, with the cable construction and testing, at PSI, in time to allow all electronics systems to be fully tested before needed for data taking.

## B. Trigger

*a. Purpose:* The trigger identifies events of interest for the fast DAQ, and initiates the read out of detector signal times and sizes.

*b. Requirements:* The trigger needs to efficiently identify muon and electron scattering events, suppress pion scattering events, and provide multiple potentially prescaled trigger types corresponding to the different types of physics and / or background events of interest. The trigger needs to be  $\approx 99\%$  efficient at identifying  $e$  and  $\mu$  scattering events to maintain statistical precision and  $\approx 99\%$  efficient at identifying and not triggering from pion induced background events to keep dead time low. Trigger angle-dependent efficiency variation should be small and known at the  $\approx 0.1\%$  level. Finally, the trigger must be generated within several hundred ns of the event.

*c. Trigger system design* We use a two level trigger consisting of several level 1 trigger components feeding into a level 2 master trigger. The components include the following:

- *The beam PID system* uses RF timing of signals from the beam hodoscope described in Section III B 2 to identify  $e$ 's,  $\mu$ 's, and  $\pi$ 's.
- *The veto system* detects particles that will enter the vacuum chamber through the veto scintillators and the thick metal vacuum chamber wall behind them. These particles arise from the beam tails, from particle decays, or from scattering in the beam line detectors.
- *The scattered particle system* uses hit patterns in the scattered particle scintillators to identify possible scattering events from the cryotarget region.
- *The beam monitor system* identifies forward-going particles after the target. Due to the potential of this information to change the shape of the angular distribution, this system is not planned to be used in production data taking. It is intended for calibration data such as trigger verification, beam momentum measurements, and determination of backgrounds in the scattered particle detectors when they do not have a level 1 trigger.
- *The random system* generates a random in time (with respect to beam interactions) signal to help measure unbiased detector backgrounds.
- *The NIM system* generates a trigger independently via NIM logic modules. We have used NIM trigger generation in test times to date, and the NIM system will continue to be used as the FPGA trigger is developed, as an aid to its verification.

- *The level 2 master trigger* takes the outputs of the aforementioned level 1 systems to determine if any trigger conditions are satisfied. It includes different prescale factors for the different trigger types and a latch function.

Typically the various detector logic signals are sent to a high precision TDC on a TRB3 FPGA through a splitter board, with the copied signal sent to a second TRB3 FPGA programmed with the appropriate trigger logic.

The beam PID system logic uses individual channel logic signals plus the RF signal as a clock to determine the RF phase of each logic signal. All 32 signals from each beam hodoscope plane are fed into the beam PID system; each plane is analyzed in a separate FPGA. The different particle types arrive in the beam line detectors about every 20 ns, with  $\approx 3 - 6$  ns separation between particle types and  $\approx 0.3$  ns rms width of the particle bunches in time. We require both ends of a paddle to fire to identify particle type, to suppress noise. The system can identify multiple particle types at the “same” time from the 16 paddles in a plane.

The veto system is a simple logical OR of all 8 PMTs in the veto detector.

The scattered particle system uses logical ORs and ANDs to identify hit patterns of scintillator paddles correlated between the front and rear walls. Due to the number of channels, the system is divided among four FPGAs, for top left, lower left, top right, and lower right PMTs. Each FPGA has inputs from 18 front + 28 read PMTs.

The beam monitor system comprises three FPGAs, using ORs and ANDs to analyze that both ends of one of the 16 hodoscope paddles fire in either the front or rear hodoscope planes, or that both ends of one of the 4 large flanking paddles fire.

The random system will be a logic signal generated from noise in a PMT away from the beam line. The rate will be kept low by setting an appropriate discriminator threshold.

The level 2 master trigger then generates triggers, including the following<sup>5</sup>:

- *Scattered electron*: Beam PID system indicates  $e$ ,  $!\mu$ ,  $!\pi$ ; !VETO; Scattered particle system indicates  $\text{TOPLEFT} \vee \text{TOPRIGHT} \vee \text{BOTTOMLEFT} \vee \text{BOTTOMRIGHT}$ ; beam monitor ignored, random ignored, NIM ignored.

---

<sup>5</sup> We indicate a logical NOT with the symbol “!” and a logical OR with the symbol “ $\vee$ ”.

- *Scattered muon*: Beam PID system indicates  $\mu$ ,  $!e$ ,  $!\pi$ ; !VETO; Scattered particle system indicates TOPLEFT  $\vee$  TOPRIGHT  $\vee$  BOTTOMLEFT  $\vee$  BOTTOMRIGHT; beam monitor ignored, random ignored, NIM ignored.
- *Scattered pion*: Beam PID system indicates  $\pi$ ,  $!e$ ,  $!\mu$ ; !VETO; Scattered particle system indicates TOPLEFT  $\vee$  TOPRIGHT  $\vee$  BOTTOMLEFT  $\vee$  BOTTOMRIGHT; beam monitor ignored, random ignored, NIM ignored.
- *VETO*: Beam PID system ignored; VETO; Scattered particle system ignored; beam monitor ignored, random ignored, NIM ignored.
- *Beam particle*: Beam PID system indicates  $e \vee \mu \vee \pi$ ; !VETO; Scattered particle system ignored; beam monitor TRUE, random ignored, NIM ignored.
- *Random*: Beam PID system ignored; VETO ignored; Scattered particle system ignored; beam monitor ignored, random TRUE, NIM ignored.
- *NIM*: Beam PID system ignored; VETO ignored; Scattered particle system ignored; beam monitor ignored, random ignored, NIM TRUE.

*d. Trigger system current status* Trigger programming has been ongoing and all needed functions of the trigger have been demonstrated in prototypes.

To test the veto, scattered particle, and beam monitor systems, we programmed initially OR and AND logic for testing. Different operations were encoded for different input channels to test the various options needed. The code generated logic pulses of widths 20, 30, and 40 ns from the inputs, and performed the same logic on all pulse widths. This is a standard technique to provide information about trigger efficiency when signal times or widths can vary, and we plan to use this technique during the experiment. We found that the TRB3 FPGA generates these logic outputs within  $\approx 40$  ns.

A much harder task is the TDC function, using the RF clock to determine particle identification. The TDC was encoded with similar, but lower resolution, techniques to the TRB3 high precision TDC code, to speed up processing. This still requires detailed placement of the logic gates and logic routing through the FPGA. We coded for 48 input

channels, with the beam RF time divided into 32 0.6-ns wide TDC bins.<sup>6</sup> By varying the phase of the input signal relative to the clock, we determined that the bins width variation is sufficiently small, with bin widths ranging from about 0.3 - 1.0 ns. The phase determined is compared to separate  $e$ ,  $\mu$ , and  $\pi$  arrays to determine the particle type - this allows a single particle in a detector to be identified as multiple types in that detector, if the two types are close enough in time. We found that the TRB3 FPGA generates these TDC outputs within  $\approx 80$  ns.

*e. Path to completion* The TDC trigger code will be beam tested in the June 2017 beam time. Two main types of work remain to develop the trigger. The first, more straightforward, development is to adjust the generic code we have developed to the specific input logic combinations needed for the various level 1 triggers and the level 2 trigger. The second, less straightforward, development is to understand the TRBnet code implemented in the fast TDCs, and include it in our FPGA codes. Implementing TRBnet will allow monitoring and controlling - for example, adjusting the TDC bins that correspond to each particle type - the level 1 triggers through the network, rather than through the JTAG connectors on the boards.

### C. Software Systems

MUSE has been using and will continue to use the PSI MIDAS system for data acquisition. MIDAS supports the slow controls and standard data acquisition modules, and we have extended it to successfully read out all electronics used in the experiment: the GEM electronics, the TRB3s, and the Mesytec QDCs. The read out system has been incrementally extended as we have obtained additional modules and crates to read out, with ongoing performance tests. MIDAS has been operated at rates up to 2.4 kHz, with the limit determined by the number (0, 1, or 2) of GEM telescopes we read out, since the GEMs have been the slowest component, requiring nearly (1 ms / GEM telescope) in our original implementation. Block readout times for other electronics are  $\approx 0.1$  ms, but were not implemented in the original rate tests.

---

<sup>6</sup> With 0.6-ns wide bins and measured beam and detector time resolutions, particle identification gates in the trigger can be set on the RF time that are  $\approx 99.99\%$  efficient for both accepting electrons and muons and rejecting pions. Actual performance will depend on the bin widths in the time region between the peaks.

The DESY OLYMPUS analysis framework has been adopted into the experiment as “MUSECOOKER,” for data analysis. The analysis also uses CERN ROOT and GENFIT, a general wire chamber tracking program.

With a  $\approx 2$  kHz trigger rate, data rates are about 12 MB/s, with nearly all of the raw data coming from the GEMs. We have about 30 TB of local storage for experimental data, sufficient for about 1 month of full rate raw data, along with 90 TB of long term archival storage being arranged through PSI. We plan to reduce long term storage needs by zero-suppressing the GEM data, rather than retaining the full set of ADC values for each GEM plane.

## VI. TESTS, COMMISSIONING, CALIBRATIONS, RUNS

### A. Installation and Commissioning

The MUSE equipment is currently planned to be partially installed in late 2017 for a dress rehearsal run at the end of the year, with full installation completed in winter/spring 2018 for production data taking starting mid 2018. The 2017 dress rehearsal run will include most of the beam line detectors and one spectrometer arm. The beam line detectors for 2017 will be the first 2 of the 4 beam hodoscope planes, the GEM telescope, the veto detector, and the central hodoscope of the beam monitor. Also, only a solid target will be used in 2017.

Installation and commissioning of the detectors will follow typical procedures. Detector installation first requires assembly and installation of the corresponding support structures, the beam line detector table, the scattered particle frames, and the beam monitor frame. Also, the appropriate electronics, high and low voltage supplies, and gas systems must be available. From late summer to early fall 2017 we expect to install and survey the beam line hodoscope planes, GEM chambers, and veto detector on the beam line detector table, the left front STT on the beam line detector table, the left scintillators walls onto their support frame, and the central beam monitor hodoscope onto its frame.

Approximate operating conditions are known for all of these detectors from previous experience, including prototyping and testing after construction. Initial detector checkout

/ commissioning will be done with cosmic rays and sources, and ultimately with beam. Techniques are standard.

## B. Calibrations

MUSE requires several nonstandard calibration procedures, which we address here.

A special mount has been built that allows the GEM telescope to be tilted at various precisely known angles relative to the beam. We can use these data sets provide a check of the consistency of the internal GEM coordinate system, since the beam is not moving.

The STT wire spacing is determined with a precision moving collimated source in a special calibration setup. Also, to limit experimental systematic uncertainties, we require knowledge of measured scattering angle offsets at the sub-mr level. The experimental table is designed so that the STT can be rotated into the beam behind the GEMs, into several precisely determined angle settings. These measurements allow the STT wire spacing, position, and orientation to be checked, and also determine the STT orientation relative to the beam in the data taking setting. This can be achieved since the GEMs determine angles to  $\approx 1$  mr ( $100\mu$  spatial resolution over 16.8 cm) the STTs determine angles to  $\approx 5$  mr ( $150\mu$  spatial resolution over 4 cm) for one STT or  $\approx 1$  mr for the STT pair, and multiple scattering can be limited to 2-3 mr at higher channel momenta for alignment determination.

The GEMs and STT combined can be used to obtain data for multiple scattering from target and detector elements to verify simulations. We leave the STT in the beam line and use a beam trigger, but we add various materials between the GEMs and the STT. Note that the GEM telescope + STT setup verifies calculated multiple scattering in the GEMs, and the GEM telescope with 2 STTs verifies multiple scattering in the STTs. Of course, each of the measurements convolutes resolutions and multiple scattering.

The level 1 beam PID trigger needs to be calibrated for each momentum. If system electronics and cables and the accelerator setup are kept constant, the electron RF time is constant, whereas the pion and muon times vary with momentum. The beam PID will be calibrated with a beam trigger at a low beam flux of a several kHz, where the accidental rate is negligible. Once the trigger PID cuts are determined, the trigger will



be operated with increasing beam flux, up to the planned 3.3 MHz flux, to verify that its efficiency for accepting events of interest and for rejecting background events, as well as the effects of accidentals, are understood. Note that the scattered particle trigger requires additional study. The timing of the scattered particle trigger needs to be determined, and the prescale factors for the various trigger types need to be adjusted to optimize in particular the muon scattering uncertainties.

The table and beam monitor support are designed so that the beam hodoscope and beam monitor positions along the beam line can be varied by precisely known distances. Multiple measurements at different positions allows the muon and pion momenta to be determined.<sup>7</sup> We also use the downstream beam line to analyze the relative momentum of beam particles, by turning off the quadrupoles after the second dipole, and comparing positions of pions, muons, and electrons at the target. This measurement is performed for multiple positions of a narrow collimator at the channel intermediate focus, where the beam dispersion is 7 cm / %. TURTLE calculations indicate that the dispersion at the target is about the same, providing a  $\approx 10^{-4}$  measurement of the relative momentum.<sup>8</sup> The same measurement also gives information on energy loss in materials placed at the IFP, for validating simulations.

### C. Dress Rehearsal Run Plan

After the commissioning and calibrations are completed, the dress rehearsal run can start. The aim of a dress rehearsal run is to take a  $\approx 10\%$  sample of the intended full data set in near production data conditions, to be subjected to analysis so that any issues can be identified and corrected before starting the production data taking.

The dress rehearsal and production data taking run plan for an individual beam momentum are similar. In production data taking we will:

1. Determine the beam momentum.
2. Calibrate the trigger and determine its performance. Optimize prescale factors for different trigger types.

---

<sup>7</sup> We have obtained 0.2% – 0.3% measurements with 50-cm distance changes in PiM1. We have designed for 2-m changes in the experiment.

<sup>8</sup> This technique is being tested in the June 2017 test run.

3. Take data in the no-target setting to measure pion and muon decay and other backgrounds.
4. Take data with solid calibration target to verify position reconstruction.
5. Cycle through full hydrogen cell + empty cell settings to determine signal + backgrounds and backgrounds.
6. Repeat for opposite polarity.

The cryotarget will not be ready in time for the dress rehearsal run, so for #5 we will instead measure with solid CH<sub>2</sub> and carbon targets.

#### D. Run Plan

Based on estimated beam fluxes, cross sections, and efficiencies, the experiment requires 12 months of primary production beam time for a  $5\sigma$  measurement of whether the proton radius is the smaller muonic hydrogen or larger electron value. To date we have assumed an even distribution of 2 months beam time for each of the 6 momentum / beam polarity combinations. We have not tried to optimize this division since the optimization depends in part on actual system performance and in part on physics motivation. Also, the systematic and statistical uncertainties are roughly matched, reducing the effects of redistributing time. Since the muon scattering rates are higher for positive charge than negative, but lower in each case than the electron scattering rates, the division of time between the beam charges can improve the statistical uncertainties for the radius extraction by spending more time at positive polarity, or can improve the statistics for the two-photon measurement by spending more time at negative polarity.

Figure 52 in appendix A shows that the ratio of hydrogen elastic scattering to carbon elastic scattering ranges from a factor of 3 - 4 at small angles to an order of magnitude or more at large angles. Muon decay backgrounds are smaller than elastic scattering by an order of magnitude or more, once timing cuts are applied to the data. For each kinematic setting the time needs to be split between measuring the signal plus backgrounds with target full, and measuring the backgrounds with target empty. Figure 36 shows that

the final statistical uncertainty on the background subtracted cross sections is not very sensitive to the division of time between the two measurements. In our case it appears the signal to background varies with angle from about 3 - 10, and choosing to spend about 75% of the time on signal plus background will not cause the background subtracted statistical uncertainty at any angle to be more than a few percent worse than it would be if the division of time were optimized for that angle. Since changing between full and empty targets takes only a few minutes, we expect to cycle from target full to empty and back every several hours.

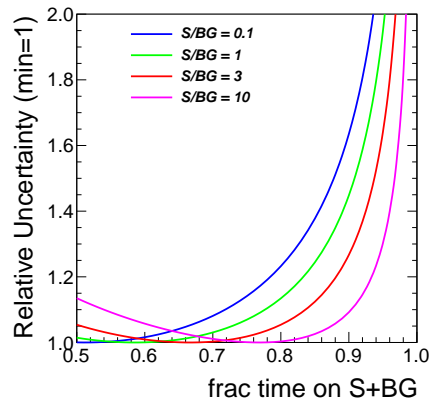


FIG. 36. The relative statistical uncertainty for the background subtracted cross section as a function of the fraction of time spent measuring the signal + background - the remaining fraction of time would be spent measuring the background.

To avoid being affected by long term issues, and as a check of stability, it is desirable to regularly change between momentum settings. However, changing momenta runs into two potential issues. First, momentum settings may not be reproducible with sufficient accuracy. We have established that if we cycle the channel, setting the channel momentum to at least 300 MeV/c until the Hall probe stabilizes before reducing the momentum to the desired value, then the RF time distribution and apparently the beam spot are reproduced, but we have not proven this with sufficient precision to consider it routine; we also have not tested this for channel polarity changes. Second, we plan to optimize the data by adjusting the number of beam hodoscope planes from 2 at 115 MeV/c to 3 at 153 MeV/c to 4 at 210 MeV/c. This requires working on the detector, near the cryotarget, to remove

or reinstall beam hodoscope planes. We prefer to avoid this activity due to the potential safety hazard of working near the cryotarget and due to a desire to minimize handling the detector, with the consequent risk of damage to some equipment. We cannot commit to more frequent momentum changes until we have more confidence in the procedure.

Once calibrations are finished and normal production operations are established, we expect up to a few target changes daily and momentum / polarity much less frequently.

We are considering two further checks on systematics, and our ability to extract the same form factors from different settings, beyond the three primary momentum settings, two identical spectrometers, and two beam polarities. We can obtain data with the straw tube trackers slightly rotated in angle, rather than symmetric, and run some time at a beam momentum off by a few MeV/ $c$  from one of our 3 planned settings. Each of these would require about half of the time of one of the already planned settings.

The detectors are built to have high efficiency, and are monitored through redundant planes, scaler rates, efficiency triggers, pulse size spectra, and slow controls. We expect to not need special efficiency calibration runs, after the initial setup. We also note that random coincidence beam particles provide an unbiased measurement of beam parameters and beam line detector performance and stability.

### **E. Personnel for Production Runs**

For MUSE production running, we plan to run single person shifts. We plan to have 3 - 4 experts – MUSE postdocs and Ph.D. students – on site during production data taking, to act as experts on call or in case a second person is needed for beam area access. The experts also need to be at PSI for additional time for checkout of the apparatus before production data taking starts. This plan leads to about 1400 expert and 1200 non-expert shifts for the two years of production data. Table XVI shows the shift commitments of core MUSE institutions involved in the construction project that were presented to the PSI BV48 meeting in February 2017. We are slightly under-committed for non-expert shifts, but strongly over-committed for expert shifts.

TABLE XVI. MUSE shift commitments.

Institution	Expert shifts	non-expert shifts
GW	360	168
Hampton	120	56
Hebrew	180	90
Michigan	308	96
Montgomery	0	112
Rutgers	720	112
South Carolina	120	196
Tel Aviv	0	196
Temple	360	90
TOTAL	2168	1116

## VII. ANALYSIS, CORRECTIONS, SYSTEMATICS, RESULTS

### A. Data Analysis

#### 1. Determination of Yields

Here we present various standard steps in the data analysis leading to the determination of yields. The event-data analysis inputs are QDC and TDC signals from the detectors along with trigger information.

- QDC spectra will be monitored to check for stability of detector gains, threshold setting, and consistency with simulations.
- Timing of fast scintillators will be improved with QDC walk corrections. All paddles (except veto paddles) have double-ended readout, so mean times will be determined.
- A raw time of flight is calculated from the beam hodoscope to the scattered particle scintillators. We average over multiple detector planes.
- GEM hit positions are determined from GEM clusters.
- Straw drift times are converted to drift distances.

- We use GENFIT for both GEMs and straws to determine tracks and residuals / resolutions. Tracking also determines efficiencies, independently from hit spectra.
- The GEM track is compared to the beam hodoscope hit position for consistency. We use the GEM track projected to the target to put a fiducial cut on the target to decrease the number of background, side-wall events.
- The straw track is compared to the scintillator paddle hit for consistency.
- The GEM and straw tracks together determine an interaction vertex, the quality of the reconstructed vertex, and the scattering and azimuthal angles. Simulations indicate few mm position resolutions, growing to the cm level for  $z$  position in cases of forward angle scattering, and typically 10 – 15 mr angle resolution, due to multiple scattering. We use a loose  $z_{target}$  cut as we prefer to remove background through full cell / dummy cell subtractions. See Fig. 37.
- GEM and straw tracks determine a path length between the beam hodoscope and scattered particle scintillators, leading to a corrected time of flight and  $\beta$ .
- The RF time and the corrected time of flight or  $\beta$  determine the reaction type, scattering or decay of some particle. We have also found in Monte Carlo studies that a neural network analysis approach, discussed below, is very efficient.
- Fiducial cuts are applied to the straw chambers, so that we do not use particles near the edge of the acceptance to determine cross sections.
- The data will be analyzed for accidental coincidences with other beam particles. Additional beam particles that might interfere with an unambiguous analysis will cause the event to be thrown out. Clearly additional beam particles provide unbiased measurements of beam properties (trajectories in the target, and perhaps momentum from time of flight from beam hodoscope to beam monitor).

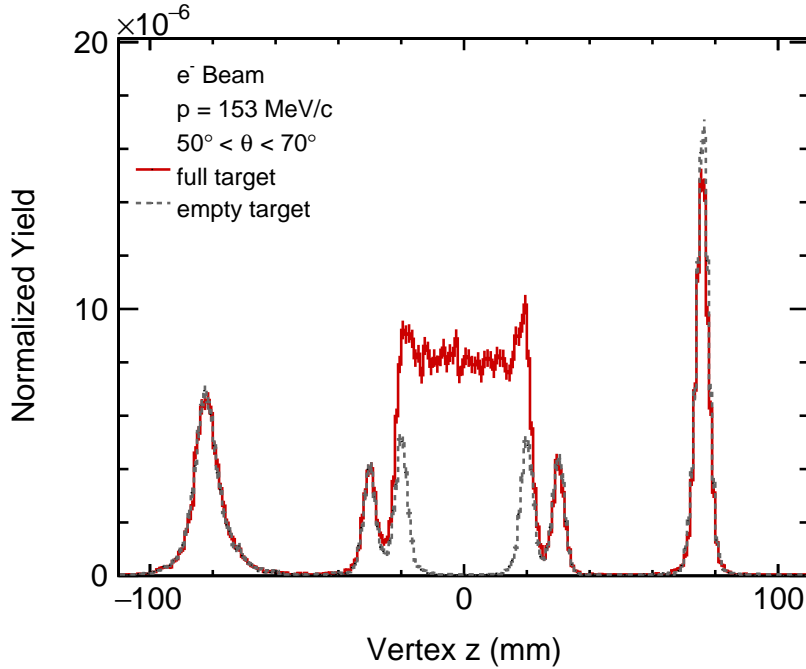


FIG. 37. Geant4 simulation of reconstructed interaction position along the beam line for electrons, with a full target (solid) and an empty target (dotted). The resolution along the beam line is a few mm; see also Fig. 38. The structures in the empty-target distribution are (from the outside to the inside): scattering-chamber windows, super insulation, and target entrance/exit walls.

## 2. Backgrounds

All reactions other than elastic scattering of electrons and muons from protons are background reactions. There is only a small probability that beam particles scatter or decay upstream and produce hits in the scattered particle detectors without giving hits in the beam line detectors – which would lead to throwing out the event due to multiple beam particles. As a result, we only consider reactions possibly leading to triggers that might be mistaken for electron or muon elastic scattering.

Pion events are removed by RF time in the beam line detectors. These events would also have a long corrected time of flight / small  $\beta$ . We do not consider them further.

Figure 37 shows a Geant4 simulated reconstructed image of the target along the beam line. The simulation included effects of the various detector and target materials on the particles. The resolution of the vertex  $z$  coordinate varies as a function of angle due

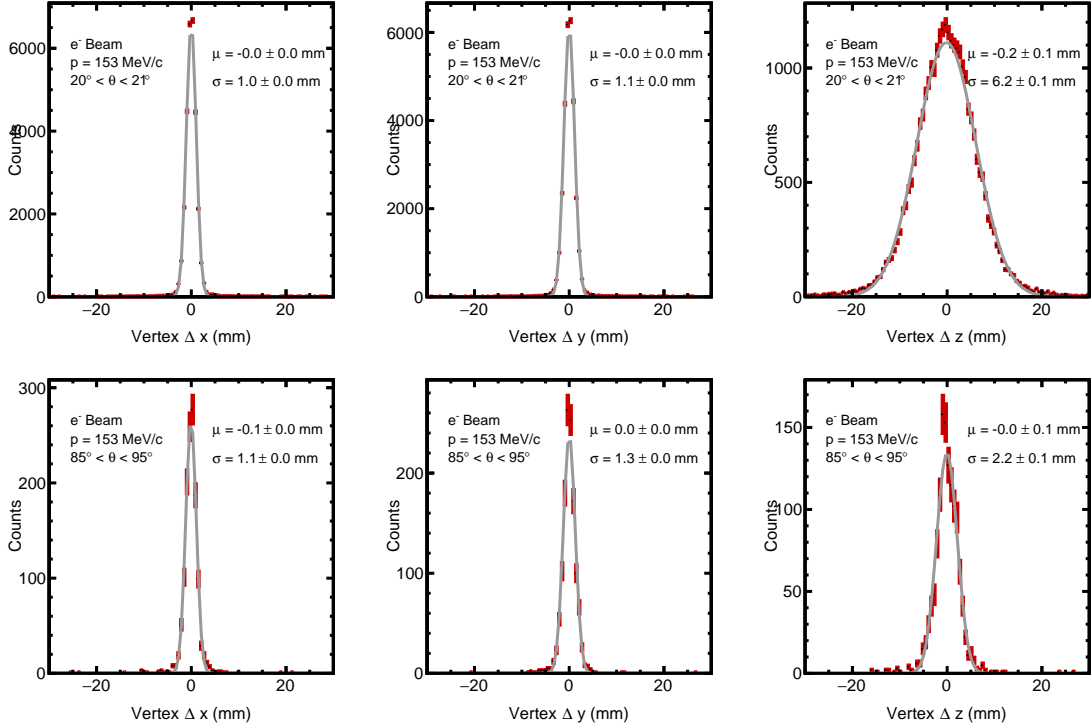


FIG. 38. Examples of differences between reconstructed and actual scattering reaction vertex from simulations for electrons at forward angles (upper panels) and perpendicular to the beam line (lower panels) and a beam momentum of 153 MeV/c.

to a  $1/\sin\theta$  geometric effect. The reaction vertex is determined by the position of the closest approach between the incident-particle track measured by the GEM chambers and the scattered-particle track measured by the straw chambers. The good reconstruction with few mm resolution is evident, which allows rejection of all events that do not result from scattering or decay in the immediate vicinity of the target cell; see also Fig. 38. We use the reconstructed vertex information to remove scattering backgrounds from vacuum chamber windows, which are far from the target. Scattering from the target cell walls must be subtracted. Monte Carlo simulations show that LH<sub>2</sub> cell - empty cell subtractions work well, but care must be taken for the downstream windows, due to the slight loss of flux, energy, and change in beam position distribution caused by interactions in the liquid hydrogen.

The shape of the target leads to an increasing ratio of wall events to liquid hydrogen events for trajectories further from the beam axis. We apply target fiducial cuts using the



GEM detector tracks to reduce scattering from the sides of the target cell.

Møller and Bhabha scattering generate a low-energy forward-angle background. The recoil electrons with enough energy (10 – 20 MeV) to trigger our system all go to smaller angles than the detectors, but can multiple scatter out into the detectors and generate events that look like forward angle scattering,  $<25^\circ$ . The beam monitor is an efficient veto detector for these Møller scattering background events in the offline analysis, as they have a forward going “high” momentum beam particle that continues into the high-precision beam scintillators after the target.

Muon decay with the electron or positron detected has similar kinematics to muon scattering, but a faster outgoing particle. We have studied the muon-decay-in-flight background with a trained neural network based on data from our Geant4 simulation of the full detector setup. The data included five parameters: time-of-flight (SiPM to front TOF SC wall and SiPM to rear TOF SC wall) information, energy deposition (in front- and rear SC bars), and front-to-rear SC bar correlations. We assumed overall 100 ps, 92 ps, and 89 ps timing resolutions for the system at 115, 153, and 210 MeV/ $c$ , respectively, as we plan to use more beam hodoscope planes at the higher momenta. Results for the muon scattering signal and for the muon-decay background for these observables are shown in Fig. 39 for a beam momentum of 153 MeV/ $c$ . Particularly the simultaneous use of time-of-flight information from both scintillator planes proved crucial for a good discrimination of the muon-scattering signal from the decay background. Results for 115 and 210 MeV/ $c$  momenta have also been obtained, but are not shown here in detail.

The output of the trained neural network for an event is related to the probability of the event being signal or background. Depending on the cut on the output variable larger and larger fractions of signal events can be selected at the expense of also accepting larger fractions of background events. This is shown in Fig. 40. As expected, the separation of peak and background events is much better at the lower 115 MeV/ $c$  beam momentum and worse for 210 MeV/ $c$ . We estimate that a close to 100% signal efficiency can be obtained with less than 0.1% background for the 115 MeV/ $c$  setting and less than 0.5% background for the 153 MeV/ $c$  settings. The time-of-flight distributions and pulse-height distributions of the simulation can be carefully validated in these settings. For the 210 MeV/ $c$  setting we estimate that an acceptance of 98% of the signal would include 1% of the background

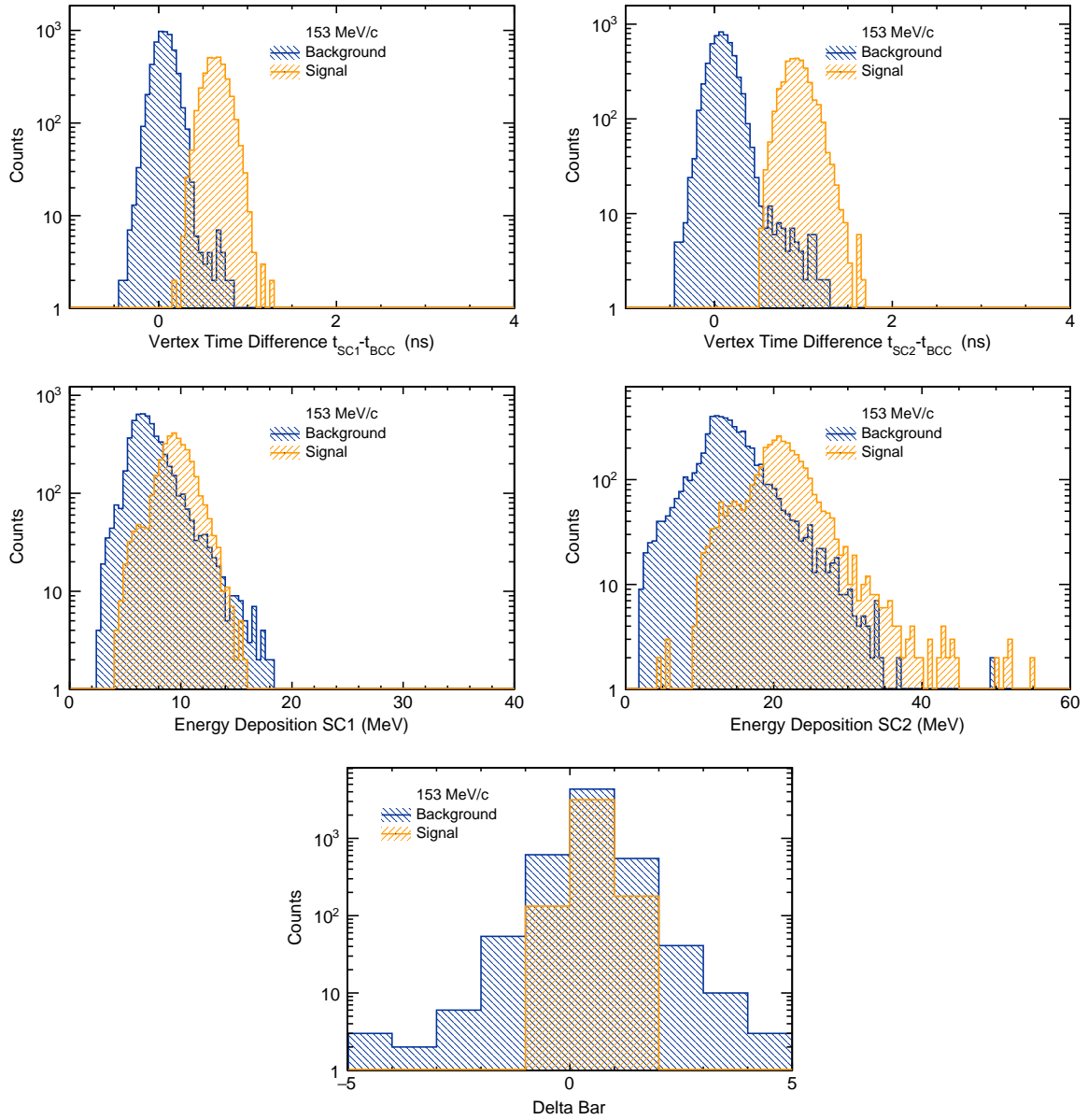


FIG. 39. Simulated timing, energy, and detector correlations for muon-scattering signal and muon-decay background and a beam momentum of 153 MeV/ $c$ .

events. These effects can be corrected for with data from the simulation (after validation) and/or with background measurements.

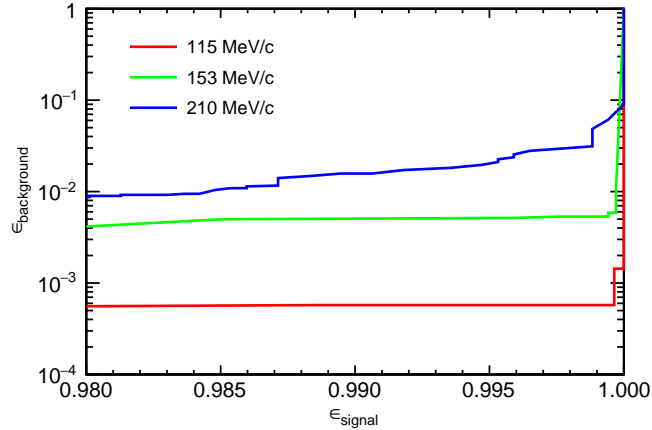


FIG. 40. Neural-network result for the discrimination of muon-scattering signal from muon-decay background at beam momenta of 115, 153, and 210 MeV/ $c$ . The red curve for example indicates that one can obtain near 100% efficiency identifying scattering particles while only misidentifying  $< 0.1\%$  of decay particles. In the worst case, at 210 MeV/ $c$ , one can reduce the decay events by 99% while retaining over 98% of the scattering events. There is a large relative uncertainty in the 115 MeV/ $c$  and 153 MeV/ $c$  results due to a lack of statistics because the remaining background after the neural net cut is very small.

### 3. Solid Angle

Determination of the cross section from the yields requires knowing the solid angle. The MUSE beam size is sufficiently large that a realistic beam profile needs to be taken into account in calculating the solid angle. We have studied the solid angle in Monte Carlo. Figure 41 shows the estimated geometrical acceptance. We have also studied the effects of offsets in the relative positions of the target, beam, and detectors on the solid angle - the systematic uncertainty. Generally the solid angle is not much changed except at the edges of the acceptance, and we are most sensitive to offsets along the beamline, since offsets transverse to the beamline cancel. These studies have led to a specification that the relative positions be determined at the  $100\mu\text{m}$  level.

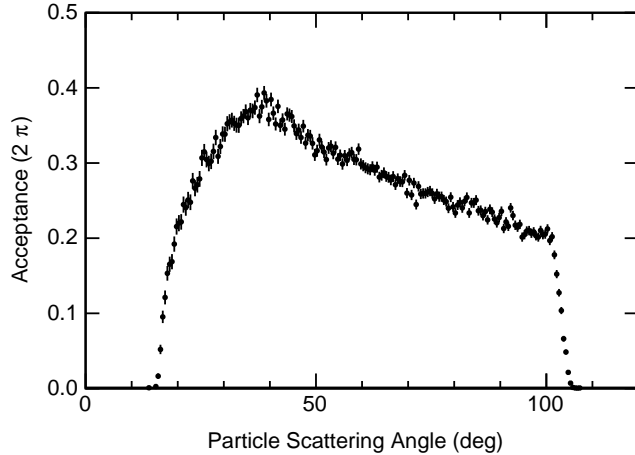


FIG. 41. Estimate of the geometrical acceptance of one scintillator wall as the fraction of high-energy muons originating uniformly distributed from the target which hit the straw chambers and front and back scintillator walls.

#### 4. Projected Data with Statistical Uncertainties

Using the information given above, it is possible to take the run plan, make rate estimates for these processes, take into account various inefficiencies and the increases in uncertainties from measuring and subtracting backgrounds, and work out the resulting statistical uncertainties. This is shown in Fig. 42 for the positive polarity  $\mu^+p$  scattering and Fig. 43 for  $\mu^-p$  scattering. For both polarities  $ep$  uncertainties are a factor of a couple times smaller due to the greater particle flux and the lack of a decay background to be cut and subtracted. Some momenta shown have generally larger uncertainties due to a smaller  $\mu$  flux than at other momenta. Uncertainties generally increase with  $Q^2$  or angle due to the decreasing cross section. The statistical uncertainties are below the 1% level for most of the data set, but grow to about 2% in the least precise cases. Thus the form factor will be determined to better than about 1% in all cases. Negative polarity beams have more electrons and fewer muons, leading to increased uncertainties for the muons when measuring for the same integrated luminosity.

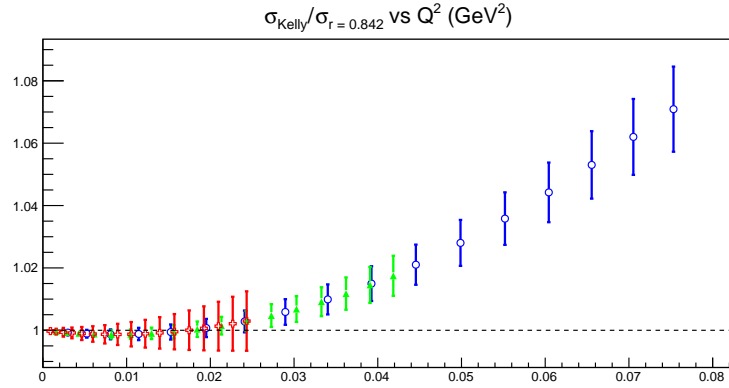


FIG. 42. Estimated statistical uncertainties for  $\mu^+p$  elastic scattering cross sections, after background subtraction, and including experimental inefficiencies. Each point corresponds to a  $5^\circ$  bin in scattering angle.

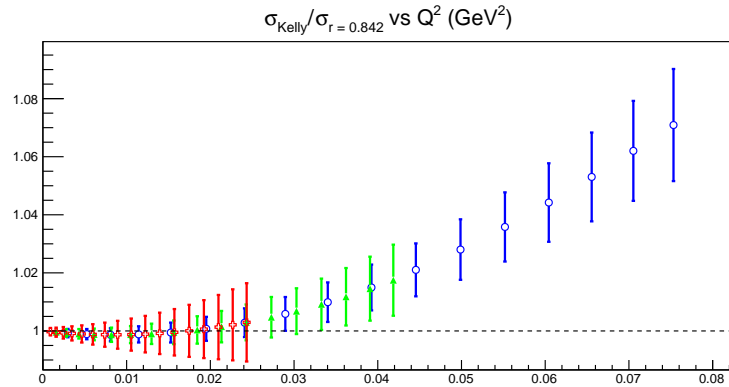


FIG. 43. Estimated statistical uncertainties for  $\mu^-p$  elastic scattering cross sections, after background subtraction, and including experimental inefficiencies. Each point corresponds to a  $5^\circ$  bin in scattering angle.

### 5. Derived Data with Statistical Uncertainties

From the cross sections shown in Figs. 42 and 43, we will construct ratios to determine the consistency of the “electron” and “muon” form factors, and the size of two-photon effects.

Figure 44 shows the ratio of  $\mu p$  to  $ep$  elastic cross sections. The ratio is not unity due to terms in the full cross section formula proportional to  $m/E$  and  $m/M_p$ , which are about 0 for the electron. We neglect this to show the relative statistical uncertainty

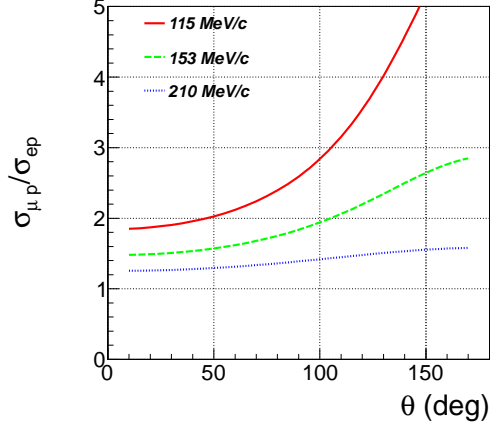


FIG. 44. Calculated ratio of  $\mu p$  to  $ep$  elastic cross sections at the same angle.

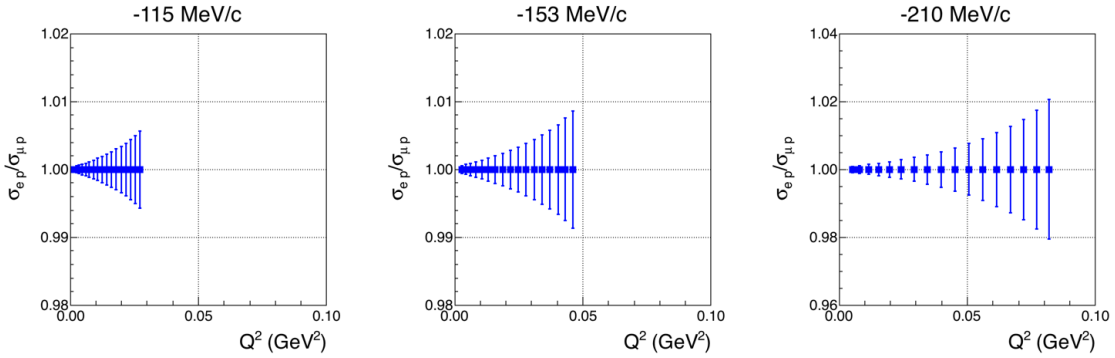


FIG. 45. Relative uncertainty in the ratio of  $\mu p$  to  $ep$  elastic cross sections. The relative statistical uncertainties in the form factors are half as large, since  $d\sigma/d\Omega \propto G^2$ .

in the cross section ratio, in Fig. 45. The statistical uncertainties are dominated by the  $\mu p$  uncertainties which are a few times larger. Ultimately, we will want to compare the electric form factor at the same  $Q^2$ . For the form factor, the statistical uncertainty is reduced a factor of 2, compared to the cross section ratio, as  $d\sigma/d\Omega \propto G^2$ , but there are additional systematic uncertainties, from comparing the cross sections in the same angle bin vs. the form factors in the same  $Q^2$  bin. It can be seen that the form factor ratio will have statistical uncertainties generally below 1%.

The ratios of positive polarity cross section to negative polarity ones differs from unity

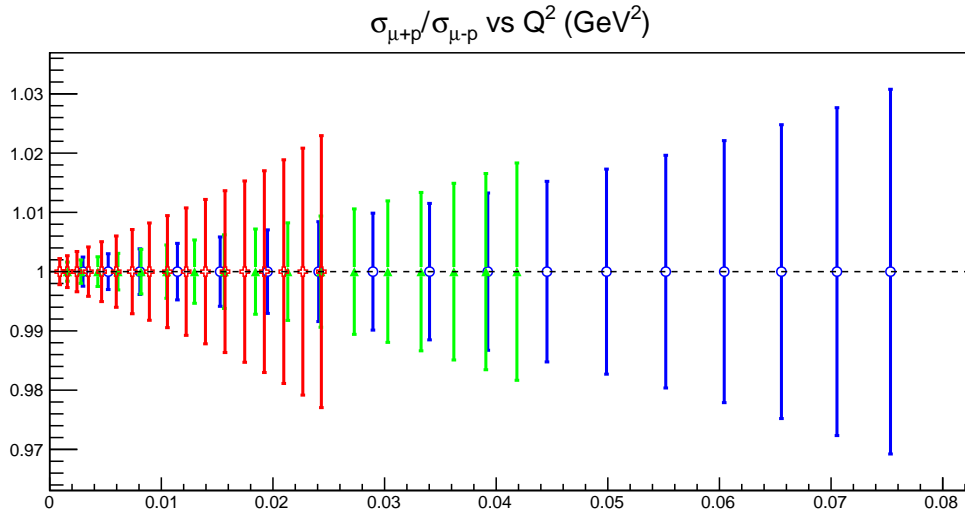


FIG. 46. Relative uncertainty in the ratio of  $\mu^+p$  to  $\mu^-p$  elastic cross sections.

due to the two-photon exchange contribution, which reverses sign between positive and negative polarities. The size of the effect varies with  $Q^2$ , and is typically not more than a few percent, but calculations disagree with the best existing data at the percent level. The relative statistical uncertainties for the ratio of positive to negative polarity cross sections for muons are shown in Fig. 46; uncertainties for the electron ratios are a few times better. Some theoretical estimates are in Section VII B. There are no existing data in this  $Q^2$  range; there are two  $\approx 4\%$  points at  $Q^2 \approx 0.15 \text{ GeV}^2$ , to be compared with the 48 often much more precise projected data shown here.

## B. Corrections

The  $ep$  and  $\mu p$  cross sections determined from the background-subtracted yields must be corrected for a number of experimental and theoretical effects. The experimental efficiency corrections included in Eq. (1) are all standard, so we do not discuss them further. Resolutions and multiple scattering lead to an angle averaging, which warps the cross section as shown in Fig. 58 in Appendix B. This effect can be corrected by either calculation or Monte Carlo, and we do not discuss it further.

There are three types of theoretical corrections we discuss here: magnetic and  $Q^2$

corrections, radiative corrections, and two-photon exchange corrections.

### 1. Magnetic and $Q^2$ Correction

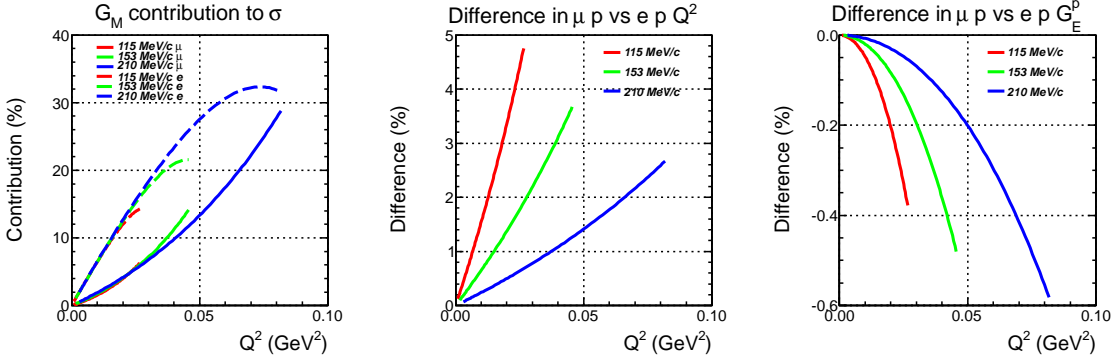


FIG. 47. Corrections related to extracting the electric form factor from the cross section for comparison at constant  $Q^2$  rather than constant scattering angle. Left: Portion of the cross section coming from the magnetic form factor  $G_M$ . Solid (dashed) lines for  $\mu p$  ( $ep$ ) elastic scattering. Middle: Percentage difference in  $Q^2$  between  $\mu p$  and  $ep$  elastic scattering at the same beam momentum and angle. Right: The difference in the electric form factor arising from the different  $Q^2$ . All estimates use the Kelly form factors.

To extract and compare the proton electric form factors and *electric* radius with  $ep$  and  $\mu p$ , corrections have to be made for the magnetic contribution to the cross section and for the  $Q^2$  difference between  $\mu p$  and  $ep$  elastic scattering at the same beam momentum and angle. Figure 47 shows factors related to this determination. The magnetic contribution ranges up to about 30% at the largest angles. In the range of the MUSE experiment, fits of the Bernauer data suggest that the uncertainty in the magnetic form factor is  $\leq 0.3\%$ . The uncertainty of the magnetic contribution to the cross section is then  $\leq 30\% \times 0.3\% \approx 0.1\%$ . The changes in  $Q^2$  are purely kinematic.

### 2. Radiative Corrections

Radiative corrections procedures for electron-proton scattering are well established, and numerous codes exist. The precision of the corrections is limited by approximations in



the codes, the precision with which the experiment is known (acceptance, bin kinematics, etc.), and the knowledge of the form factors. The important difference for  $\mu p$  scattering vs.  $ep$  scattering is that the larger muon mass suppresses the emission of bremsstrahlung radiation. However, most older codes assume the peaking approximation and / or the ultra-relativistic approximation ( $m/E \rightarrow 0$ ). Afanasev has accounted for these effects and provided us with an exact calculation of the muon bremsstrahlung correction in MUSE kinematics. The correction is near zero at  $\theta = 0^\circ$ , and grows with angle and beam momentum, becoming as large as 3% for  $\theta = 100^\circ$  at a beam momentum of 210 MeV/ $c$ . Afanasev estimates the uncertainty in the correction to be over an order of magnitude smaller than the correction, around the 0.1% level. The correction for  $ep$  scattering is about 5 times larger and similarly less precise. These estimates need to be re-evaluated when the experiment is assembled and the actual uncertainties can be evaluated.

### 3. Radiative Corrections and Beam Momentum

The beam momentum at the interaction point is degraded from the momentum out of the channel due to interactions with detectors before the target. A major part of this energy loss is external bremsstrahlung, part of the radiative corrections. Figure 48 shows a Geant4 calculation of the beam momentum entering and exiting the target, starting from a flat channel momentum distribution  $\pm 1.5\%$ -wide.<sup>9</sup> The energy shifts are similar at the three beam settings, leading to larger fractional momentum shifts at the lowest beam momentum setting. We can use these calculated momentum distributions to study corrections from the spectrum shape. We compare the average of the cross sections from the calculated spectrum to the cross section at the central momentum of the spectrum. The right panel of Fig. 48 shows that this is about 0.05% – 0.1%, and the variation with angle is about 0.01%. Thus knowing the average momentum is sufficient to make this correction quite small.

---

<sup>9</sup> The distributions will also be *measured* as part of our simulation calibration program.

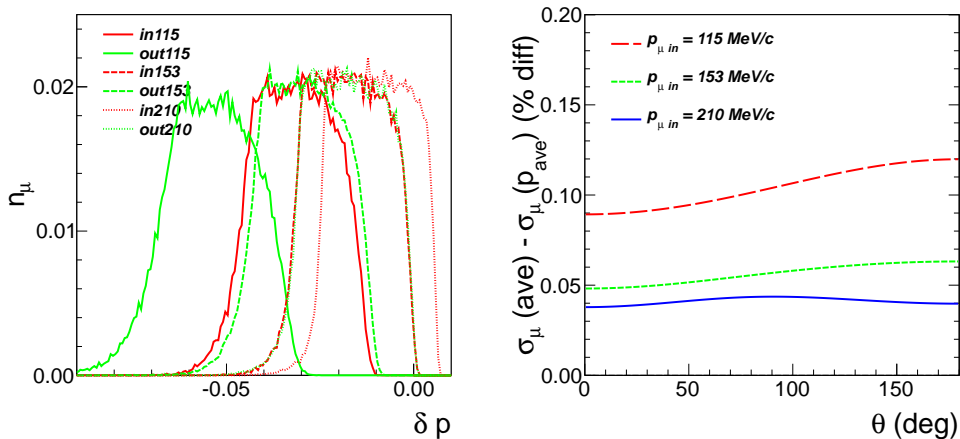


FIG. 48. Left: Momentum spectrum for beam muons entering and exiting the target. A fractional number of events per bin is plotted vs. the momentum relative to the central momentum of the  $\pi$ M1 channel. Right: Difference between the cross section calculated for the average beam momentum and the cross section averaged over the incident spectra shown to the left.

#### 4. Two-photon exchange

At very low  $Q^2$ , calculations of two-photon exchange (TPE) within a hadronic framework [18–20] are typically expected to be reliable, and are in good agreement with a low  $Q^2$  TPE expansion [21], which is expected to be valid up to  $Q^2 = 0.1 \text{ GeV}^2$ , therefore covering our entire  $Q^2$  range. The recent generation of higher precision (TPE) measurements comparing cross sections for  $e^+p$  and  $e^-p$  shows that TPE is small, at the percent level, but at this level it is also significantly different from calculations. For  $\mu p$ , the calculations have additional uncertainties from the knowledge of helicity-flip amplitudes. The calculations also depend on what intermediate states are included. There have been two calculations of conventional, or soft, TPE calculations for MUSE, both predicting small effects on the MUSE cross sections. These calculations can be benchmarked to low- $Q^2$  measurements of the imaginary part of TPE, for example the upcoming results from the measurement of the beam normal single spin asymmetry for the Qweak experiment.

Afanasev’s calculations (see Fig. 49, left) of TPE show an effect that approaches zero at forward angles and increases with scattering angle. The effect is no more than about

0.2% in MUSE kinematics, with little difference seen between the correction for muons and for electrons, and estimated uncertainties about half of the correction. Tomalak & Vanderhaeghen [22] calculate the expected corrections for  $\mu^-p$  and find it varies between 0.25% - 0.5% (see Fig. 49, right).

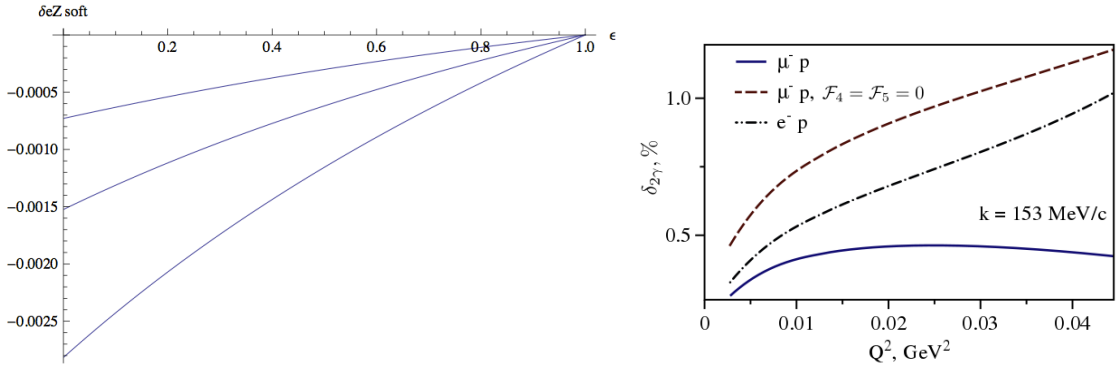


FIG. 49. Calculations of TPE for  $\mu p$  cross sections. Left:  $ep$  TPE corrections for the three MUSE beam energies as a function of  $\epsilon$  calculated by Afanasev. The correction grows with energy. The muon calculations are very similar. Right:  $\mu^-p$  and  $e^-p$  TPE corrections calculated by Tomalak [22]. The red-dashed curve shows the muon correction without accounting for the helicity-flip amplitude.

The approach in MUSE is to directly measure the TPE effect in  $ep$  and  $\mu p$  scattering by comparing the cross sections for positive and negative polarity beams, rather than relying on calculations, since these measurements directly test physics that might help explain the proton radius puzzle.

### C. Systematics

Estimated systematic uncertainties are shown in Table XVII, based on the analysis in Appendix B. We focus on relative uncertainties here since the absolute uncertainties cannot be determined precisely enough, at the few tenths of a percent level, so that the data can be used without a normalization factor. Instead we cross normalize the angular distributions to each other and to the  $Q^2 = 0$  form factors. We summarize here various aspects of the systematics.

TABLE XVII. Estimated MUSE relative systematic cross section uncertainties for the shape of angular distributions, the ratio of muon and electron scattering cross sections, and the ratio of + charge to  $-$  charge cross sections.

Uncertainty	angular distribution (%)	$\mu/e$ (%)	+/ $-$ (%)
Detector efficiencies	0.1	0.1	0.1
Solid angle	0.1	small	small
Luminosity	small	small	small
Scattering angle offset	0.2	small	small
Multiple scattering correction	0.15	small	small
Beam momentum offset	0.1	0.1	0.1
Radiative correction	0.1 ( $\mu$ ), 0.5 ( $e$ )	0.5	1 $\gamma$ small
Magnetic contribution	0.15	small	small
Subtraction of $\mu$ decay from $\mu p$	0.1	0.1	small
Subtraction of target walls	0.3	small	small
Subtraction of pion-induced events	small	small	small
Beam PID / reaction misidentification	0.1	0.1	0.1
Subtraction of $\mu$ decay from $ep$	small	small	small
Subtraction of $ee$ from $ep$	small	small	small
TOTAL	0.5 ( $\mu$ ), 0.7 ( $e$ )	0.5	0.2

### 1. Beam Detector Related Systematics

It is a good approximation that beam detectors do not change the angular distribution of scattered particles, so the related systematic uncertainty vanishes. There is a small probability of mis-identified reaction types that do change the shape of the angular distribution. By measuring the shape of these background angular distributions and quantifying how they are misidentified and mixed into the data, their effects can be subtracted.

### 2. Beam Momentum Determination Systematics

We showed that beam momentum offsets and averaging over beam momentum distributions lead essentially to a renormalization of the data with small angle-dependent

variations, at or below 0.1%. We plan to control this systematic with beam momentum and energy loss measurements, using a combination of time of flight and channel dispersion techniques. We have demonstrated absolute muon and pion momentum measurements at the needed 0.2% – 0.3% level, and estimated from TURTLE simulations that the relative momentum of all particle types can be determined to  $\ll 0.1\%$ .

### 3. Target Systematics

The target thickness varies with trajectory, and multiple scattering in the upstream detectors leads to slightly different beam spots for different particles and beam momenta. However we measure the particle dependent trajectories into the target, so corrections can be made through the simulation.

### 4. Scattered Particle Detector Systematics

The scintillators and straw chambers are designed so that we have very high detection and tracking efficiencies, near 100%, so that there is little room for the angular distribution shape to be changed. There is only a  $\approx 99\%$  efficiency for  $e^+$  due to positron annihilation, for which we estimate a 0.1% relative systematic uncertainty.

While the rate varies across the detector angular range, the rates are sufficiently low that even for the most forward scintillator bars the dead time will only be  $\approx 0.1\%$ . The dead time can be deduced from scaler readings.

The experiment is sensitive to offsets in the measured angles and multiple scattering that averages the cross section, due to the sharply falling electromagnetic cross section. We have a program of calibration measurements to control both effects. These uncertainties strongly increase towards the forward angles, much smaller impact at larger angles.

### 5. Solid Angle

The determination of the solid angle is controlled through a combination of careful design and construction of equipment, temperature control, and survey and dedicated calibration measurements of equipment positions. The left/right and up/down symmetry

of our systems provide checks on offsets in those directions that might affect the solid angle. All the offsets have the largest effect on cross sections at our most forward and most backward scattering angles, where the acceptance is getting small.

### 6. Electronics, Trigger, and Computer Live Time Uncertainties

We use standard techniques to control electronics uncertainties, including scalers, measuring read out times, performing logic with multiple width pulses, using a random trigger, and taking data at multiple beam fluxes. We plan to calibrate the trigger at low beam rates and study its performance as a function of rate, monitoring in the fast DAQ the trigger inputs, intermediate stages, and final trigger.

### 7. Uncertainties in Theoretical Corrections

We do not consider uncertainties in the TPE calculations since MUSE will measure the TPE contribution directly. Radiative corrections for the muon, an example shown in Fig. 50, are estimated to be  $<3\%$ , with overall uncertainties about one-tenth of the correction, or  $0.3\%$  and angle-dependent variations smaller, about  $0.1\%$ . Electron radiative corrections and uncertainties are about 5 times larger. In the case of the muon, the radiative tail is quite small, whereas for the electron, the radiative tail is long, so the correction averages over a wider range of vertex kinematics from pre-radiation.

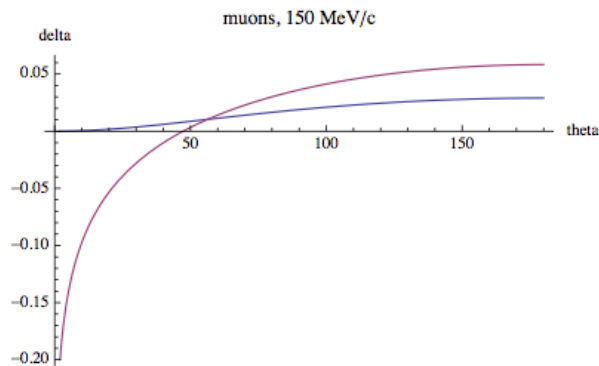


FIG. 50. Radiative correction calculation from Afanasev showing the muon radiative corrections at 150 MeV/c for MUSE. The blue (red) curve is the full (approximate) calculation.

### 8. Analysis and Instability Uncertainties

Additional systematic uncertainties might arise from the analysis procedures or instabilities in the data. For example, the cross section varies over time or with a range of reasonable cuts by some amount, with no good explanation as to why. The variation presumably reflects some unidentified systematic effect, and can be used to estimate an uncertainty from the unknown effect. It is not possible at this time to assign an uncertainty here.

### 9. Systematic Uncertainties for Ratios

As shown in Table XVII, certain factors are the same or very close to the same when comparing  $ep$  to  $\mu p$  or  $+$  to  $-$  cross sections, which results in some cancellations of the systematic uncertainties. The mass effects limit the cancellations in  $ep$  vs.  $\mu p$ .

#### D. Radius Extraction

The direct comparison of  $\mu p$  and  $ep$  cross sections, corrected for the effects of the muon mass, or the extracted electric form factor, will make it clear in the MUSE experiment whether the two particles have different interactions or not. If there is a difference, the comparison of  $+$  and  $-$  charge cross sections should make it clear if two-photon exchange might be responsible for the difference. But the radius, extracted from the slope of the form factor at  $Q^2 = 0$ , directly connects to the atomic physics measurements. Since we do not measure at  $Q^2 = 0$ , the radius relies on fitting the measured data with a form factor parameterization. In this section we very briefly discuss the radius extraction and the resulting uncertainties.

We consider here the standard approaches of doing simple polynomial fits – note the criticism of this approach in [25] – and of doing inverse polynomial fit to the data sets. Pade fits have too many parameters for the MUSE data range, and  $z$ -expansion fits yield similar results to what we present. We followed the fitting procedures of [25], and have consistent results for our polynomial fits.

We fit pseudodata, with the data generated according to various world parameteriza-

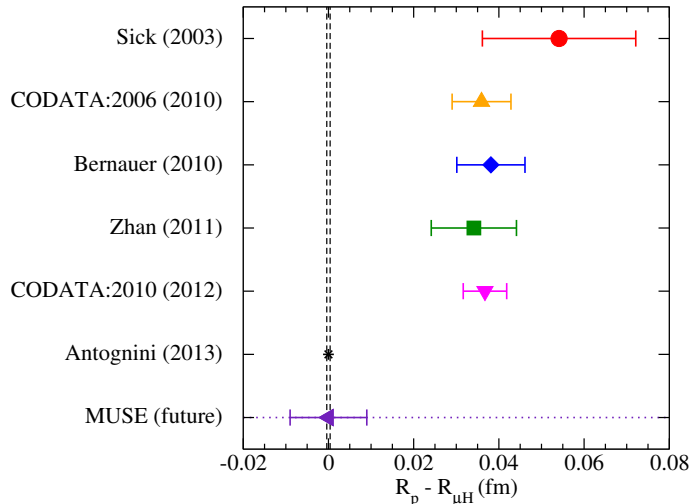


FIG. 51. A summary of some recent proton charge radius determinations, relative to the muonic hydrogen result, including Sick [23], CODATA 2006 [24], Bernauer *et al.* [3], Zhan *et al.* [4], CODATA 2010 [5], and Antognini *et al.* [2], which includes Pohl *et al.* [1], along with our expected MUSE result, arbitrarily placed at 0.

tions and with our expected uncertainties. We used the same generating functions for  $ep$  and  $\mu p$  and fit the same way, and compared the results and the differences in the results. Table XVIII summarizes our results. In comparing  $ep$  to  $\mu p$ , fitting issues largely go away and the difference is reliable – if as assumed here the form factors are the same in both cases. In first order fits, the truncation error is larger than the uncertainty, especially for polynomial fits, so the absolute radius is unreliable. Going to a second order fit increases the uncertainty and reduces the truncation error, making the extracted radius more reliable. Going from polynomial to inverse polynomial fits reduces the truncation error while leaving the uncertainty approximately unaffected. Thus we advocate for a first-order inverse polynomial fit to compare  $ep$  to  $\mu p$  most precisely, and, if the extracted radii are consistent, a joint fit of the  $ep$  and  $\mu p$  data sets with a second order inverse polynomial fit to obtain the absolute radius. The difference fit gives an  $\approx 8\sigma$  determination of the possible 0.04 fm difference, while the joint fit gives an  $\approx 5\sigma$  determination of the absolute radius.



TABLE XVIII. Typical results from fitting estimated MUSE data for several generating functions.

	Truncation Error		Uncertainty		$ep$ vs. $\mu p$
	$ep$ (fm)	$\mu p$ (fm)	$ep$ (fm)	$\mu p$ (fm)	difference (fm)
First order polynomial	-0.050	-0.048	0.003	0.003	-0.002
Second order polynomial	-0.005	-0.005	0.009	0.007	0.001
First order inverse polynomial	0.007	0.007	0.004	0.003	0.001
Second order inverse polynomial	-0.001	-0.001	0.01	0.008	0

TABLE XIX. MUSE project WBS tasks and responsible people.

Task/WBS	Responsible Persons	Institution
Management	Gilman/Cioffi/Reimer/Briscoe	Rutgers/GW/Argonne/GW
Frames and Design WBS 1	Reimer	Argonne
Scintillator/Silicon photodetector WBS 2	Piasetzky	Tel Aviv Univ.
Cerenkov detector WBS 3	Gilman	Rutgers
Wire Chambers WBS 4	Ron	Hebrew
Cryogenic Target WBS 5	Lorenzon	University of Michigan
Electronics and DAQ WBS 6	Downie	George Washington
Scintillators WBS 7	Strauch	South Carolina
GEM chambers WBS 8	Kohl	Hampton
Installation WBS 9	Briscoe	GW
Software WBS 10	Golossanov	GW
Data Taking WBS 10	Downie	GW

## VIII. PROJECT MANAGEMENT

The MUSE construction project has put in place a formal project management structure due to the extent and cost of the construction project. The project manager team consists of:

- R. Gilman (Rutgers) Project Manager. Professor Gilman stepped down as MUSE spokesperson to take over project management for the experiment, as he was the best fit for the position.

- D. F. Cioffi (George Washington) Deputy Project Manager. Professor Cioffi taught project management at GW for more than ten years, during much of that time he was director of the master's Project Management Program. He has extensive federal government experience, including being a National Science Foundation Associate Program Director (1991). A faculty member of the Decision Sciences Department, he currently serves as Senior Advisor to the Dean of the Business School, as well as retaining an appointment in the Physics Department.
- P. Reimer (Argonne National Laboratory) Deputy Project Manager. Dr. Reimer has played a lead role in a number of experiments, and most recently served as deputy project manager for the Fermilab SeaQuest experiment.
- W. J. Briscoe (George Washington) Deputy Project Manager. Professor Briscoe is currently Chair of the Department of Physics at George Washington University. He has managed several large experimental efforts.

The project management is described in detail in the Project Execution Plan; the final version was submitted to NSF on June 1, 2017. The Plan covers numerous topics including the Work Breakdown Structure, responsible people, key performance parameters, milestones, risks and risk management, contingencies, project oversight and communication, and the funding profile.

This material is based upon work supported by the National Science Foundation under Grant Numbers OISE-1150594, PHY-1205782, PHY-1207672, PHY-1306126, PHY-1309130, PHY-1314148, OISE-1358175, PHY-1401974, PHY-1404271, PHY-1404342, PHY-1505458, PHY-1505615, PHY-1505934, PHY-1506000, PHY-1506061, PHY-1506160, PHY-1612495, PHY-1614456, PHY-1614773, PHY-1614850, PHY-1614938, PHY-1649873, HRD-1649909, and PHY-1714833; the Department of Energy under Grant Numbers DE-SC0012485, DE-0012589, DE-AC02-06CH11357, and DE-SC0013941; the Schweizerischer Nationalfonds under grant numbers 200020-156983, and 2015.0594; and the Binational Science Foundation under Grant Number 2015618, 2015625, and 2014709; and the Paul Scherrer Institute.

### A. Collaboration

The MUSE collaboration is comprised primarily of people with experience in electron scattering experiments, some of whom have worked together for over 20 years. The collaboration lead spokesperson is E. Downie (GW), with deputy spokespeople G. Ron (HUJI) and S. Strauch (SC). The collaboration has experience with experiments of the size and scale of MUSE, primarily electron and photon scattering experiments. The core of the collaboration comprises the institutions constructing the experimental equipment. A summary of some commitments beyond what is reported in Table XIX on the WBS structure is shown in Table XX. The collaboration formalized its structure by adopting a charter at its January 2014 meeting, and has regularly held collaboration meetings since.

TABLE XX. Some MUSE collaboration responsibilities not covered by the WBS structure.

<b>Responsibility</b>	<b>Person</b>	<b>Institution</b>
$\pi$ M1 Channel	K. Deiters	PSI
Trigger	R. Gilman (Project Manager)	Rutgers
Radiative Corrections	A. Afanasev	George Washington
Analysis Software	J. Bernauer	MIT
Simulations	S. Strauch	South Carolina

## Appendix A: Backgrounds

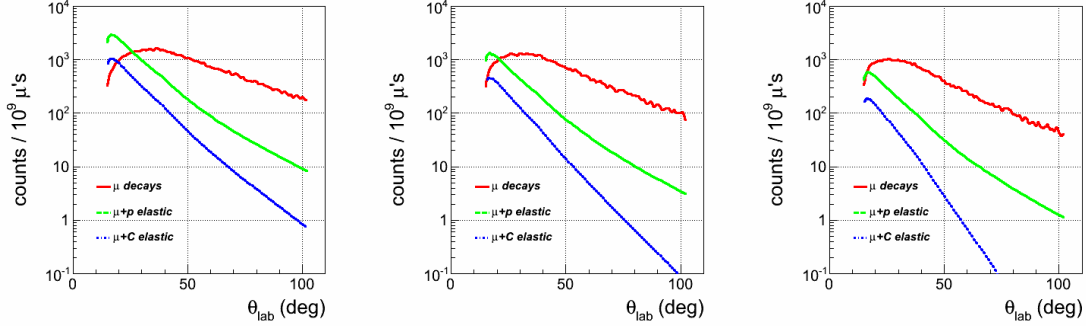


FIG. 52. Estimated rates at 115 MeV/ $c$  (left), 153 MeV/ $c$  (middle), and 210 MeV/ $c$  (right) as a function of angle for muon elastic scattering from protons and from carbon in the target end caps, and for electrons from muon decays in flight in a 10 cm region near the target. The counts shown are based on the detector geometry,  $1^\circ$  angle bins, and  $10^9$  incident  $\mu$ 's, corresponding to about 1 hour of data. Elastic scattering rates were directly calculated, while in-flight muon decay rates are from a numerical simulation.

In this appendix we enumerate many of the physics backgrounds in the MUSE experiment. The MUSE experiment goal is to measure precise  $ep$  and  $\mu p$  elastic scattering cross sections. Backgrounds can increase uncertainties, due to cuts, subtractions, or DAQ dead times, as well as modify cross sections if not correctly handled.

Background processes include the following:

- For incident  $\mu$ 's: scattering from the target end windows, decaying in flight, and knocking out  $\delta$ 's from the target. The rates for elastic muon scattering and in-flight muon decay are shown in Fig. 52. The  $e$ 's from  $\mu$  decay have a wide range of angles due to the 3-body nature of the decay, as shown in Fig. 53, and, at the trigger level, resemble scattering events for decays near the target. An example of such an event is shown in the left panel of Fig. 54. Simulations (Section VII A 2) show that the muon decay background can be suppressed by at least 3 orders of magnitude at the lower momenta, and 2 orders of magnitude at 210 MeV/ $c$ , while maintaining high elastic scattering identification, by time-of-flight cuts in a neural network approach. Cell end-cap backgrounds are removed mainly by empty-target subtractions.

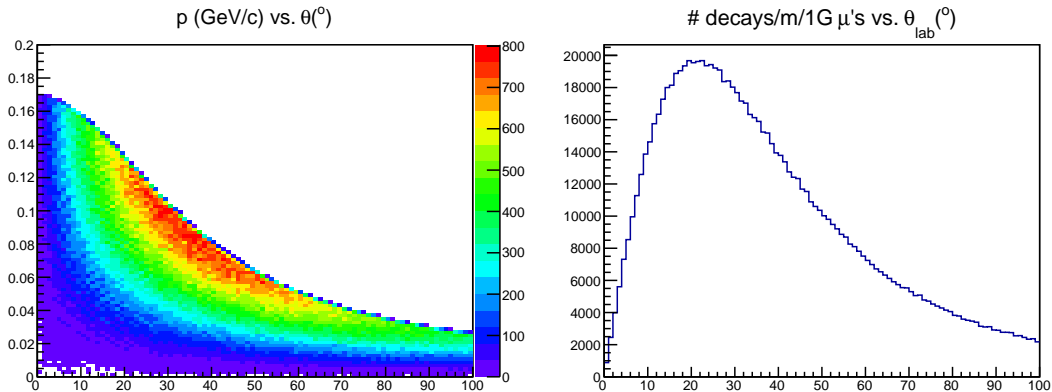


FIG. 53. Left: Simulation of  $e$  momentum vs. angle from decays in flight of 153 MeV/ $c$  unpolarized  $\mu$ 's. Right: A projection showing the angular distribution of the electrons from muon decays. The distribution shifts slightly to smaller or larger angles depending on muon polarization direction. The numbers of electrons are per meter of flight path and per  $10^9$  incident  $\mu$ 's.

- For incident  $e$ 's: scattering from the target end windows, Møller and Bhabha scattering from atomic electrons, and positron annihilation. Empty target subtraction removes the end window background. Møller and Bhabha electrons and positrons are suppressed because the large-angle, low-momentum particles do not efficiently trigger our system, and because the beam monitor scintillator allows further suppression at the analysis stage. A sample Møller event is shown in the right panel in Fig. 54. Positron annihilation at the target generates photons that we are inefficient at detecting, while annihilation of scattered positrons represents a potential inefficiency that can be understood and corrected through simulations. Note that radiative corrections are much more important for electrons and positrons than for muons.
- For incident  $\pi$ 's: all processes are backgrounds. Beam particle identification (PID) with beam line detector timing suppresses pion events at the trigger and analysis level.
- Beam background events: in-flight decays of  $\pi$ 's and  $\mu$ 's in the beam generate a halo of particles with large emittance as well as a momentum halo for the occasional  $\mu$  decay in the near- $0^{\circ}$  direction. Simulations and test data have shown that:

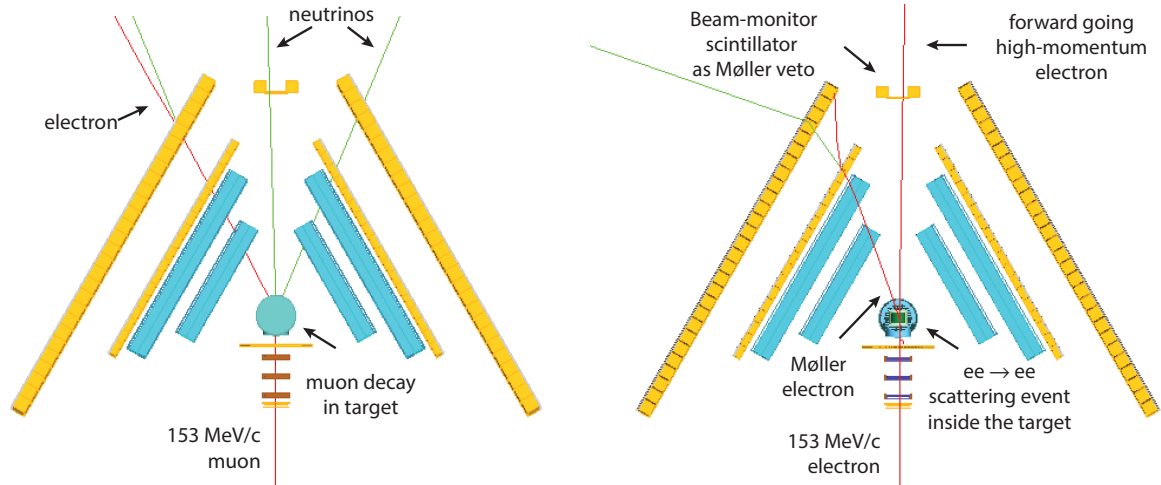


FIG. 54. Geant4 simulation showing two background events. Red tracks are charged particles, while green tracks are neutrals. Left: an apparent muon scattering event is actually a muon decay within the target. At the trigger level the outgoing electron forms a coincidence with the incoming muon. The electron knocks out several neutrals from the rear plane. Right: An incident electron Møller scatters in the target. The high-energy forward going electron is detected in the beam monitor, which can be used to greatly suppresses the Møller scattering. The scattered electron is low energy and multiple scatters in the front scintillator plane so that it ends up a few paddles from the expected position in the rear scintillator plane, but still causes a trigger.

- Decays of pions in the first few m of the channel, before magnetic elements, can lead to muons with timing in the tails of the muon RF timing peak.
- Decays within the magnetic elements of the channel are largely swept out of the acceptance, because the decay product has a momentum outside the channel acceptance.
- Decays after the magnetic elements of the channel are mostly at large angles to the beam direction, and, if detected in the beam line detector elements, add tails to the angle, position and time distributions.

Section VII A describes in more detail estimated uncertainties resulting from removing backgrounds through cuts and subtractions.

## Appendix B: Systematic Uncertainties

In this appendix we present details of some experimental systematics that lead to the experiment performance requirements. At the smallest MUSE  $Q^2$  setting, 0.0016 GeV<sup>2</sup>, the elastic cross section differs from that of a point particle by  $\approx 1\%$ . Absolute uncertainties will almost certainly be at least twice as large, so the data need to be normalized to the  $Q^2 = 0$  point, and it is the relative systematic uncertainties that are important.

The relative systematic uncertainties are typically at the few-tenths of a percent level, and can be divided into two categories. First, the factors in Eq. (1) can be systematically different from angle to angle. Second, the cross section depends strongly on  $Q^2$ , so offsets in determining the kinematics can change the extracted form factors. Overall systematics, such as the factors  $N_{beam}$  and  $(x\rho)_{target}$ , and beam line detector efficiencies, are the same independent of scattering angle, so the relative uncertainty vanishes. Our goal is to measure the relative cross section with systematic uncertainties of 0.4% for muons and 0.6% for electrons.

The solid angle  $\Delta\Omega$  can be calculated by integrating  $\Delta\Omega = dA/r^2 = (dxdy)/r^2$ . For MUSE, we have to integrate not only over the detector, but also over the target volume including the spatial distribution of the beam. We have also studied the systematic uncertainty in the solid angle arising from offsets in the chamber position and orientation relative to the beam and target. The essential finding is that the relative solid angle uncertainty is greatest at the edges of the acceptance, the most forward and most backward angles. As long as the chamber provides “full”  $\phi$  coverage – the arc of constant  $\theta$  reaches from the bottom to the top of the chamber, rather than ending on the sides – chamber offsets do not affect the  $\phi$  coverage much. Examining the numerical change in the solid angle vs offsets, we set a positioning knowledge requirement of 0.1 mm to keep cross section systematic uncertainties close to the desired 0.1% level. However, offsets in the directions transverse to the beam largely cancel due to the up/down and left/right symmetry of the experiment; analysis can be used to search for such offsets.

When binning data, the concern is how well the solid angle is known for a bin, which is determined by the precision of the straw chambers. Since reconstruction resolutions do not change the solid angle, what is important is that the chamber wire positions need

to be determined precisely. Standard machining techniques should allow determination of wire positions at the  $\approx 25 \mu\text{m}$  level<sup>10</sup>, compared to  $\approx 2.5 \text{ cm}$  wide bins, and a  $\approx 35 \text{ cm}$  distance to the pivot, so that relative solid angle uncertainties will be about 0.14%. We will use a traveling collimated source technique to measure wire positions at the  $\approx 50 \mu\text{m}$  level. But note that bin to bin fluctuations are correlated – if one bin is too wide the neighbor is too narrow, as long as there is no overall scale issue in the chamber. In effect, these are fluctuations that add noise to the data.

The detector system is designed for high detection efficiency, so that the angle-to-angle variation is below the tenths of a percent level. (At larger angles statistics will limit our ability to know the efficiency this well.) Scintillator thresholds will be calibrated with QDC spectra checked against simulations, with resulting uncertainties estimated to be  $< 0.1\%$ . Trigger programming will have to be carefully studied to ensure that it does not introduce paddle-dependent efficiencies. Straw chamber detection and tracking efficiencies should be  $\approx 100\%$  due to the use of redundant straw chamber planes.

Not evident in Eq. (1) is that the cross section varies with beam momentum and scatter-angle, so offsets in these can lead to changes in the cross sections that vary with angle. Offsets in beam energy,  $E$ , change the scattering kinematics and factors of  $E$ ,  $E'$ , and  $Q^2$  that go into the cross section formula, and lead to the form factor being determined at the wrong  $Q^2$ . Multiple scattering and tracking detector resolution move events from bin to bin, with multiple scattering having a much larger effect.

Figure 55 shows the sensitivity of the measured cross sections to offsets in the beam energy and to averaging over the  $\pi\text{M1}$  momentum acceptance. For the planned kinematic coverage of  $20^\circ - 100^\circ$ , both effects act roughly as overall normalization offsets. As the data will be renormalized in the end, the important issue is the angle-to-angle variations of the curves in Fig. 55, not the offsets from 0.

The beam momentum distribution will be measured by monitoring the flux with beam-line detectors as the IFP collimator is set to a thin slit and moved across the acceptance. (It is also possible to measure with an active detector at the IFP.)

The central beam momentum is more difficult. Knowing the beam momentum at the  $\approx 0.3\%$  level will keep this systematic to below 0.1% (0.05%) on the cross section ( $G_E$ ) and

<sup>10</sup> At this level of precision, temperature control is required.



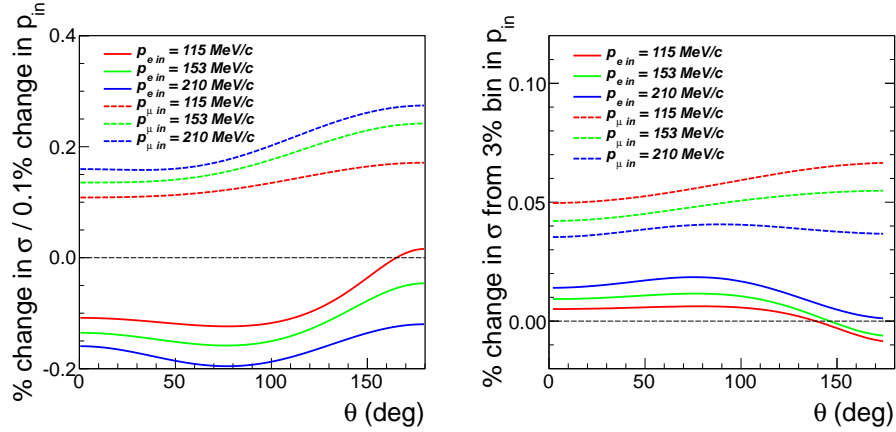


FIG. 55. Left: Change in cross section in percent for a 0.1% change in the beam momentum. Right: Change in cross section in percent when averaging over a  $\pm 1.5\%$  bin in the beam momentum. We assumed a uniform distribution in incident momentum, and evaluated the average cross section for the full momentum bin compared to the cross section for a mono-energetic beam at the central momentum. Both studies used the Kelly form factor parameterization [9].

thus it will be nearly insignificant. We have in test measurements determined the muon beam momentum at a level of  $\approx 0.2\%$  or  $0.3\%$  through time-of-flight measurements, using multiple positions of the thin target scintillators and measuring time of flight to the beam monitor. We have also verified the channel dispersion and checked the consistency of the pion and muon momenta.

The electron beam momentum cannot be measured with time of flight. We have a proof of principle demonstration from TURTLE simulations of the channel that we can turn off the downstream quadrupoles after the final dipole, to obtain a dispersion of about 7 cm / % at the PiM1 target. By combining RF time +time of flight measurements to identify particles with position measurements, we should be able to again vary collimator position at the central dispersion point of the channel and check the consistency of electron, muon, and pion momenta at close to the 0.01% level. A first test measurement with this technique is planned for June 2017. We note that this technique also allows us to verify simulations of energy loss in materials.

We conclude that the beam momentum distribution can be determined well enough that the residual systematic uncertainty on the cross sections will be no more than about 0.1%,

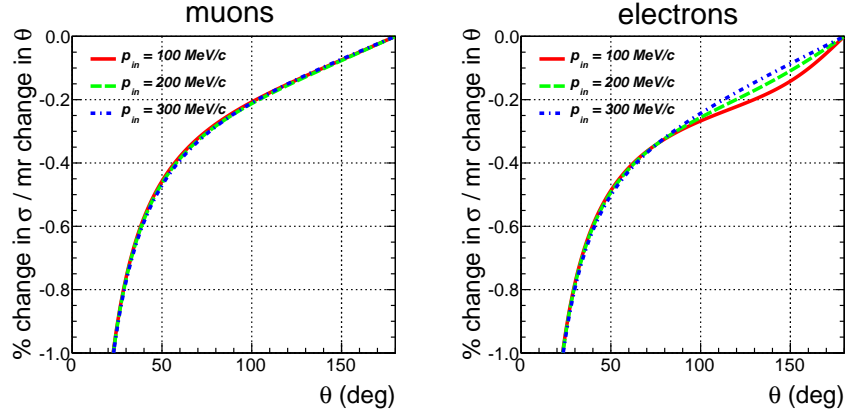


FIG. 56. Change in cross section from a +1 mr offset in the scattering angle. Estimates were done with the Kelly form factor parameterization [9].

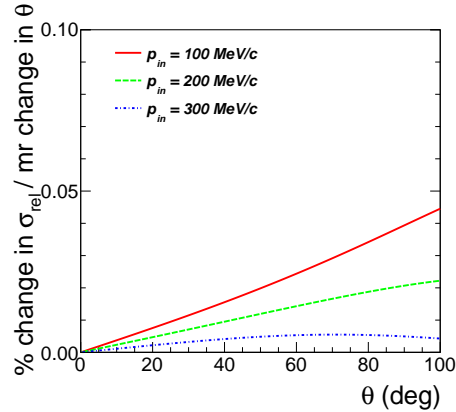


FIG. 57. Relative change in cross section – the change in the ratio of cross sections of  $\mu p$  to  $ep$  scattering – from a +1 mr offset in the scattering angle. Estimates were done with the Kelly form factor parameterization [9].

with the uncertainty on the electric form factor about 0.05%. Section VIIC2 provides more detail, including a more realistic (Geant simulated) beam momentum spectrum, but the conclusions are unchanged.

Figure 56 shows that offsets in the scattering angle change the cross section, which changes the slope of the form factor vs.  $Q^2$  and the radius. For determining a precise absolute radius, an absolute scattering angle uncertainty at the 1 mr level leads to cross

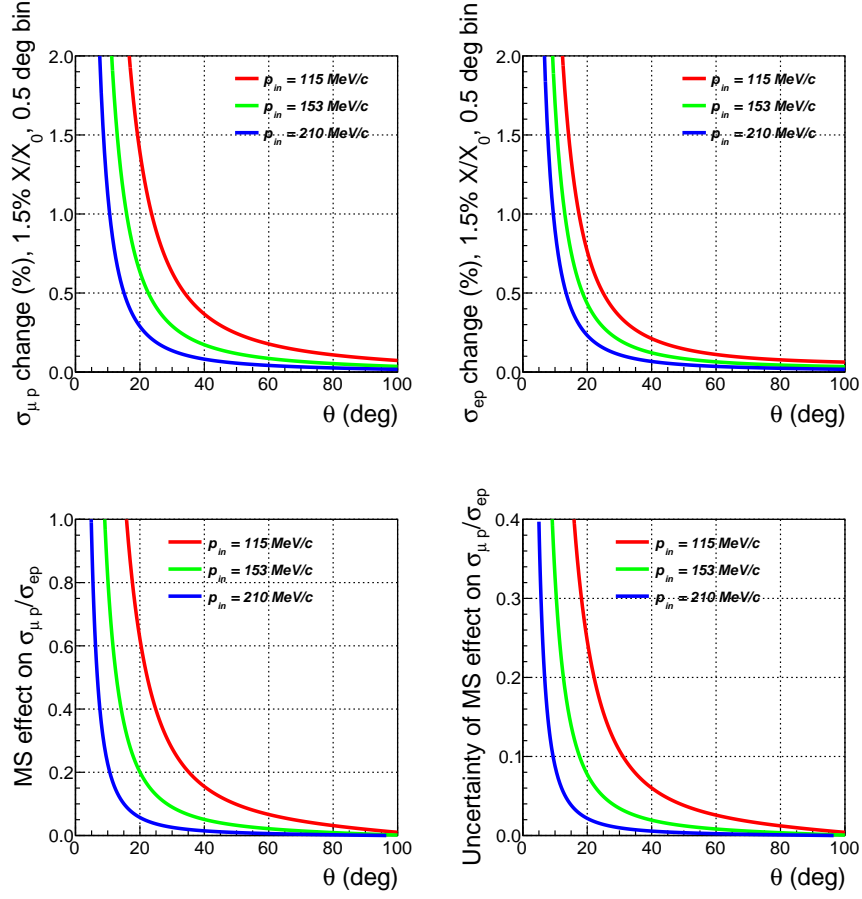


FIG. 58. Top: Change in the cross section from multiple scattering. Bottom left: Same calculation applied to the ratio of  $\mu p$  to  $ep$  cross sections. Bottom right: Estimated uncertainty in the Gaussian approximation. We assume the approximation is exact, and calculate the difference in the multiple scattering correction for the best estimate of  $X/X_0 = 1.5\%$  and  $X/X_0 = 1.67\%$ , about 11% more material.

section uncertainties at the 1% level, close to the allowed limits. Section VI describes a dedicated calibration measurement to determine the spectrometer angles to  $\approx 0.2$  mrad with dedicated calibration data. We precisely rotate the straw chambers into the beam behind the GEMs, and use high energy particles to limit multiple scattering. Thus the angle offset effect should be below 0.2%, with a relative uncertainty at the 0.1% level.

Figure 58 shows the effect of multiple scattering, which averages over scattering angles. The estimates use the simple Gaussian approximation, the Kelly form factor parameterization [9], and material corresponding to  $X/X_0 = 1.5\%$  based on the thicknesses of the last

GEM chamber, the first straw chamber, and the cryotarget windows and liquid hydrogen cell. The multiple scattering effect is similar in shape at all beam momenta, but decreases in magnitude with momentum due to a  $1/p\beta$  dependence. The upper panels show that the multiple scattering effect quickly decreases with angle, with about 1% effects at forward angles. The lower left panel shows that the effect is partially canceled in considering the ratio of  $\mu p$  to  $ep$  scattering cross sections. Since the effect is known it can be corrected for. The lower right panel estimates how accurate the correction might be, comparing multiple scattering for two different amounts of material. The correction should be able to reduce the uncertainty from multiple scattering to be a factor of 2 or so smaller than the effect of multiple scattering. A simple estimate is that the uncertainty from multiple scattering is about  $0.3 \pm 0.3\%$  for the individual cross sections but only  $0.1 \pm 0.1\%$  for the ratio of cross sections. The uncertainty is half as large for the electric form factor.

In Geant4 simulations we have compared the reconstructed scattering angle with the actual scattering angle in the  $ep$  and  $\mu p$  reactions; see Figure 59. From similar simulations,

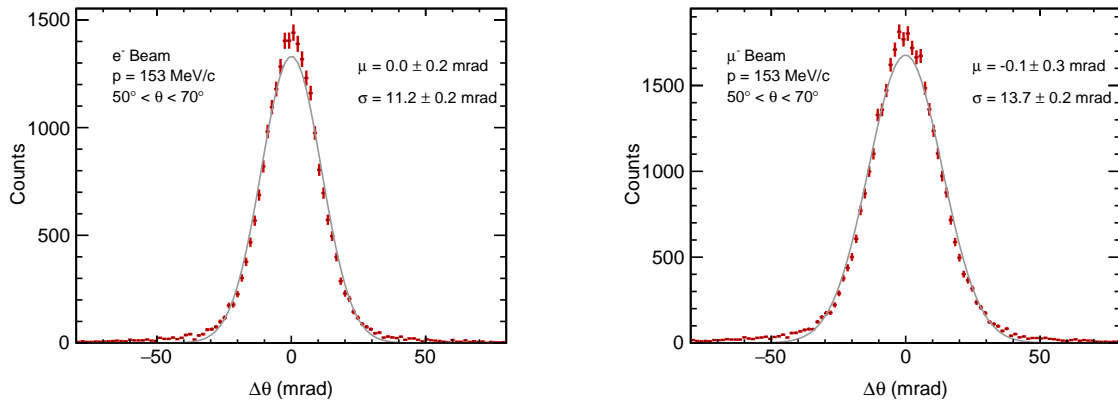


FIG. 59. Examples of differences between reconstructed and actual reaction scattering angle from simulations for electrons (left panel) and muons (right panel) with a beam momentum of 153 MeV/ $c$  and an average scattering angle of about  $60^\circ$ .

multiple scattering corrections will be calculated for the data, and the final systematic uncertainty might be much smaller if we can show in high precision calibration data that the simulations accurately model the effects of multiple scattering. To ensure accurate corrections can be done, we will measure multiple scatter from experiment components to verify the simulations. The uncertainty ultimately will depend on the accuracy of the

simulations, and the multiple scattering uncertainty given here is only a rough estimate.

The systematic uncertainties will be verified by measuring multiple cross sections with 6 primary experiment settings – two beam polarities  $\times$  three beam momenta. These primary settings will be supplemented with additional measurements at offset angles and momenta. The quality of the overlap of these data provide a check on the estimated systematics.

### Appendix C: Electronics Layout

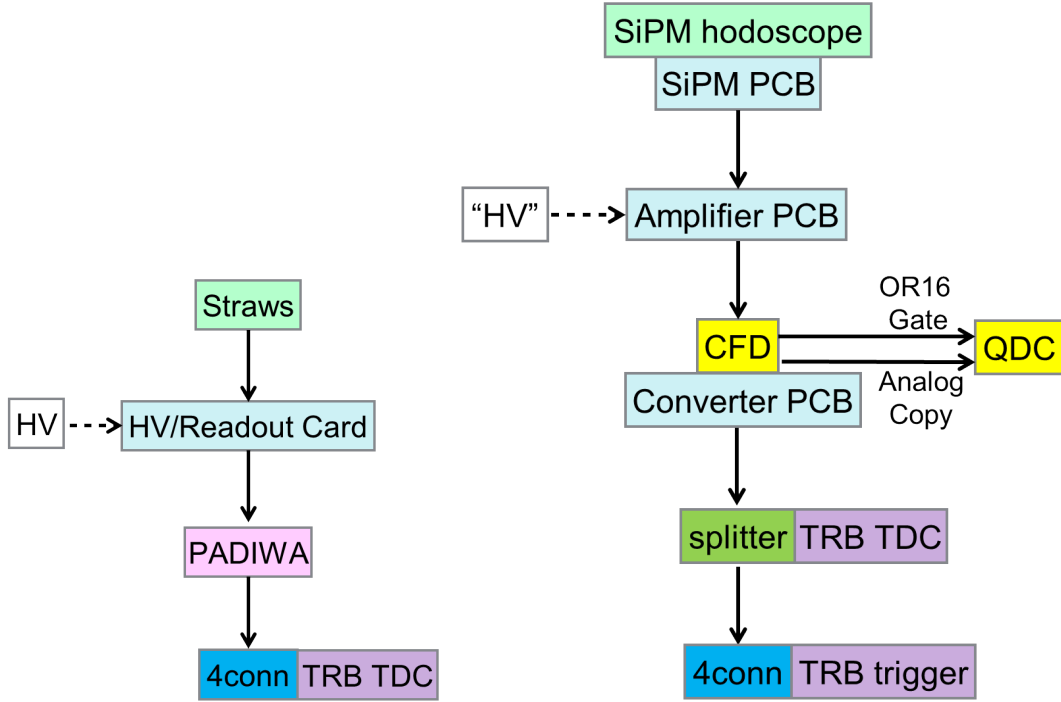


FIG. 60. Left: Electronics layout of the Straw Tube Tracker. Right: Electronics layout of all SiPM detectors including beam hodoscope and beam monitor SiPM detectors.

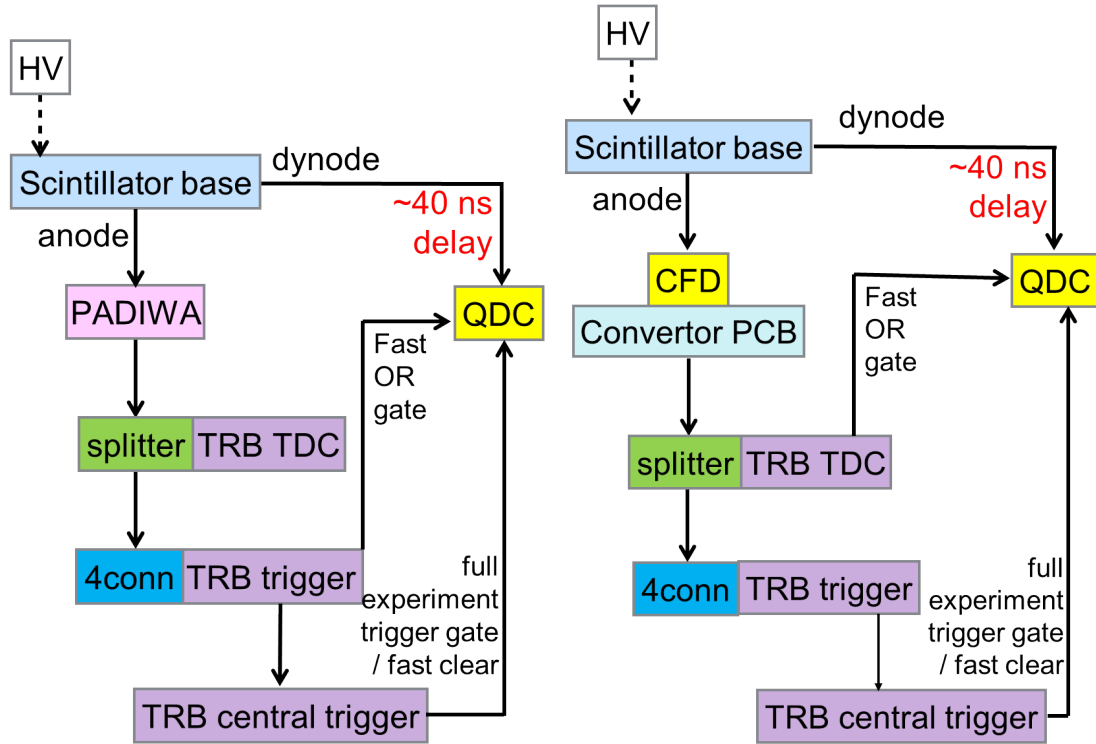


FIG. 61. Left: Electronics layout of the Scattered Particle Scintillators. Right: Electronics layout of the beam monitor scintillator paddles. Note the exchange of the PADIWA for an MCFD in the case of the beam monitor paddles in order to get good timing for out-of-time background particles for which there will be no good QCD signal.

- 
- [1] R. Pohl, A. Antognini, F. Nez, F. D. Amaro, F. Biraben, *et al.*, *Nature* **466**, 213 (2010).
- [2] A. Antognini *et al.*, *Science* **339**, 417 (2013).
- [3] J. Bernauer *et al.* (A1 Collaboration), *Phys.Rev.Lett.* **105**, 242001 (2010), arXiv:1007.5076 [nucl-ex].
- [4] X. Zhan, K. Allada, D. Armstrong, J. Arrington, W. Bertozzi, *et al.*, *Phys.Lett.* **B705**, 59 (2011), arXiv:1102.0318 [nucl-ex].
- [5] P. J. Mohr, B. N. Taylor, and D. B. Newell, *ArXiv e-prints* (2012), arXiv:1203.5425 [physics.atom-ph].
- [6] R. Pohl, R. Gilman, G. Miller, and K. Pachucki, *Annu.Rev.Nucl.Part.Sci.* **63**, 175 (2013).
- [7] R. Pohl, G. A. Miller, R. Gilman, *et al.*, “Workshop on the Proton Radius Puzzle at the Trento European Center for Theory in Nuclear Physics and Related Areas, <http://www.mpq.mpg.de/~rnp/wiki/pmwiki.php/Main/WorkshopTrento>,” (2012).
- [8] C. Carlson, R. Hill, S. Karshenboim, M. Vanderhaeghen, *et al.*, “Workshop on the Proton Radius Puzzle at the Mainz Institute for Theoretical Physics, <https://indico.mitp.uni-mainz.de/internalPage.py?pageId=0&confId=140>,” (2014).
- [9] J. Kelly, *Phys.Rev.* **C70**, 068202 (2004).
- [10] S. Agostinelli *et al.* (GEANT4), *Nucl. Instrum. Meth.* **A506**, 250 (2003).
- [11] R. Schumacher and U. Sennhauser, “Particle fluxes in  $\pi m1$ ,” (1987).
- [12] M. Albrow, H. Kim, S. Los, E. Ramberg, A. Ronzhin, *et al.*, *JINST* **7**, P10027 (2012), arXiv:1207.7248 [physics.ins-det].
- [13] R. Milner *et al.*, *Nuclear Inst. and Methods in Physics Research A* **741**, 1 (2014), arXiv:1312.1730.
- [14] B. Henderson *et al.*, *Physical Review Letters* **118**, 092501 (2017), arXiv:1611.04685v2.
- [15] W. Erni *et al.*, *The European Physical Journal A* **49**, 1 (2013).
- [16] M. Lutz *et al.* (PANDA Collaboration), (2009), arXiv:0903.3905 [hep-ex].
- [17] R. Gothe, E. Phelps, R. Steinman, and Y. Tian, “CLAS12 Forward Time-of-Flight at USC: A Comprehensive Update <http://www.physics.sc.edu/~gothe/research/pub/FToF12-review-11-09.pdf>,” (2009).
- [18] P. Blunden, W. Melnitchouk, and J. Tjon, *Phys.Rev.* **C72**, 034612 (2005), arXiv:nucl-th/0506039 [nucl-th].
- [19] P. G. Blunden and I. Sick, *Phys.Rev.* **C72**, 057601 (2005), arXiv:nucl-th/0508037 [nucl-th].
- [20] J. Arrington, P. Blunden, and W. Melnitchouk, *Prog.Part.Nucl.Phys.* **66**, 782 (2011),



arXiv:1105.0951 [nucl-th].

- [21] D. Borisyuk and A. Kobushkin, Phys.Rev. **C75**, 038202 (2007), arXiv:nucl-th/0612104 [nucl-th].
- [22] O. Tomalak and M. Vanderhaeghen, Phys. Rev. D **90**, 013006 (2014).
- [23] I. Sick, Phys.Lett. **B576**, 62 (2003), arXiv:nucl-ex/0310008 [nucl-ex].
- [24] P. J. Mohr, B. N. Taylor, and D. B. Newell, Rev.Mod.Phys. **80**, 633 (2008), arXiv:0801.0028 [physics.atom-ph].
- [25] E. Kraus, K. E. Mesick, A. White, R. Gilman, and S. Strauch, Phys. Rev. C **90**, 045206 (2014).